STATIC AND ROTATING NEUTRON STARS IN A GENERAL RELATIVISTIC FORMULATION OF ALL FUNDAMENTAL INTERACTIONS AND ASTROPHYSICAL APPLICATIONS

Thesis Advisors
Prof. Remo Ruffini
Dr. Jorge A. Rueda

Ph.D. Student
Riccardo Belvedere

Sapienza–University of Rome

Academic Year 2012/2013

"Set the Controls for the Heart of the Sun"

Pink Floyd

Contents

Chapter 1

Introduction

1.1 Neutron Stars as Astrophysical Laboratories

There exist four fundamental forces that allow us to describe the magnificent world built by Mother Nature in which we live. Among these forces, the strong, the weak, the electromagnetic and the gravitational one, it is the latter to be the most astonishing: extremely weak on short distances, it becomes the inescapable master of anything is surrounding us, once long distances or big masses are taken into account. Our world is governed by any of this four forces and a complete description of it can be reached only studying the connections between them. A wonderful mix of this four forces is represented by the neutron stars. Neutron stars are the densest stars known, with a radius of the order of 10 km, a mass slightly larger than the solar mass ($M_\odot \sim 1.989 \times 10^{33}$ g) and so a mass density of the order of 10^{15} g cm^{-3}, greater than the nuclear matter density. This means that the neutron stars can be used as astrophysical laboratories to explore any of the above-quoted forces, without the technical limits to which undergo terrestrial experiments. They allow to explore condensed matter states, critical electromagnetic fields, superfluidity and superconductivity, phase transitions, exotic matter, strong fields, nuclear forces at high densities and so on.

1.2 A Bit of History

The milestone work that opened the road to the neutron stars, has been the one from Landau in 1931 (published one year later) (Landau, 1932), where he introduced the idea of a denser star with respect to white dwarfs,

composed by matter at nuclear density. The neutrons were still not discovered, so, building an atomic nucleus only with electrons and protons led to a violation of the Heisenberg principle. Landau proposed a solution to this issue arguing a violation of the quantum statistics, but, more important, he understood that this new class of stars could be regarded as a sort of "*gigantic nucleus*". Just one year later, Chadwick discovered the main ingredient of a neutron star, the *neutron* (Chadwick, 1932).

It has been at the end of 1933, that Baade and Zwicky predicted for the first time the existence of the neutron stars analyzing the observations of supernova explosions with the aim of explaining the huge amount of energy released. As they wrote in their work (Baade and Zwicky, 1934): *"With all reserve we advance the view that a super-nova represents the transition of an ordinary star into a neutron star, consisting mainly of neutrons. Such a star may possess a very small radius and an extremely high density. As neutron can be packed much more closely than ordinary nuclei and electrons, the "gravitational packing" energy in a cold neutron star may become very large, and, under certain circumstances, may far exceed the ordinary nuclear packing fractions. A neutron star would therefore represent the most stable configuration of matter as such."*.

Some years later, in 1937, the scientific interest for the neutron stars grow up thanks to two independent works by Gamow (1937) and Landau (1938), in which they both argued about the possibility for any main sequence star to contain a neutron star as a core. Anyway, such a core, in their model, was useful to explain the amount of energy necessary for a normal star to be stable, but one year later Bethe and Critchfield (Bethe and Critchfield, 1938), demonstrated as the energy of a star is due to the thermonuclear reactions.

A fundamental step has been done by Tolman (1939) and Oppenheimer and Volkoff (1939), that in two different and independent works, published on the same day and in the same journal, described for the first time the equation of hydrostatic equilibrium for a spherically symmetric star in the context of a fully general relativistic theory. Oppenheimer and Volkoff (1939) calculated the maximum gravitational mass for a stable static neutron star, obtaining $M_{Max} \approx 0.71 M_{\odot}$ for an equation of state (EOS) [1] of stellar matter composed only by a strongly degenerate relativistic gas of non-interacting neutrons. The main problem of this limit was its quite low value, so low that was below the Chandrasekhar mass limit for the white dwarfs (Chandrasekhar,

[1] An equation of state, or EOS for short, is a relation describing the dependence of the pressure P on energy density $\mathcal{E}$ (or on mass density via the relation $\mathcal{E}=\rho c^2$), and temperature T (even if, for a system composed mainly by degenerate fermions as neutron stars are, the temperature is mostly negligible) as well as other parameters depending by the star composition.

1931). This low limit could prevent the formation of the neutron star and was due mainly to the absence of the strong interactions, which provide additional pressure, thus increasing the maximum mass allowable. Oppenheimer and Volkoff discussed the idea of introducing repulsive neutron-neutron interactions to increase the maximum mass value, but they concluded that their $0.71 M_{\odot}$ limit was close to the real one. In 1958 Wheeler and his collaborators described a neutron star with a core composed by neutrons, protons and electrons in β-equilibrium (Harrison et al., 1958) and one year later Cameron (Cameron, 1959) emphasized the importance of the strong interactions and how the Oppenheimer-Volkoff limit could be increased up to a more realistic $\sim 2M\odot$ value for a neutron star born through a supernova explosion. Then, in 1974, Rhoades and Ruffini (1974), with the aim to provide a method to observationally distinguish neutron stars from black holes, established an absolute upper limit for the mass of neutron stars, $M_{\rm max} \approx 3.2\ M_{\odot}$, through the principle of causality and Le Chatelier's principle, in the framework of general relativity.

The possibility to observe directly a neutron star came with the beginning of the X-ray astronomy during the $'60s$ (Giacconi et al., 1962). In that period a lot of theories born to suggest how to discover neutron stars (see e.g. Zeldovich and Novikov (1971); Shapiro and Teukolsky (1983); Lyne and Graham-Smith (1998)): it is noteworthy a work by Pacini (Pacini, 1967), in which it is shown how a rapidly rotating neutron star with a strong magnetic field (assumed as a dipole one) could convert its rotational energy into electromagnetic radiation and accelerate particles to high energies. Neutron stars were discovered almost casually in 1967 and with methods quite different form the ones proposed earlier: Jocelyn Bell discovered a weak variable radio source, during night observations (Hewish and Okoye, 1965). The period of this source was extremely stable as if it could derive from an artificial signal. At the beginning of 1968 three other *pulsar* were discovered and it was proposed that them could be either oscillating white dwarfs or neutron stars (Hewish et al., 1968). The observational evidence that ruled out the possibility for a pulsar to be a white dwarfs has been given by the discovery of Crab pulsar in 1968 and the studies of its rotational period ($\sim$ 33 ms, too short for a white dwarf) (Comella et al., 1969): the idea by Pacini and (in a different and independent work) by Gold (Gold, 1968) about pulsars as rotating magnetized neutron stars has been since then the standard picture of a pulsar.

1.3 Birth

Neutrons stars belong to the family of *compact objects*, together with white dwarfs and black-holes. All of them are born from stars, once the thermonuclear fuel is ended. The final stage depends from the mass of the progenitor star and the environmental conditions. It is widely believed that a neutron star is born from a star more massive than 8 solar masses: the burning of the thermonuclear fuel leads the star to join the super red giant stage. In the central region of the red star, the reactions burn to the iron end point and the core can resist against the gravitational collapse only thanks to the pressure of the degenerate nonrelativistic electrons. The external layers burn adding to the iron core mass until the gravity squeeze the core itself and the increasing pressure forces the nonrelativistic electrons to become relativistic. The core of the star reaches the maximum possible mass for an object supported by the pressure of ultrarelativistic, degenerate electrons, namely the Chandrasekhar limit ($\approx 1.4 M_\odot$) (Chandrasekhar, 1931). The core undergoes a sort of free-fall on itself, increasing its temperature and pressure until the neutrons degeneracy pressure contrasts the gravitational force and a rebound on itself, generating a shock wave that expel the external layers of the supergiant red star and resulting in a supernova explosion. The new system is composed by a cloud of matter expelled by the dead star, the supernova remnant (SNR), and, at the center of this system, by the "old" core, composed mainly by neutrons and a small fraction of electrons and protons: a neutron star (Haensel et al., 2007; Shapiro and Teukolsky, 1983).

1.4 Neutron Star Structure

The state of the art about the understanding of the neutron star's inner structure lays on solving the Tolman-Oppenheimer-Volkoff (TOV) system of equations, which, for a static neutron star under the assumption of local charge neutrality, are given by

$$\frac{d\mathcal{P}}{dr} = -\frac{G(\mathcal{E}+\mathcal{P})(M+4\pi r^3\mathcal{P})}{r^2(1-\frac{2GM}{r})}\,, \tag{1.1}$$

$$\frac{dM}{dr} = 4\pi r^2 \mathcal{E}\,, \tag{1.2}$$

where $M{=}M(r)$ is the mass enclosed at the radius r and the energy-density $\mathcal{E}$ and the pressure $\mathcal{P}$ are related by some EOS $\mathcal{P}{=}\mathcal{P}(\mathcal{E})$; see Fig. 1.1 for a schematic review of some solution of the TOV equations for different EOS:

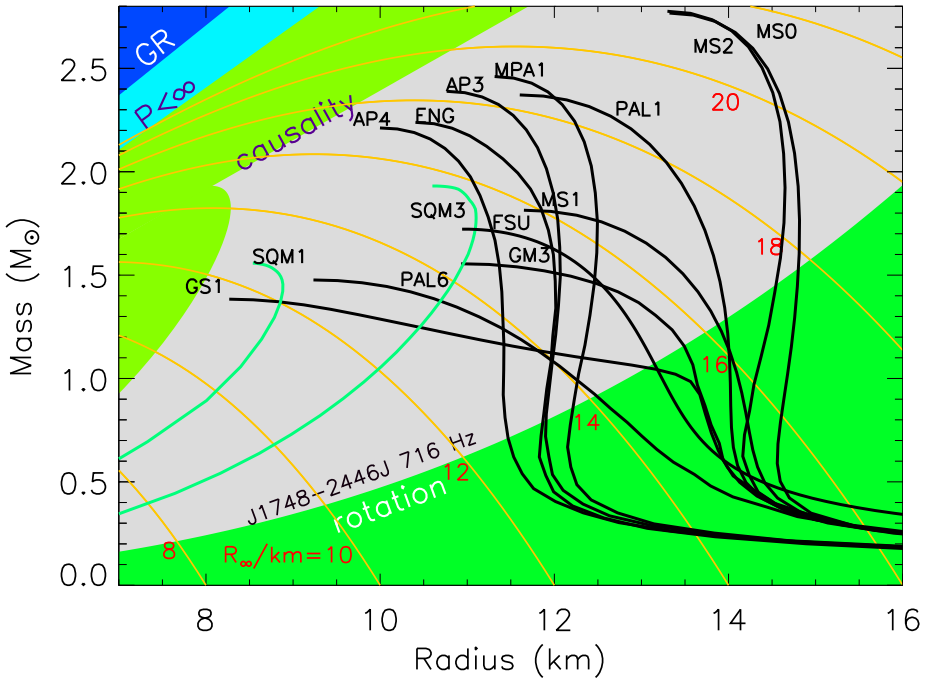

Figure 1.1: Mass versus radius relation for different EOS for neutron stars (and quark stars), obtained solving the TOV system of equations 1.1; (for details see e.g. Lattimer, 2012, and references therein). Plot from (Lattimer, 2012).

Different regions inside the neutron stars can be found, depending by the variation of the matter density from the center of the star up to the external border: in Fig. 1.2 is shown an artistic picture of the inner structure of a neutron star.

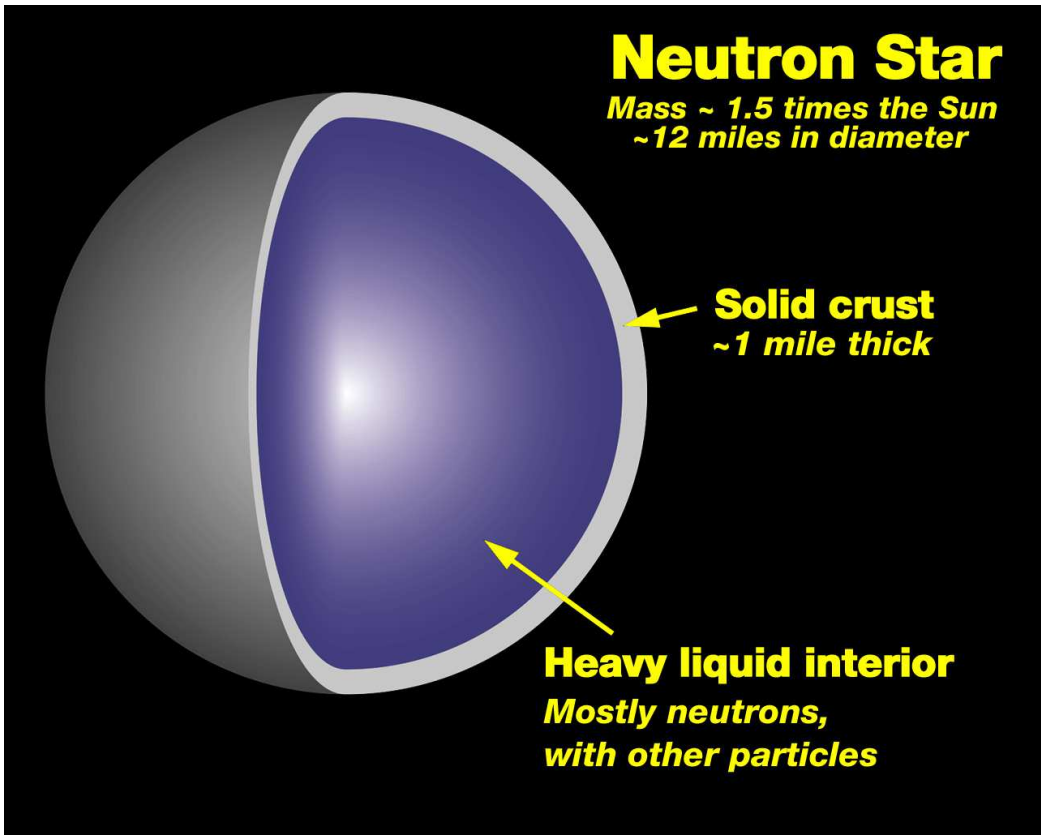

Figure 1.2: Artistic neutron star cross section.

Following the standard picture of the neutron stars, the first region that we find starting from the low-density bottom layers is the *outer crust*. The outer crust is a few hundred meters thick and composed mainly by nuclei immersed in a sea of free electrons, namely, by a nuclei lattice surrounded by white dwarf-like material. In the outer crust, the matter density grows up to the "neutron drip" density $\rho_{\rm drip} \approx 4.3 \times 10^{11}$ g cm^{-3}. At this density, it becomes energetically favorable for neutrons to drip out from nuclei, and the so-called *inner crust* begins. The inner crust is about one kilometer thick and it is composed by a nuclei lattice in a background of electrons and neutrons. Below the inner crust, the *core* begins. The matter density to which the core begins is model dependent, anyway, this value is generally close to the value of the matter saturation density for ordinary nuclei $\rho_{\rm nuc} \approx 2.7 \times 10^{14}$

g cm^{-3}, corresponding to a baryon number density $n_{\rm nuc} \approx 0.16$ fm^{-3}. The core is about 10 km thick and its composition depends, as for the density to which it begins, by the particular model used. Depending on the nuclear model, in a neutron star core it is possible to find ordinary matter, namely a degenerate gas of free neutrons, electrons and protons, or, in addition, more exotic particles that could be created by the high pressure reached in the most inner regions of the neutron star core. The maximum possible density at the center of the core is also model dependent.

1.5 The General Relativistic Thomas-Fermi Theory and the Neutron Stars

It is since long time ago that it has been recognized the Thomas-Fermi model in the realm of Atomic Physics (Gombás, 1950; Lieb, 1981). In 1973, for the first time, it was proposed, as a theoretical interest, that the Thomas-Fermi model could be used to obtain an alternative derivation of a self-gravitating system of fermions, within Newtonian gravity, able to give a description of neutron stars and white dwarfs in addition to the usual derivation in the perfect fluid approximation (Ruffini and Bonazzola, 1969; Dewitt and Dewitt, 1973). To describe the gravitational effect of relativistic objects as neutron stars and white dwarfs, as well as to describe the physics of heavy nuclei (Migdal et al. (1976, 1977); Ferreirinho et al. (1980); Ruffini and Stella (1981)), it is mandatory to generalize the Thomas-Fermi model to the special relativistic level. The Thomas-Fermi treatment started to span from the original realm of Atomic Physics, through its special relativistic extension, to gravitational and Nuclear Physics.

It has been thanks to the recent works by Ruffini et al. (2007); Ruffini (2008); Popov (2010); Rotondo et al. (2011d), that the Thomas-Fermi model started to be used in a rigorous way to describe neutron stars, taking into account Nuclear Physics, Newtonian Physics and β-equilibrium. In particular, in (Ruffini, 2008), it has been shown, for the first time, the possibility to have overcritical electric fields in the core of the neutron stars. All this works led to the necessity to improve the Thomas-Fermi model, generalizing it up to the general relativistic formulation, with the aim of describing relativistic objects as neutron stars. A fundamental step, in this sense, has been made by Rotondo et al. (2011b) through the use of the Wigner-Seitz cell. First of all they generalized the classical approach of Feynman, Metropolis and Teller (FMT) (Feynman et al., 1949), solving the relativistic Thomas-Fermi model for compressed atoms (Rotondo et al., 2011b): this work led to

a new equation of state for white dwarfs duly expressed in general relativity (Rotondo et al., 2011a). As a consequence of this work, the same authors proved the impossibility of imposing local charge neutrality on chemically balanced matter made of neutrons, protons, and electrons, in the simplified case in which the strong interactions are not taken into account (Rotondo et al., 2011c). This was a critical issue for neutron star matter calculations, because Rotondo et al. (2011c) demonstrated that the equations which describe baryonic matter and the Einstein-Maxwell equations need to be solved simultaneously. In a subsequent work, Rueda et al. (2011) generalized this theory including the strong interactions.

As said in Sec. 1.4, the classic work of Oppenheimer and Volkoff (1939)es address the problem of the equilibrium configurations for a neutron star composed only by neutrons. Even generalizing the model including other ingredients as protons and electrons, in all of the scientific literature on neutron stars, it is still assumed that the condition of local charge neutrality applies identically to all points of the equilibrium configuration (see e.g. Haensel et al. (2007)). As a consequence, the corresponding solutions in this more general cases of a non-rotating neutron star, are systematically obtained again on the base of the TOV equations.

In general, to describe the equilibrium configurations of multi-particle systems it must to be taken into account the framework of statistical physics of multicomponent systems (see e.g. Evans (1992)). To ensure the thermodynamic equilibrium of these systems, it has to be imposed the constancy, throughout the whole configuration, of the generalized chemical potentials, often called "electro-chemical", of each of the components of the system; (see e.g. Klein, 1949; Kodama and Yamada, 1972; Olson and Bailyn, 1975). Such generalized potentials include both the contribution due to kinetic energy and the contribution due to the potential fields, e.g. gravitational and electromagnetic potential energies per particle, and, once the rotation is considered, also the centrifugal potential. For such systems, in presence of gravitational and Coulomb fields, electric polarization effects at macroscopic scales occur. The balance of the gravitational and electric forces acting on ions and electrons in ideal electron-ion plasma leading to the occurrence of gravito-polarization was first pointed out in the classic work of S. Rosseland (1924).

Once the gravito-polarization effects are included in the theory of neutron stars, the corresponding theoretical treatment acquires remarkable conceptual and theoretical complexity, since it must be necessarily formulated consistently within the Einstein-Maxwell system of equations. In 1949, Klein (1949), first introduced the constancy of the general relativistic chemical potential of particles, hereafter "Klein potentials", in the study of the thermodynamic equilibrium of a self-gravitating one-component fluid of neutral

particles throughout the configuration within the framework of general relativity. In 1972, Klein's work has been extended to the case of neutral multi-component degenerate fluids (Kodama and Yamada (1972)) and later, in 1975, to the case of multi-component degenerate fluid of charged particles by Olson and Bailyn (1975).

Recently, using the concept of Klein potentials, Rotondo et al. (2011c) demonstrated the impossibility of imposing the condition of local charge neutrality in the simplest case of a self-gravitating system of degenerate neutrons, protons and electrons in β-equilibrium: it has been shown that the consistent treatment of such simple system demands the solution of the general relativistic Thomas-Fermi equations, coupled with the Einstein-Maxwell ones, being the TOV equations thus superseded.

In the mean time, Rueda et al. (2011) formulated the theory of a system of neutrons, protons and electrons fulfilling strong, electromagnetic, weak and gravitational interactions. There, the role of the Klein first integrals has been again highlighted and their theoretical formulation in the Einstein-Maxwell background and in the most general case of finite temperature has been presented, generalizing the previous results for the "non-interacting" case (Rotondo et al., 2011c). The strong interactions are there modeled by a relativistic nuclear mean field theory, and, more exactly, are described by the introduction of the σ, ω and ρ virtual mesons (see Appendix A for details).

1.6 Plan of the Thesis

In Chap. 2 are constructed the equilibrium configurations of non-rotating neutron stars following the new approach shown by Rotondo et al. (2011c); Rueda et al. (2011). We calculate the properties of neutron star matter and neutron stars treated fully self-consistently with strong, weak, electromagnetic, and gravitational interactions. The full set of the Einstein-Maxwell-Thomas-Fermi (EMTF) equations is solved numerically for zero temperatures and for selected parameterizations of the nuclear model.

In Chap. 3 we examine the equilibrium configurations of slowly rotating neutron stars by using the Hartle formalism in the case of the EMTF equations presented in Chap. 2. We integrate these equations of equilibrium for different central densities ρ_c and circular angular velocities Ω and compute the mass M, polar R_p and equatorial $R_{\rm eq}$ radii, angular momentum J, eccentricity ϵ, moment of inertia I, as well as quadrupole moment Q of the configurations. Both the Keplerian mass-shedding limit and the axisymmetric secular instability are used to construct the new mass-radius relation. Moreover we compute the maximum and minimum masses and rotation fre-

quencies of neutron stars. At the end of the chapter we compare and contrast all the results for the global and local charge neutrality cases.

In Chap. 4, we compare and contrast the obtained neutron star parameters such as moment of inertia and radius with respect to the traditionally assumed fiducial values. We also show the inapplicability of some existent analytic formulas for the description of the maximally rotating sequence and the moment of inertia of neutron stars. The consequences of our results on neutron star astrophysics is explored; it is shown in particular that the magnetic field of pulsars can be overestimated up to one order of magnitude when computed with fiducial parameters.

At the end we briefly summarize our results (see Chap. 5), the research activities, as well as the scientific production obtained during the different stages of this research work (see Chap. 6).

Spacetime metric signature (+,-,-,-) and units $\hbar = c = 1$ are used unless otherwise specified.

Chapter 2

Equilibrium Configurations for Static Neutron Stars, Relativistic Mean Field Theory and Global Charge Neutrality

2.1 Introduction

In this first chapter, we formulate the equations of equilibrium of neutron stars taking into account strong, weak, electromagnetic, and gravitational interactions within the framework of general relativity. The nuclear interactions are described by the exchange of the σ, ω, and ρ virtual mesons. The equilibrium conditions are given by the recently developed theoretical framework based on the Einstein-Maxwell-Thomas-Fermi equations along with the constancy of the general relativistic Fermi energies of particles, the "Klein potentials", throughout the configuration. The equations are solved numerically in the case of zero temperatures and for selected parameterizations of the nuclear models. The solutions lead to a new structure of the star: a positively charged core at supranuclear densities surrounded by an electronic distribution of thickness $\sim \hbar/(m_e c) \sim 10^2 \hbar/(m_\pi c)$ of opposite charge, as well as a neutral crust at lower densities. Inside the core there is a Coulomb potential well of depth $\sim m_\pi c^2/e$. The constancy of the Klein potentials in the transition from the core to the crust, impose the presence of an overcritical electric field $\sim (m_\pi/m_e)^2 E_c$, the critical field being $E_c = m_e^2 c^3/(e\hbar)$. The electron chemical potential and the density decrease, in the boundary interface, until values $\mu_e^{\rm crust} < \mu_e^{\rm core}$ and $\rho_{\rm crust} < \rho_{\rm core}$. For each central density, an entire family of core-crust interface boundaries and, correspondingly, an

entire family of crusts with different mass and thickness, exist. The configuration with $\rho_{\rm crust} = \rho_{\rm drip} \sim 4.3 \times 10^{11}$ g/cm^3 separates neutron stars with and without inner crust. We present here the novel neutron star mass-radius for the especial case $\rho_{\rm crust} = \rho_{\rm drip}$ and compare and contrast it with the one obtained from the traditional Tolman-Oppenheimer-Volkoff treatment.

We construct the constitutive equilibrium equations for the core, the crust and the transition layer in between in Sec. 2.2. In Sec. 2.3 we show the results of the numerical integration of the equilibrium system of equations. We focus on the effects of the Coulomb interactions on the structure of the neutron star crust as well as on the abundances of the chemical elements in the crust once the electrostatic forces are taken into account. The observational constraints on the mass-radius relation are discussed in Sec. 2.4. In Sec. 2.5 we compare and contrast the globally and the locally neutral neutron star configurations. We finally summarize the results in Sec. 2.6 and suggest some perspectives in Sec. 2.7.

2.2 The Constitutive Relativistic Equations

2.2.1 Core Equations

It has been clearly recognized that, since neutron stars cores may reach density of order $\sim 10^{16}$–10^{17} g/cm^3, much larger than the nuclear density $\rho_{\rm nuc} \sim 2.7 \times 10^{14}$ g/cm^3, approaches for the nuclear interaction between nucleons based on phenomenological potentials and non-relativistic many-body theories become inapplicable (see Bowers et al. (1973b,a), for instance). Based on the pioneering work of Johnson and Teller (Johnson and Teller, 1955), Duerr (Duerr, 1956) and later on Miller and Green (Miller and Green, 1972) formulated the basis of what is now known as Relativistic Mean Field Theory (RMFT for short) of nuclear matter. They constructed the simplest relativistic model that accounts for the binding of symmetric nuclear matter at saturation density by introducing the interaction of one scalar field and one vector field with nucleons through Yukawa couplings. A nuclear model with only the scalar field with a self-interacting potential up to quartic order based on the sigma-model was considered by Lee and Wick (1974); Lee and Margulies (1975). The repulsive contribution of nuclear force was there introduced by hand through a *hard-sphere* model that artificially increases the nucleon Fermi momentum emulating the effect of a massive vector field coupled to nucleons. The relevance of such interactions as well as relativistic effects in the determination of the equation of state and in the nuclear matter properties such as compressibility and the nucleon effective

mass was clearly pointed out in (Miller and Green, 1972; Boguta and Rafelski, 1977; Boguta and Bodmer, 1977). The importance of allowing scalar meson self-interactions (cubic and quartic terms in the scalar field potential) as adjustable parameters to reproduce physical nuclear properties and not due to renormalization (see e.g. Walecka (1974)) was stressed by Boguta and Bodmer (1977); Boguta and Stocker (1983); Boguta and Moszkowski (1983); Boguta (1989). The necessity of introducing additional isovector fields to match the empirical symmetry energy of nuclear matter at saturation density was recognized by Boguta and Bodmer (1977).

Assuming that the nucleons interact with σ, ω and ρ meson fields through Yukawa-like couplings and assuming flat spacetime the equation of state of nuclear matter can be determined. However, it has been clearly stated by Rotondo et al. (2011c); Rueda et al. (2011) that, when we turn into a neutron star configuration at nuclear and supranuclear densities, the global description of the Einstein-Maxwell-Thomas-Fermi equations is mandatory. Associated to this system of equations there is a sophisticated eigenvalue problem, especially the one for the general relativistic Thomas-Fermi equation is necessary in order to fulfill the global charge neutrality of the system and to consistently describe the confinement of the ultrarelativistic electrons.

We here adopt the phenomenological relativistic mean field nuclear model of Boguta and Bodmer (1977) by assuming nucleons interacting in minimal coupling approximation with a σ isoscalar meson field that provides the attractive long-range part of the nuclear force and a massive vector field ω that models the repulsive short range. The self-interacting scalar field potential $U(\sigma)$ is assumed as a quartic polynomial with adjustable coefficients. In addition, a massive isovector field ρ is introduced to accounts for surface as well as isospin effects of nuclei.

The total Lagrangian density of the system is given by

$$\mathcal{L} = \mathcal{L}_g + \mathcal{L}_f + \mathcal{L}_\sigma + \mathcal{L}_\omega + \mathcal{L}_\rho + \mathcal{L}_\gamma + \mathcal{L}_{\rm int}\,, \tag{2.1}$$

where $\mathcal{L}_g$, $\mathcal{L}_\sigma$, $\mathcal{L}_\omega$, $\mathcal{L}_\rho$ are the Lagrangian densities for the free- fields, $\mathcal{L}_f$ is the Lagrangian density for the three fermion species and $\mathcal{L}_{\rm int}$ is the interacting part of the Lagrangian density, in the minimal coupling assumption (for details refer to Appendix A and Belvedere et al. (2012); Rueda et al. (2011)).

The non-rotating spherically symmetric spacetime metric is

$$ds^2 = {\rm e}^{\nu(r)}dt^2 - {\rm e}^{\lambda(r)}dr^2 - r^2 d\theta^2 - r^2\sin^2\theta d\varphi^2\,, \tag{2.2}$$

where the $\nu(r)$ and $\lambda(r)$ are only functions of the radial coordinate r.

For very large number of fermions, we adopt the mean-field approximation in which fermion-field operators are replaced by their expectation values (see

Ruffini and Bonazzola (1969), for instance). Within this approximation, the full system of general relativistic equations, in the degenerate case $T = 0$, can be written in the form (see Appendix A and Belvedere et al. (2012) for details, and Rueda et al. (2011) for a generalization to the finite temperature case).

$$\mathrm{e}^{-\lambda(r)}\left(\frac{1}{r^2}-\frac{1}{r}\frac{d\lambda}{dr}\right)-\frac{1}{r^2}=-8\pi G T_0^0\,, \tag{2.3}$$

$$\mathrm{e}^{-\lambda(r)}\left(\frac{1}{r^2}+\frac{1}{r}\frac{d\nu}{dr}\right)-\frac{1}{r^2}=-8\pi G T_1^1\,, \tag{2.4}$$

$$\frac{d^2V}{dr^2}+\frac{dV}{dr}\left[\frac{2}{r}-\frac{1}{2}\left(\frac{d\nu}{dr}+\frac{d\lambda}{dr}\right)\right]=-e\,\mathrm{e}^{\nu/2}\mathrm{e}^{\lambda}(n_p-n_e)\,, \tag{2.5}$$

$$\partial_\sigma U(\sigma)+g_s n_s=0\,, \tag{2.6}$$

$$g_\omega J_0^\omega-m_\omega^2\omega=0\,, \tag{2.7}$$

$$g_\rho J_0^\rho-m_\rho^2\rho=0\,, \tag{2.8}$$

$$E_e=\mathrm{e}^{\nu/2}\mu_e-eV=\text{constant}\,, \tag{2.9}$$

$$E_p=\mathrm{e}^{\nu/2}\mu_p+\mathcal{V}_p=\text{constant}\,, \tag{2.10}$$

$$E_n=\mathrm{e}^{\nu/2}\mu_n+\mathcal{V}_n=\text{constant}\,. \tag{2.11}$$

where $\mu_i = \partial\mathcal{E}/\partial n_i = \sqrt{(P_i^F)^2+\tilde{m}_i^2}$ and $n_i = (P_i^F)^3/(3\pi^2)$ are the free-chemical potential and number density of the i-specie with Fermi momentum P_i^F, while g_γ and m_γ are the coupling constants and the masses of the three virtual mesons respectively. The particle effective mass is $\tilde{m}_N = m_N + g_s\sigma$ and $\tilde{m}_e = m_e$ and the effective potentials $\mathcal{V}_{p,n}$ are given by

$$\mathcal{V}_p = g_\omega\omega+g_\rho\rho+eV\,, \tag{2.12}$$

$$\mathcal{V}_n = g_\omega\omega-g_\rho\rho\,. \tag{2.13}$$

Eqs. (2.9)–(2.11) describe the Thomas-Fermi equilibrium conditions: the constancy of the generalized Fermi energies E_n^F, E_p^F and E_e^F, the Klein potentials, derives from the thermodynamic equilibrium conditions given by the statistical physics of multicomponent systems, applied to a system of degenerate neutrons, protons, and electrons within the framework of general relativity (Rueda et al., 2011). These constants are linked by the β-equilibrium (Boguta, 1981) between the matter constituents

$$E_n^F = E_p^F + E_e^F\,. \tag{2.14}$$

These equations must be solved with the boundary conditions given by the fulfillment of the condition of global charge neutrality and the continuity of

the Klein potentials of particles between the core and the crust (see Rotondo et al. (2011c); Rueda et al. (2011) and below for details).

The parameters of the nuclear model, namely the coupling constants g_s, g_ω and g_ρ, and the meson masses m_σ, m_ω and m_ρ are fixed by fitting experimental properties of nuclei, such as saturation density, binding energy per nucleon (or experimental masses), symmetry energy, surface energy, and nuclear incompressibility. In Table 2.1 we present selected fits of the nuclear parameters. In particular, we show the following parameter sets: NL3 (Lalazissis et al., 1997), NL-SH (Sharma et al., 1993), TM1 (Sugahara and Toki, 1994), and TM2 (Hirata et al., 1995).

	NL3	NL-SH	TM1	TM2
m_σ (MeV)	508.1940	526.0590	511.198	526.443
m_ω (MeV)	782.5010	783.0000	783.000	783.000
m_ρ (MeV)	763.0000	763.0000	770.000	770.000
g_s	10.21700	10.44400	10.0289	11.4694
g_ω	12.86800	12.94500	12.6139	14.6377
g_ρ	4.474000	4.383000	4.63220	4.6783
g_2 (fm^{-1})	-10.4310	-6.90990	-7.2325	-4.4440
g_3	-28.8850	-15.8337	0.61830	4.6076
c_3	0.0000	0.000000	71.30750	84.5318

Table 2.1: Selected parameter sets of the σ-ω-ρ model.

The constants g_2 and g_3 are the third and fourth order constants of the self-scalar interaction as given by the scalar self-interaction potential (see Boguta and Bodmer (1977), for instance)

$$U(\sigma) = \frac{1}{2}m_\sigma^2\sigma^2 + \frac{1}{3}g_2\sigma^3 + \frac{1}{4}g_3\sigma^4\,. \tag{2.15}$$

The non-zero constant c_3 that appears in the TM1 and TM2 models corresponds to the self-coupling constant of the non-linear vector self-coupling $\frac{1}{4}c_3(\omega_\mu\omega^\mu)^2$. We have not include such a self-coupling vector interaction in the general formulation presented above. However, we shown also here the results of the integration when such a self-interaction is taken into account (refer to Sugahara and Toki (1994); Hirata et al. (1995) for details about the motivations of including such a contribution).

The numerical integration of the core equations can be started given a central density and the regularity conditions at the origin; see below Sec. 2.3 for details. At nuclear density the phase-transition to the "solid" crust takes place. Thus, the radius of the core $R_{\rm core}$ is given by $\mathcal{E}(r = R_{\rm core})/c^2 = \rho_{\rm nuc}$.

2.2.2 Core-Crust Transition Layer Equations

In the core-crust interface, the mean-field approximation for the meson-fields is not valid any longer and thus a full numerical integration of the meson-field equations of motion, taking into account all gradient terms, must be performed. We expect for the core-crust transition boundary-layer to be a region with characteristic length scale of the order of the electron Compton wavelength $\sim \lambda_e = \hbar/(m_e c) \sim 100$ fm corresponding to the electron screening scale. Then, in the core-crust transition layer, the system of equations (2.3)–(2.11) reduces to

$$\frac{d^2V}{dr^2} + \frac{2}{r}\frac{dV}{dr} = -e^{\lambda_{\rm core}} e J_0^{ch} \,, \tag{2.16}$$

$$\frac{d^2\sigma}{dr^2} + \frac{2}{r}\frac{d\sigma}{dr} = e^{\lambda_{\rm core}} \left[\partial_\sigma U(\sigma) + g_s n_s\right] \,, \tag{2.17}$$

$$\frac{d^2\omega}{dr^2} + \frac{2}{r}\frac{d\omega}{dr} = -e^{\lambda_{\rm core}} \left[g_\omega J_0^\omega - m_\omega^2 \omega\right] \,, \tag{2.18}$$

$$\frac{d^2\rho}{dr^2} + \frac{2}{r}\frac{d\rho}{dr} = -e^{\lambda_{\rm core}} \left[g_\rho J_0^\rho - m_\rho^2 \rho\right] \,, \tag{2.19}$$

$$E_e = e^{\nu_{\rm core}/2}\mu_e - eV = \text{constant} \,, \tag{2.20}$$

$$E_p = e^{\nu_{\rm core}/2}\mu_p + eV + g_\omega\omega + g_\rho\rho = \text{constant} \,, \tag{2.21}$$

$$E_n = E_p + E_e \,, \tag{2.22}$$

due to the fact that the metric functions are essentially constant on the core-crust transition layer and thus it is possible to take their values at the core-radius $e^{\nu_{\rm core}} \equiv e^{\nu(R_{\rm core})}$ and $e^{\lambda_{\rm core}} \equiv e^{\lambda(R_{\rm core})}$. Here we have replaced the TOV equation (see Eqs. (2.3)–(2.4)) with appropriate conservation laws for the generalized particle Fermi energies and the beta equilibrium condition.

The system of equations of the transition layer has a stiff nature due to the existence of two different scale lengths. The first one is associated with the nuclear interactions $\sim \lambda_\pi = \hbar/(m_\pi c) \sim 1.5$ fm and the second one is due to the aforementioned screening length $\sim \lambda_e = \hbar/(m_e c) \sim 100$ fm. Thus, the numerical integration of Eqs. (2.16)–(2.22) has been performed subdividing the core-crust transition layer in the following three regions: (I) a mean-field-like region where all the fields vary slowly with length scale $\sim \lambda_e$, (II) a strongly interacting region of scale $\sim \lambda_\pi$ where the surface tension due to nuclear interactions dominate producing a sudden decrease of the proton and the neutron densities and, (III) a Thomas-Fermi-like region of scale $\sim \lambda_e$ where only a layer of opposite charge made of electrons is present producing the total screening of the positively charged core.

In Fig. 2.1, we show the core-crust transition layer for the NL3-model of Table 2.1 with and without the presence of the ρ-meson. The presence of the

ρ-meson is responsible for the nuclear asymmetry within this nuclear model. The relevance of the nuclear symmetry energy on the structure of nuclei and neutron stars is continuously stressed in literature; see e.g. Müther et al. (1987); Kubis (2007); Sharma and Pal (2009); Hebeler et al. (2010); Loan et al. (2011). The precise value of the nuclear symmetry energy plays here a crucial in determining the precise value of the ρ-meson coupling which, in the present case, is essential in the determination of the intensity of the electric field in the core-crust boundary interface, as can be seen from the comparison of the right and the left plot in Fig. 2.1.

We have integrated numerically Eqs. (2.3)–(2.11) for the models listed in Table 2.1. The boundary conditions for the numerical integration are fixed through the following procedure. We start assuming a value for the central baryon number density $n_b(0) = n_n(0)+n_p(0)$. From the regularity conditions at the origin we have $e^{-\lambda(0)} = 1$ and $n_e(0) = n_p(0)$.

The metric function ν at the origin can be chosen arbitrarily, e.g. $\nu(0) = 0$, due to the fact that the system of equations remain invariant under the shift $\nu \to \nu+$ constant. The right value of ν is obtained once the end of the integration of the core has been accomplished and duly matched to the crust, by fulfilling the following identity at the surface of the neutron star,

$$e^{\nu(R)} = e^{-\lambda(R)} = 1 - \frac{2GM(R)}{c^2 R}\,, \tag{2.23}$$

being $M(R)$ and R the total mass and radius of the star. Then, taking into account the above conditions, the system of equations (2.6)–(2.11) is solved at the origin for the other unknowns $\sigma(0)$, $\omega(0)$, $\rho(0)$, $n_n(0)$, $n_p(0)$, $n_e(0)$.

The initial conditions for the numerical integration of the core-crust transition layer equations are determined by the final values given by the numerical integration of the core equations, i.e. we take the values of all the variables at the core-radius $R_{\rm core}$.

In the region "I" the effect of the Coulomb interaction is clear: on the proton-profile we can see a bump due to Coulomb repulsion while the electron-profile decreases as expected. Such a Coulomb effect is indirectly felt also by the neutrons due to the coupled nature of the system of equations. However, the neutron-bump is much smaller than the one of protons and it is not appreciable in Fig. 2.1 due to the plot-scale. In the region "II" we see clearly seen the effect of the surface tension due to nuclear interaction which produces a sharp decrease of the neutron and proton profiles in a characteristic scale $\sim \lambda_\pi$. In addition, it can be seen a neutron skin effect, analogous to the one observed in heavy nuclei, which makes the scale of the neutron density falloff slightly larger with respect to the proton one, in close analogy to the neutron skin effect observed in neutron rich nuclei, see e.g. Tamii

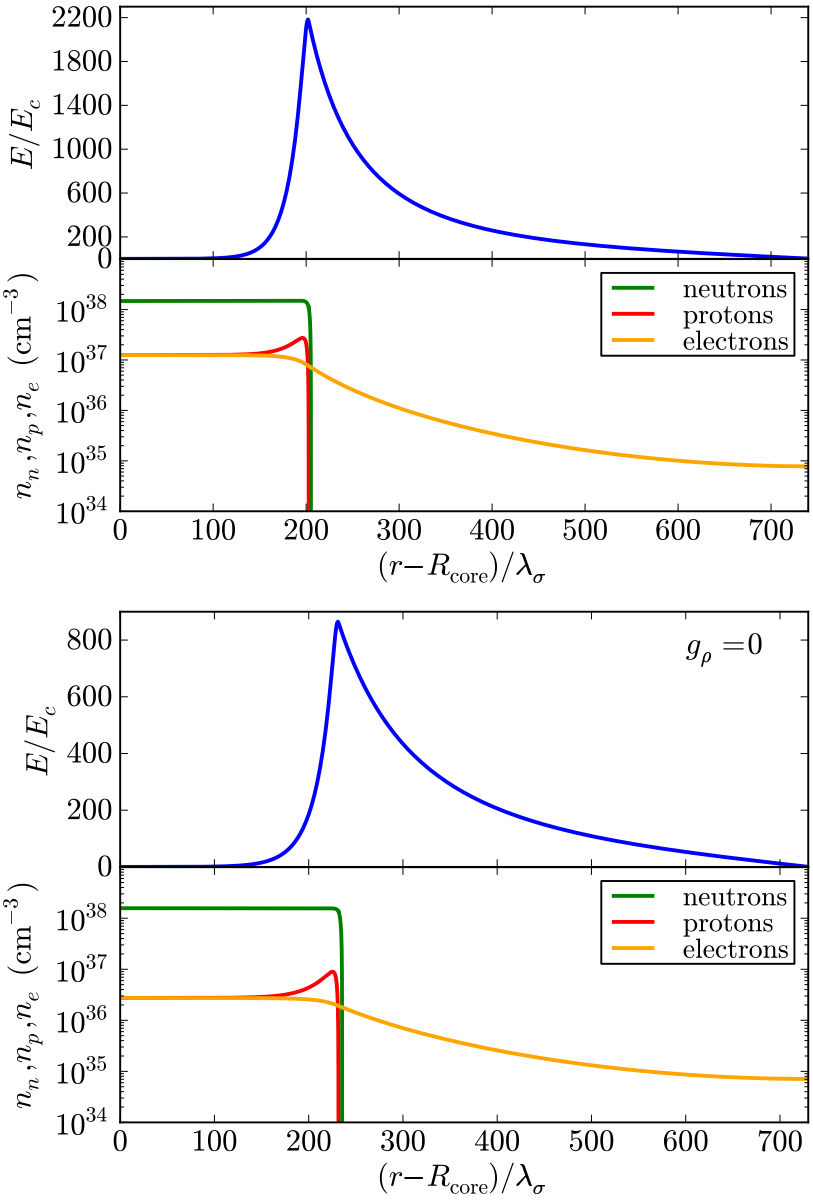

Figure 2.1: Upper panel: electric field in the core-crust transition layer in units of the critical field E_c. Lower panel: particle density profiles in the core-crust boundary interface in units of cm^{-3}. Here we use the NL3-model of Table 2.1 and $\lambda_\sigma = \hbar/(m_\sigma c) \sim 0.4$ fm denotes the sigma-meson Compton wavelength. The density at the edge of the crust in this example is $\rho_{\rm crust} = \rho_{\rm drip} = 4.3 \times 10^{11}$ g/cm^3. Upper plot: $g_\rho \neq 0$. Lower plot: the same as in the upper plot, but setting $g_\rho = 0$, in order to see the effects of the ρ-meson with respect to the case $g_\rho \neq 0$.

et al. (2011). The region "III" is characterized by a smooth decreasing of the electron density which resembles the behavior of the electrons surrounding a nucleus in the Thomas-Fermi model.

The matching to the crust must be done at a radius $R_{\rm core}+\delta R$ where full charge neutrality of the core is reached. Different thicknesses δR correspond to different electron Fermi energies E_e^F. The thickness of the core-crust transition boundary layer δR as well as the value of the electron density at the edge of the crust, $n_e^{\rm crust} = n_e(R_{\rm core}+\delta R)$, depend on the nuclear parameters, especially on the nuclear surface tension.

The equilibrium conditions given by the constancy of the Klein potentials (2.9)–(2.11) throughout the configuration, impose in the transition layer the following continuity condition

$$E_e^F = e^{\nu_{\rm core}/2}\mu_e^{\rm core} - eV^{\rm core} = e^{\nu_{\rm crust}/2}\mu_e^{\rm crust}\,, \tag{2.24}$$

where $\mu_e^{\rm core} = \mu_e(R_{\rm core})$, $eV^{\rm core} = eV(R_{\rm core})$, and $\mu_e^{\rm crust} = \mu_e(R_{\rm core}+\delta R)$, and $e^{\nu_{\rm crust}} \simeq e^{\nu_{\rm core}}$.

In the boundary interface, the electron chemical potential and the density decrease: $\mu_e^{\rm crust} < \mu_e^{\rm core}$ and $\rho_{\rm crust} < \rho_{\rm core}$. For each central density, an entire family of core-crust interface boundaries exist each one with a specific value of δR: the larger the $\rho_{\rm crust}$, the smaller the δR. Correspondingly, an entire family of crusts with different mass and thickness, exist. From the continuity of the electron Klein potential in the boundary interface given by Eq. (2.24), it follows that different values of $\rho_{\rm crust} \geq 0$ correspond to different values of the electron Fermi energy $E_e^F \geq 0$. In close analogy to the compressed atoms studied by Rotondo et al. (2011b), the case $E_e^F = 0$ corresponds to the "free" (uncompressed) configuration, where $\delta R \to \infty$ and $\rho_{\rm crust} = 0$, i.e. a bare core. In this configuration the electric field reaches its maximum value. The case $E_e^F > 0$ is analogous to the one of the compressed atom (Rotondo et al., 2011b). In Fig. 2.2 we have plotted the electron distribution in the core-crust boundary interface for selected densities at the edge of the crust $\rho_{\rm crust} = [\rho_{\rm drip}, 10^{10}, 10^9]$ g/cm^3, where $\rho_{\rm drip} \sim 4.3\times 10^{11}$ g/cm^3 is the neutron drip density.

The configuration with $\rho_{\rm crust} = \rho_{\rm drip}$ separates neutron stars with and without inner crust. In the so-called inner crust, the neutrons dripped from the nuclei in the crust form a fluid that coexist with the nuclei lattice and the degenerate electrons Baym et al. (1971).

For definiteness, we present in this work the results for configurations $\rho_{\rm crust} \leq \rho_{\rm drip}$, i.e for neutron stars possessing only outer crust. The construction of configurations with $\rho_{\rm crust} > \rho_{\rm drip}$ needs to be studied in more detail and will be the subject of a forthcoming work.

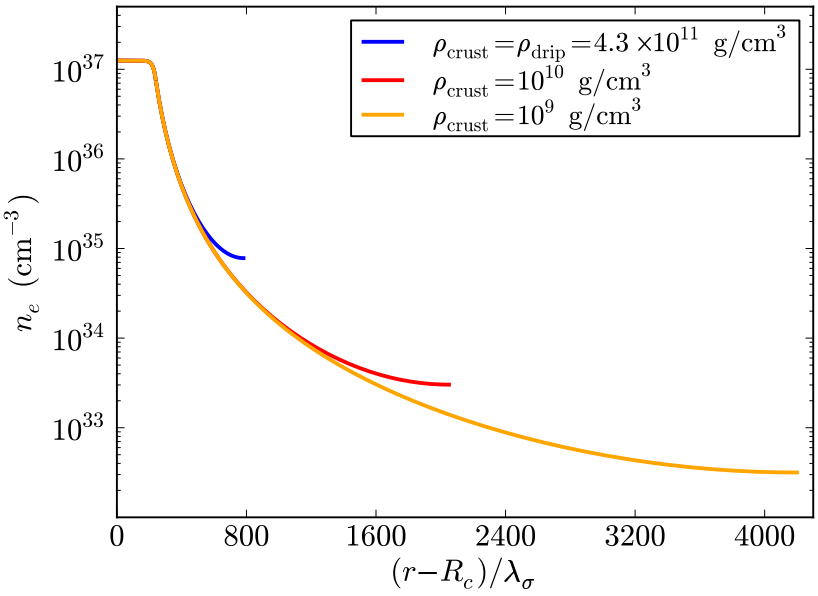

Figure 2.2: Distribution of electrons in the core-crust boundary interface for different densities at the edge of the crust, $\rho_{\rm crust}$. The larger the $\rho_{\rm crust}$, the smaller the electric field E and the smaller the thickness of the interface δR.

2.2.3 Crust Equations

Turning now to the crust, it is clear from the recent treatment of white dwarfs by Rotondo et al. (2011a) that also this problem can be solved by the adoption of Wigner-Seitz cells, and from the relativistic Feynman-Metropolis-Teller (RFMT) approach (Rotondo et al., 2011b) it follows that the crust is clearly neutral. Thus, the structure equations to be integrated are the TOV equations

$$\frac{d\mathcal{P}}{dr} = -\frac{G(\mathcal{E}+\mathcal{P})(M+4\pi r^3\mathcal{P})}{r^2(1-\frac{2GM}{r})}\,, \tag{2.25}$$

$$\frac{dM}{dr} = 4\pi r^2\mathcal{E}\,, \tag{2.26}$$

where $M = M(r)$ is the mass enclosed at the radius r and $\mathcal{E}$ and $\mathcal{P}$ are the energy density and the pressure of the system respectively.

The effects of the Coulomb interaction in "solid"-like electron-ion systems appears only at the microscopic level e.g. Debye-Hueckel screening in classical systems (Debye and Hückel, 1923) and Thomas-Fermi screening in the degenerate case (Mott, 1936). In order to analyze the effects of the microscopic screening on the structure of the configuration we will consider two equations

of state for the crust: the locally neutral case or uniform approximation (see e.g. Chandrasekhar (1931)) and, for simplicity, instead of using the RFMT EOS (Rotondo et al., 2011b), we use as second EOS the one due to Baym, Pethick and Sutherland (BPS) (Baym et al., 1971), which is by far the most used equation of state in literature for the description of the neutron star crust (see e.g. Haensel et al. (2007)).

In the uniform approximation, both the degenerate electrons and the nucleons distribution are considered constant inside each cell of volume $V_{\rm ws}$. This kind of configuration can be obtained only imposing microscopically the condition of local charge neutrality

$$n_e = \frac{Z}{V_{\rm ws}}\,. \tag{2.27}$$

The total pressure of the system is assumed to be entirely due to the electrons, i.e.

$$\mathcal{P} = \mathcal{P}_e = \frac{2}{3\,(2\pi\hbar)^3}\int_0^{P_e^F} \frac{c^2p^2 4\pi p^2}{\sqrt{c^2p^2+m_e^2c^4}}dp\,, \tag{2.28}$$

while the total energy-density of the system is due to the nuclei, i.e. $\mathcal{E} = (A/Z)m_N n_e$, where m_N is the nucleon mass.

We turn now to the BPS equation of state. The first correction to the uniform model, corresponds to abandon the assumption of the electron-nucleon fluid through the so-called "lattice" model which introduces the concept of Wigner-Seitz cell: each cell of radius $R_{\rm ws}$ contains a point-like nucleus of charge $+Ze$ with A nucleons surrounded by a uniformly distributed cloud of Z fully-degenerate electrons.

The sequence of the equilibrium nuclides present at each density in the BPS equation of state is obtained by looking for the nuclear composition that minimizes the energy per nucleon for each fixed nuclear composition (Z, A) (see Table 2.2 and Baym et al. (1971) for details). The pressure $\mathcal{P}$ and the energy-density $\mathcal{E}$ of the system are, within this model, given by

$$\mathcal{P} = \mathcal{P}_e + \frac{1}{3}W_L n_N\,, \tag{2.29}$$

$$\frac{\mathcal{E}}{n_b} = \frac{W_N + W_L}{A} + \frac{\mathcal{E}_e(n_b Z/A)}{n_b}\,, \tag{2.30}$$

where the electron energy-density is given by

$$\mathcal{E}_e = \frac{2}{(2\pi)^3}\int_0^{P_e^F} \sqrt{p^2+m_e^2}\,4\pi p^2 dp\,, \tag{2.31}$$

and $W_N(A, Z)$ is the total energy of an isolated nucleus given by the semi-empirical formula

$$W_N = m_n c^2 (A - Z) + m_p c^2 Z - bA\,, \tag{2.32}$$

with b being the Myers and Swiatecki binding energy per nucleon (Myers, 1966). The lattice energy per nucleus W_L is given by

$$W_L = -\frac{1.819620 Z^2 e^2}{a}\,, \tag{2.33}$$

where the lattice constant a is related to the nucleon density n_N by $n_N a^3 = 2$.

2.3 Neutron Star Structure

In the traditional TOV treatment the density and the pressure are a priori assumed to be continuous as well as the local charge neutrality of the system. The distinguishing feature of the new solution presented in this thesis is that the Klein potentials are constant throughout the three regions; the core, the crust and the transition interface boundary. An overcritical electric field is formed and consequently a discontinuity in density is found with a continuous total pressure including the surface tension of the boundary. In Fig. 2.3, we compare and contrast the density profiles of configurations obtained from the traditional TOV treatment and with the treatment presented here.

In Figs. 2.4–2.10 we show the results of the numerical integration of the system of the general relativistic constitutive equations of the configuration from the center all the way up to the surface with the appropriate boundary conditions between the involved phases. In particular, we have plotted the mass-radius relation as well as the compactness of the neutron stars obtained with the models listed in Table 2.1.

It is worth to note that the inclusion of the Coulomb interaction and in particular the presence of the negative lattice energy W_L results in a decreasing of the pressure of the cells. Such an effect, as shown in Fig. 2.7–2.10, leads to a decreasing of the mass and the thickness of the crust with respect to the uniform-approximation case where no Coulomb interactions are taken into account.

Comparing the mass and the thickness of the crust obtained with these two different EOS, we obtain systematically crusts with smaller mass and larger thickness when Coulomb interactions are taken into account. This results are in line with the recent results in Rotondo et al. (2011a), where the mass-radius relation of white-dwarfs has been calculated using an EOS

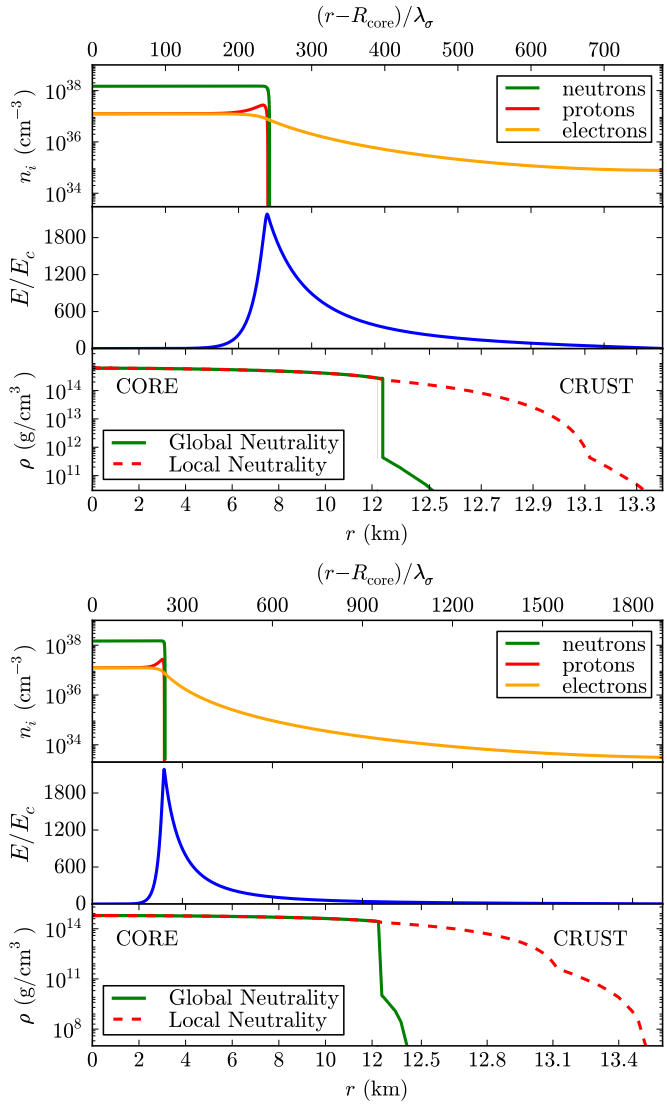

Figure 2.3: Upper panel: electric field in the core-crust transition layer, in units of the critical field E_c. Middle panel: particle density profiles in the core-crust boundary interface, in units of cm^{-3}. Lower panel: density profile inside a neutron star with central density $\rho(0) \sim 5\rho_{\rm nuc}$. We compare and contrast the structural differences between the solution obtained from the traditional TOV equations (locally neutral case) and the globally neutral solution presented here. We use here the NL3 nuclear parametrization of Table 2.1 and $\lambda_\sigma = \hbar/(m_\sigma c) \sim 0.4$ fm, denotes the sigma-meson Compton wavelength. Upper plot: the density at the edge of the crust is $\rho_{\rm crust} = \rho_{\rm drip} = 4.3 \times 10^{11}$ g/cm^3. Lower plot: the density at the edge of the crust is $\rho_{\rm crust} = 10^{10}$ g/cm^3.

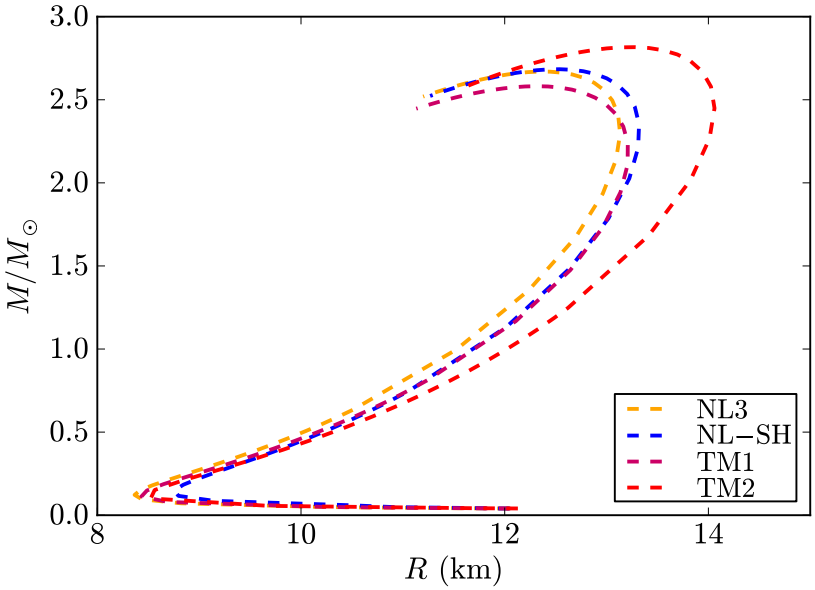

Figure 2.4: Mass-Radius relation for the neutron stars obtained with the nuclear models listed in Table 2.1. In the crust we have used the BPS equation of state. The mass is given in solar masses and the radius in km.

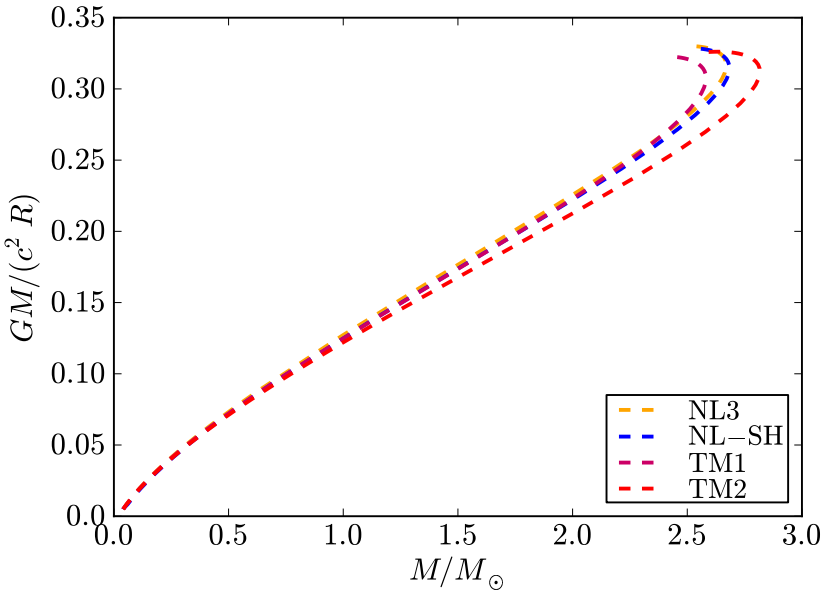

Figure 2.5: Compactness of the star $GM/(c^2R)$ as a function of the star mass M. In the crust we have used the BPS equation of state and the nuclear models are in Table 2.1.

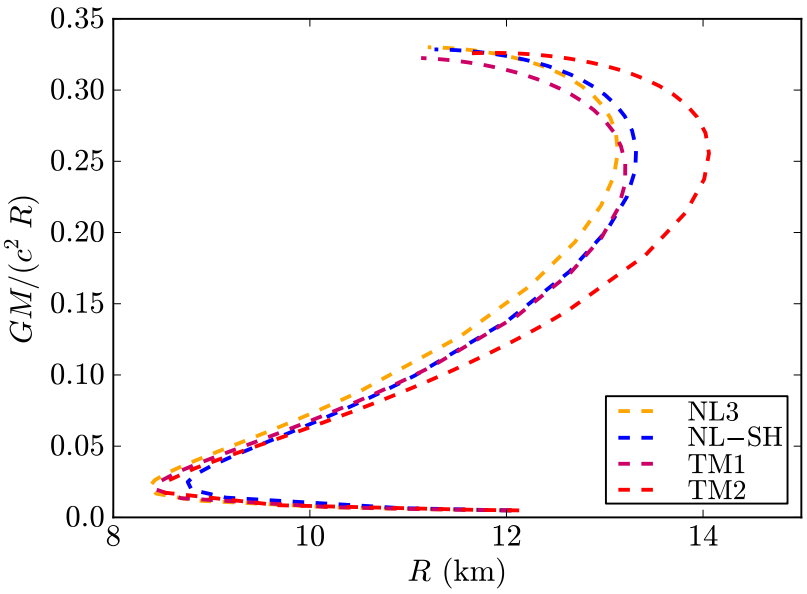

Figure 2.6: Compactness of the star $GM/(c^2R)$ as a function of the star radius R. In the crust we have used the BPS equation of state and the nuclear models are in Table 2.1.

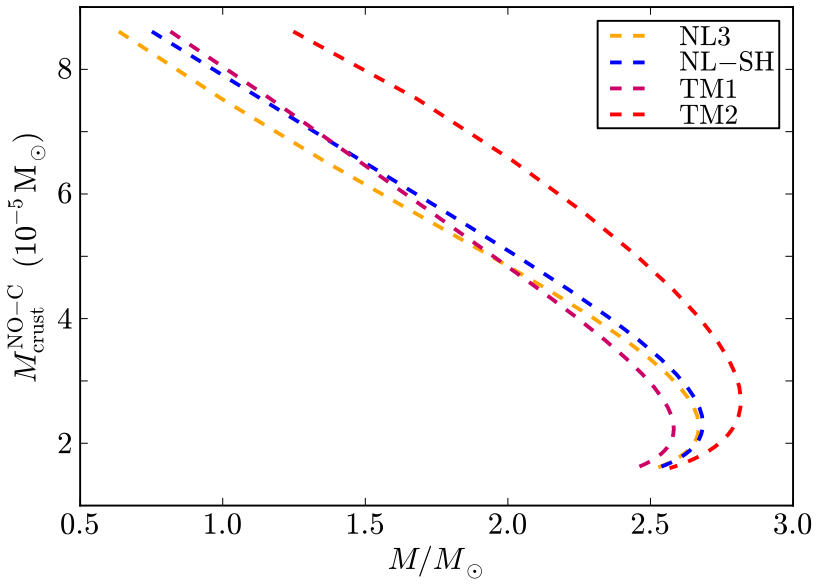

Figure 2.7: Mass of the crust as a function of the compactness for the crust EOS without Coulomb interactions.

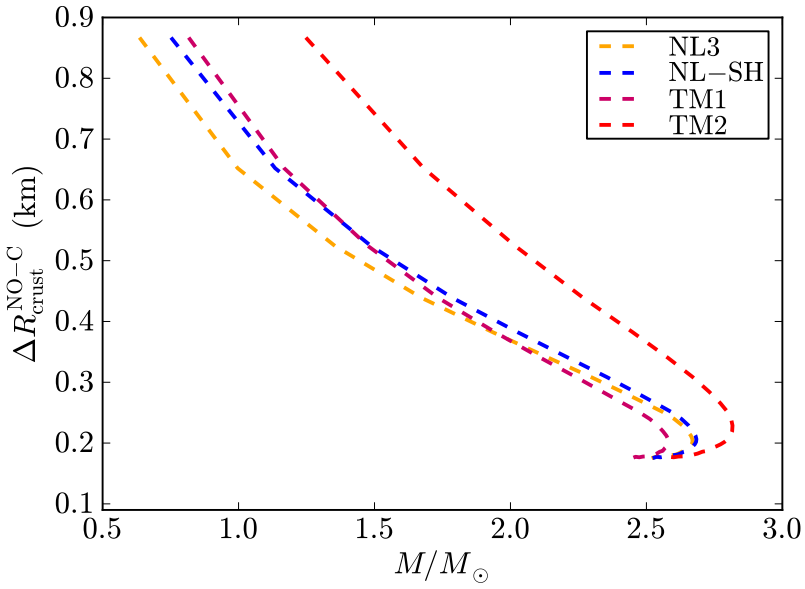

Figure 2.8: Crust-thickness as a function of the compactness for the crust EOS without Coulomb interactions.

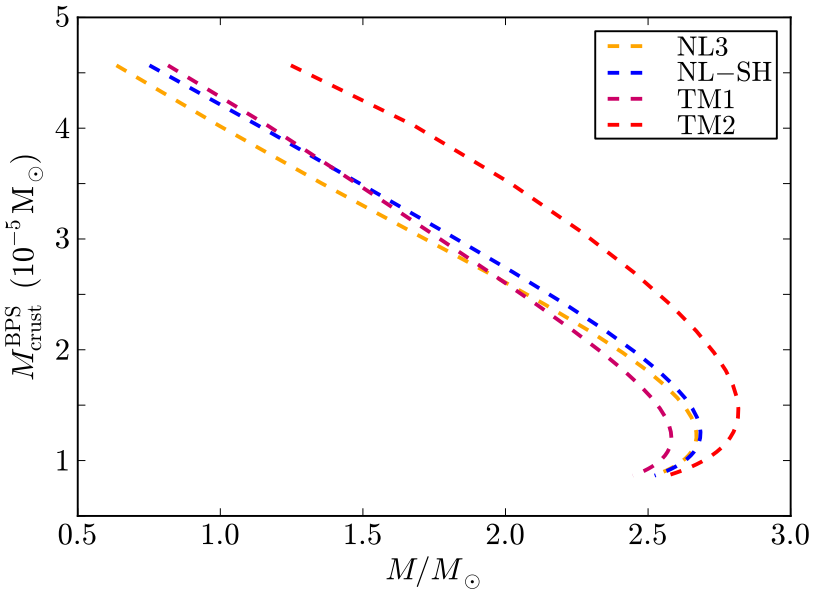

Figure 2.9: Crust mass as a function of the compactness for crust with the BPS EOS.

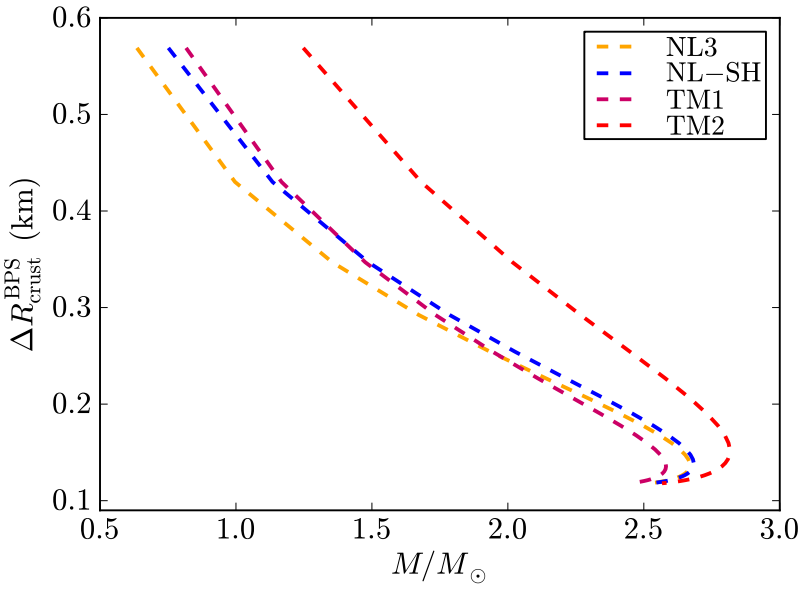

Figure 2.10: Crust thickness as a function of the compactness for crust with the BPS EOS.

based on the relativistic Feynman-Metropolis-Teller model for compressed atoms Rotondo et al. (2011b).

In the case of the BPS EOS, the average nuclear composition in the outer crust, namely the average charge to mass ratio of nuclei Z/A, is obtained by calculating the contribution of each nuclear composition present to the mass of the crust. We exemplified the analysis for two different cores: $M_{\rm core} = 2.56 M_\odot$, $R_{\rm core} = 12.79$ km; $M_{\rm core} = 1.35 M_\odot$, $R_{\rm core} = 11.76$ km.

The relative abundance of each nuclide within the crust of the star can be obtained as

$$\text{R.A.} = \frac{1}{M^{\rm BPS}_{\rm crust}} \int_{\Delta r} 4\pi r^2 \mathcal{E} dr \,, \tag{2.34}$$

where the integration is carried out in the layer of thickness Δr where the particular nuclide is present; see Table 2.2 and Fig. 2.11. Our results are in agreement with the analysis on the neutron star crust composition obtained in (Goriely et al., 2011; Pearson et al., 2011). In both cases we obtain as average nuclear composition $^{105}_{35}$Br. The corresponding crusts with fixed nuclear composition $^{105}_{35}$Br for the two chosen cores are calculated neglecting Coulomb interactions (i.e. using the first EOS). The mass and the thickness of these crusts with fixed $^{105}_{35}$Br are different with respect to the ones obtained using the full BPS EOS, leading to such average nuclear composition. For the two selected examples we obtain that the mass and the thickness of the

crust with average $^{105}_{35}$Br are, respectively, 18% larger and 5% smaller with respect to the ones obtained with the corresponding BPS EOS. This result shows how small microscopic effects due to the Coulomb interaction in the crust of the neutron star leads to quantitative not negligible effects on the macroscopic structure of the configuration.

Equilibrium Nuclei Below Neutron Drip						
Nucleus	Z	ρ_{max}(g cm^{-3})	$\Delta\ R_1$ (km)	R.A.1(%)	$\Delta\ R_2$ (km)	R.A.2(%)
^{56}Fe	26	8.1×10^6	0.0165	7.56652×10^{-7}	0.0064	6.96927×10^{-7}
^{62}Ni	28	2.7×10^8	0.0310	0.00010	0.0121	0.00009
^{64}Ni	28	1.2×10^9	0.0364	0.00057	0.0141	0.00054
^{84}Se	34	8.2×10^9	0.0046	0.00722	0.0017	0.00683
^{82}Ge	32	2.2×10^{10}	0.0100	0.02071	0.0039	0.01983
^{80}Zn	38	4.8×10^{10}	0.1085	0.04521	0.0416	0.04384
^{78}Ni	28	1.6×10^{11}	0.0531	0.25635	0.0203	0.25305
^{76}Fe	26	1.8×10^{11}	0.0569	0.04193	0.0215	0.04183
^{124}Mo	42	1.9×10^{11}	0.0715	0.02078	0.0268	0.02076
^{122}Zr	40	2.7×10^{11}	0.0341	0.20730	0.0127	0.20811
^{120}Sr	38	3.7×10^{11}	0.0389	0.23898	0.0145	0.24167
^{118}Kr	36	4.3×10^{11}	0.0101	0.16081	0.0038	0.16344

Table 2.2: ρ_{max} is the maximum density at which the nuclide is present;$\Delta\ R_1$, $\Delta\ R_2$ and R.A.1(%), R.A.2(%) are respectively the thickness of the layer where a given nuclide is present and their relative abundances in the outer crust for two different cases: $M_{\rm core} = 2.56 M_\odot$, $R_{\rm core} = 12.79$ km; $M_{\rm core} = 1.35 M_\odot$, $R_{\rm core} = 11.76$ km.

2.4 Observational Constraints on the Static Mass-Radius Relation

It has been recently pointed out that the most up-to-date stringent constraints to the mass-radius relation of neutron stars are provided by the largest mass, the largest radius, the highest rotational frequency, and the maximum surface gravity, observed for pulsars (Trümper, 2011a).

So far, the highest neutron star mass measured with a high level of experimental confidence, until 2013, has been the mass of the 3.15 millisecond pulsar PSR J1614–2230, $M = (1.97 \pm 0.04) M_\odot$, obtained from the Shapiro time delay and the Keplerian orbital parameters of the binary system (Demorest et al., 2010). However, recently, Antoniadis et al. (2013) gave an even more stringent constraint to the nuclear EOS of a neutron star, due to the reported mass $(2.01 \pm 0.04) M_\odot$ in the relativistic binary system PSR J0348+0432. The fitting of the thermonuclear burst oscillation light curves

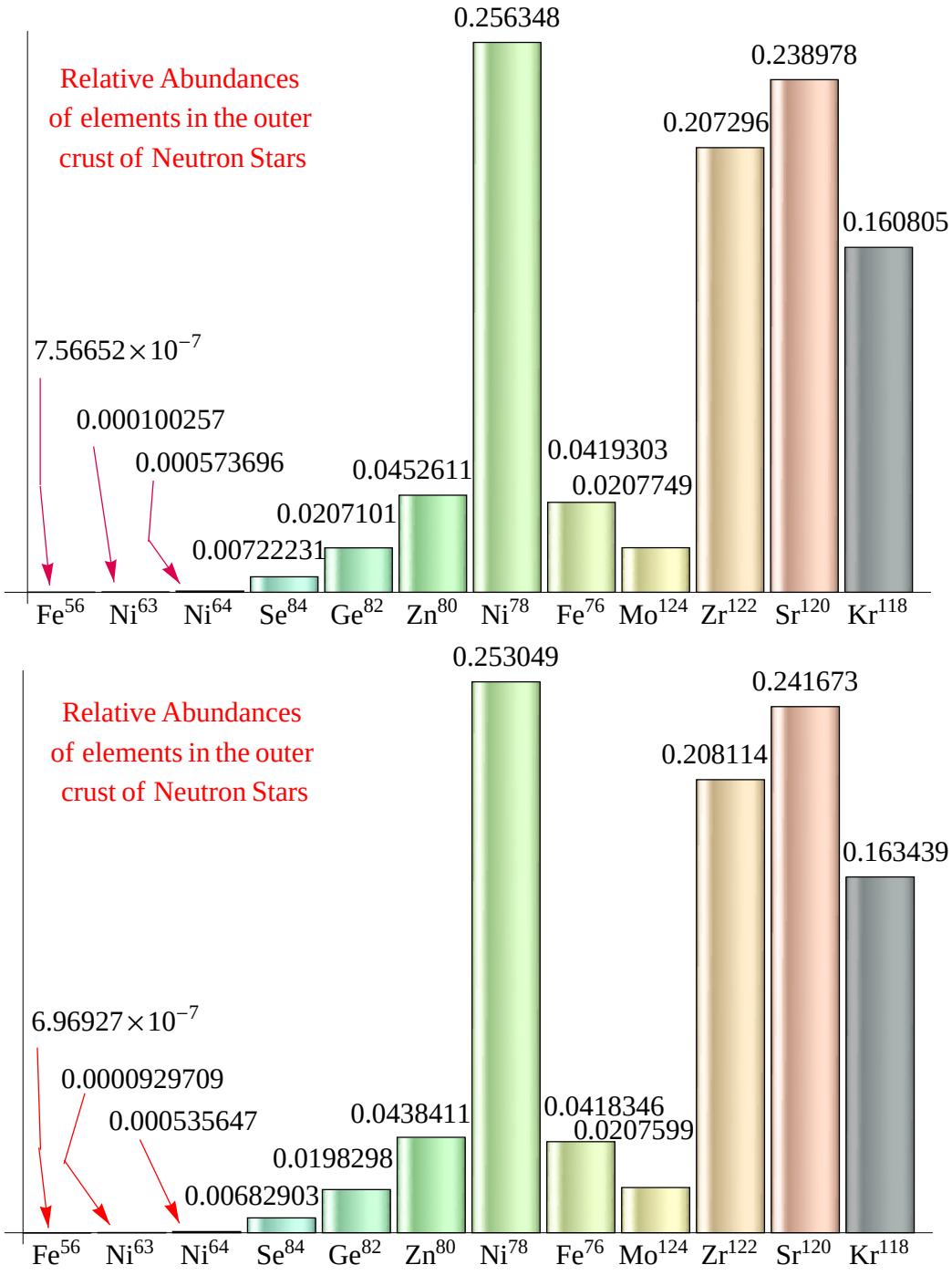

Figure 2.11: Relative abundances of chemical elements in the crust for the two cores analyzed in Table 2.2

from the accreting millisecond pulsar XTE J1814–338 weakly constrain the mass-radius relation imposing an upper limit to the surface gravity of the neutron star, $GM/(c^2R) < 0.24$ (Bhattacharyya et al., 2005). A lower limit of the radius of RX J1856–3754, as seen by an observer at infinity $R_\infty = R[1-2GM/(c^2R)]^{-1/2} > 16.8$ km, has been obtained from the fit of the optical and X-ray spectra of the source (Trümper et al., 2004); it gives the constraint $2GM/c^2 > R - R^3/(R_\infty^{\rm min})^2$, being $R_\infty^{\rm min} = 16.8$ km. Assuming a neutron star of $M = 1.4M_\odot$ to fit the Chandra data of the low-mass X-ray binary X7, it turns out that the radius of the star satisfies $R = 14.5^{+1.8}_{-1.6}$ km, at 90% confidence level, corresponding to $R_\infty = [15.64, 18.86]$ km, respectively (see Heinke et al. (2006) for details). The maximum rotation rate of a neutron star taking into account both the effects of general relativity and deformations has been found to be $\nu_{\rm max} = 1045(M/M_\odot)^{1/2}(10\,{\rm km}/R)^{3/2}$ Hz, largely independent of the equation of state (Lattimer and Prakash, 2004). The fastest observed pulsar is PSR J1748–2246ad with a rotation frequency of 716 Hz (Hessels et al., 2006), which results in the constraint $M \geq 0.47(R/10\,{\rm km})^3 M_\odot$. In Fig. 2.12 are shown all these constraints and the mass-radius relation presented in this chapter.

As discussed by J. E. Trümper in (Trümper, 2011a), the above constraints strongly favor stiff equations of state which provide high maximum masses for neutron stars. In addition, putting all of them together, the radius of a canonical neutron star of mass $M = 1.4M_\odot$ is highly constrained to the range $R \gtrsim 12$ km disfavoring, at the same time, the strange quark hypothesis for these specific objects. It is clear from Fig. 2.12 that the mass-radius relation presented here is consistent with all the observation constraints, for all the nuclear parametrizations of Table 2.1. In Table 2.3 are presented the radii predicted by the new mass-radius relation (presented in this chapter and in (Belvedere et al., 2012)) for a canonical neutron star of $M = 1.4M_\odot$ as well as for the millisecond pulsar PSR J1614–2230, $M = (1.97 \pm 0.04)M_\odot$.

$M(M_\odot)$	$R_{\rm NL3}$	$R_{\rm NL-SH}$	$R_{\rm TM1}$	$R_{\rm TM2}$
1.40	12.31	12.47	12.53	12.93
1.93	12.96	13.14	13.13	13.73
2.01	13.02	13.20	13.17	13.82

Table 2.3: Radii (in km) predicted by the nuclear parametrizations NL3, NL-Sh, TM1 and TM2 of Table 2.1, for a canonical neutron star of $M = 1.4M_\odot$ and for the millisecond pulsar PSR J1614–2230, $M = (1.97 \pm 0.04)M_\odot$.

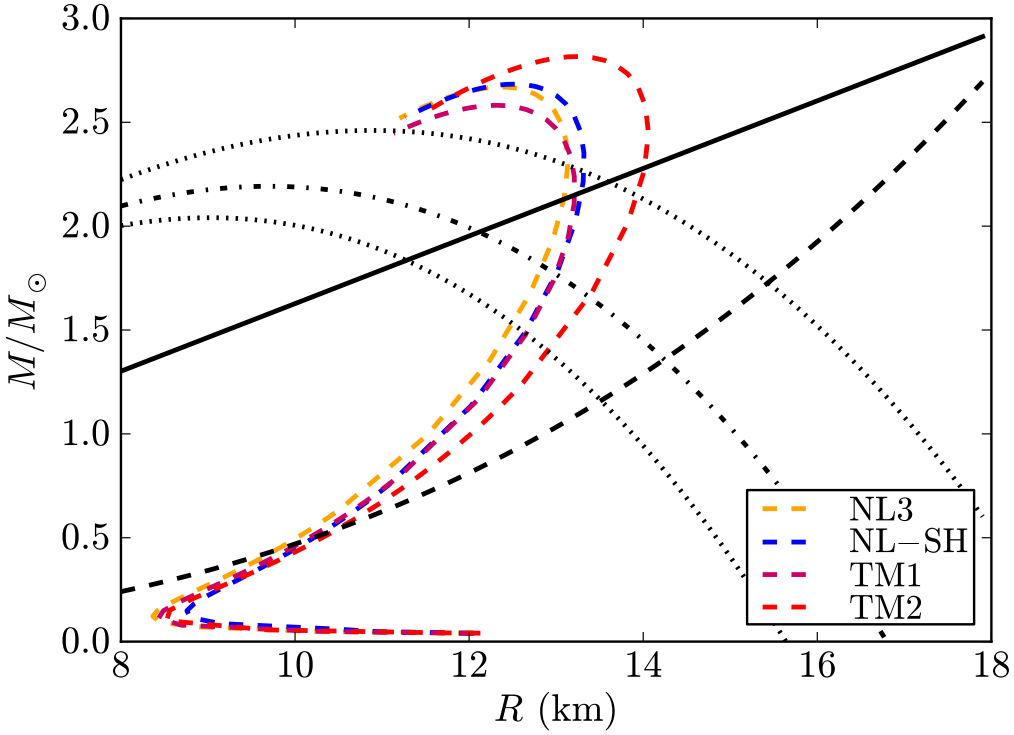

Figure 2.12: Constraints on the mass-radius relation given by J. E. Trümper in Trümper (2011a) and the theoretical mass-radius relation presented in this chapter (and in (Belvedere et al., 2012)) in Fig. 2.4. The solid line is the upper limit of the surface gravity of XTE J1814–338, the dotted-dashed curve corresponds to the lower limit to the radius of RX J1856–3754, the dashed line is the constraint imposed by the fastest spinning pulsar PSR J1748–2246ad, and the dotted curves are the 90% confidence level contours of constant R_∞ of the neutron star in the low-mass X-ray binary X7. Any mass-radius relation should pass through the area delimited by the solid, the dashed and the dotted lines and, in addition, it must have a maximum mass larger than the mass of PSR J0348+0432, $M = (2.01 \pm 0.04)M_\odot$.

2.5 Comparison with the Traditional TOV Treatment

In the traditional TOV treatment local charge neutrality as well as the continuity of the pressure and the density in the core-crust transition are assumed. This leads to explicit violation of the constancy of the Klein potentials throughout the configuration (see e.g. Rotondo et al. (2011c)). In such a case there is a smooth transition from the core to the crust without any density discontinuity and therefore the density at the edge of the crust is $\sim \rho_{\rm nuc} \sim 2.7 \times 10^{14}$ g/cm^3. The so-called inner crust in those configurations extends in the range of densities $\rho_{\rm drip} \lesssim \rho \lesssim \rho_{\rm nuc}$ while, at densities $\rho \lesssim \rho_{\rm drip}$, there is the so-called outer crust.

In Figs. 2.13 and 2.14 we compare and contrast the mass and the thickness of the crust as obtained from the traditional TOV treatment with the new configurations presented here, discussed previously in Secs. 2.2 and 2.3 characterized by $\rho_{\rm crust} = \rho_{\rm drip}$.

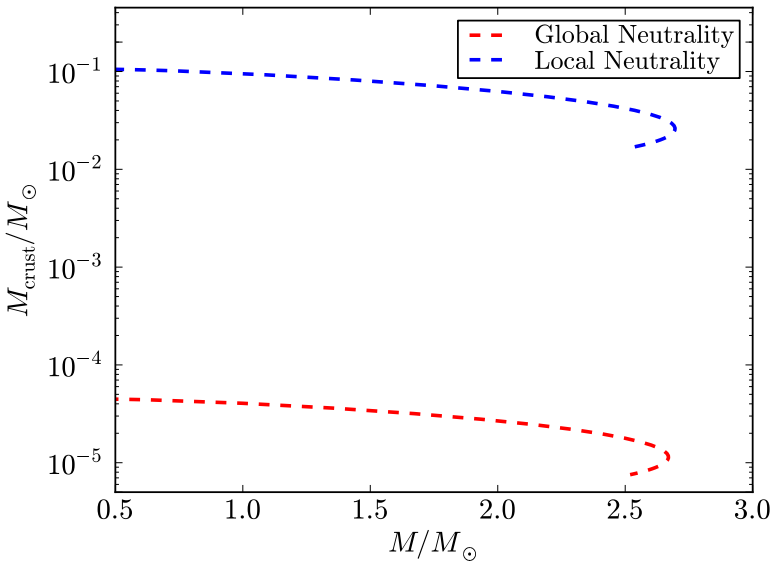

Figure 2.13: Mass of the crust given by the traditional locally neutral Tolman-Oppenheimer-Volkoff treatment and by the new globally neutral equilibrium configurations presented in this article. We use here the NL3 nuclear model, see Table 2.1.

The markedly differences both in mass and thickness of the crusts (see Figs. 2.13 and 2.14) obtained from the traditional Tolman-Oppenheimer-Volkoff approach and the new equilibrium configurations presented here,

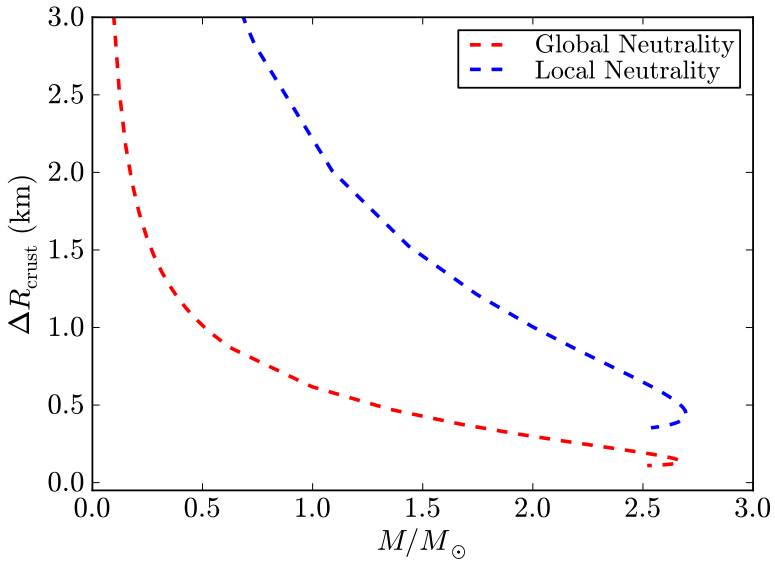

Figure 2.14: Thickness of the crust given by the traditional locally neutral Tolman-Oppenheimer-Volkoff treatment and by the new globally neutral equilibrium configurations presented in this article. We use here the NL3 nuclear model, see Table 2.1.

leads to a very different mass-radius relations which we compare and contrast in Fig. 2.15.

2.6 Conclusions

We have formulated the equations of equilibrium of neutron stars based on the recent works by Rueda et al. (2011) and Rotondo et al. (2011b,a,c). The strong, weak, electromagnetic, and gravitational interactions are taken into due account within the framework of general relativity. In particular, the strong interactions between nucleons is described by the exchange of the σ, ω, and ρ mesons. The equilibrium conditions are given by the set of Einstein-Maxwell-Thomas-Fermi equations and by the constancy of the general relativistic Fermi energies of particles, the Klein potentials, throughout the configuration.

We have solved these equilibrium equations numerically, in the case of zero temperatures, for the nuclear parameter sets NL3 Lalazissis et al. (1997), NL-SH Sharma et al. (1993), TM1 Sugahara and Toki (1994), and TM2 Hirata et al. (1995); see Table 2.1 for details.

A new structure of the star is found: the positively charged core at

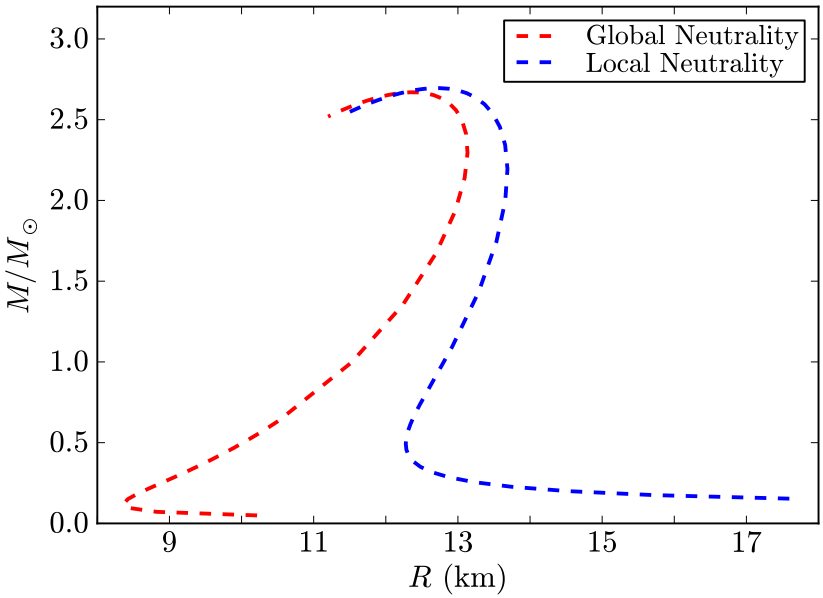

Figure 2.15: Mass-Radius relation obtained with the traditional locally neutral TOV treatment and with the new globally neutral equilibrium configurations presented here. We use here the NL3 nuclear model, see Table 2.1.

supranuclear densities is surrounded by an electronic distribution of thickness $\gtrsim \hbar/(m_e c) \sim 10^2 \hbar/(m_\pi c)$ of opposite charge and, at lower densities, a neutral ordinary crust.

In the core interior the Coulomb potential well is $\sim m_\pi c^2/e$ and correspondingly the electric field is $\sim (m_p/m_{\rm Planck})(m_\pi/m_e)^2 E_c \sim 10^{-14} E_c$. Due to the equilibrium condition given by the constancy of the Klein potentials, there is a discontinuity in the density at the transition from the core to the crust, and correspondingly an overcritical electric field $\sim (m_\pi/m_e)^2 E_c$ develops in the boundary interface; see Fig. 2.1 [1].

The continuity of the Klein potentials at the core-crust boundary interface leads to a decreasing of the electron chemical potential and density, until values $\mu_e^{\rm crust} < \mu_e^{\rm core}$ and $\rho_{\rm crust} < \rho_{\rm core}$ at the edge of the crust, where global charge neutrality is achieved. For each central density, an entire family of core-crust interface boundaries and, correspondingly, an entire family of crusts with different mass and thickness, exist. The larger $\rho_{\rm crust}$, the smaller the thickness of the interface, the peak of the electric field, and

[1] This strong electric field reminds the one studied in the stability of charged nuclear cores against vacuum polarization; see e.g. Müller and Rafelski (1975); Migdal et al. (1976, 1977); Rotondo et al. (2008).

the larger the mass and the thickness of the crust. The configuration with $\rho_{\rm crust} = \rho_{\rm drip} \sim 4.3 \times 10^{11}$ g/cm^3 separates neutron stars with and without inner crust. The neutron stars with $\rho_{\rm crust} > \rho_{\rm drip}$ deserve a further analysis in order to account for the reduction of the nuclear tension at the core-crust transition due to the presence of dripped neutrons from the nuclei in the crust.

All the above new features lead to crusts with masses and thickness smaller than the ones obtained from the traditional TOV treatment, and we have shown specifically neutron stars with $\rho_{\rm crust} = \rho_{\rm drip}$; see Figs. 2.13–2.14. The mass-radius relation obtained in this case have been compared and contrasted with the one obtained from the locally neutral TOV approach; see Fig. 2.15. We have shown that this new mass-radius relation is in line with observations, based on the recent work by J. E. Trümper Trümper (2011a); see Fig. 2.12 for details.

2.7 Perspectives

The results of this chapter could be extended to different models for the strong interactions. For example, it is possible to extend RMFT either introducing higher order couplings or by mean density-dependent couplings. These extensions have strong impact in the high-density regime. The values of the nuclear matter incompressibility coefficient for the standard σ-ω-ρ non linear models are usually larger on respect to their values obtained through the experimental data on isoscalar giant monopole resonances. At the same time, the symmetry energy coefficient and its density dependence are higher relative to the corresponding empirical estimates. It is possible to overcome these issues through the field-theoretical-based relativistic mean-field (FTRMF) model, which includes self and mixed interaction terms for σ, ω, and ρ mesons up to the quartic order. In particular, mixed interaction terms involving the ρ-meson field enables one to vary the density dependence of the symmetry energy coefficient and the neutron skin thickness in heavy nuclei over a wide range without affecting the other properties of finite nuclei, while the contribution from the self-interaction of ω mesons is important in varying the high-density behavior of the EOS and prevents instabilities in the calculation of the EOS itself; (see e.g. Dhiman et al., 2007, and references therein). Extended RMFT models are useful to study the crust of the neutron stars too, as shown for example in (Gupta and Arumugam, 2013), where they have been used to describe the phase transition from the non-uniform matter of the inner crust at densities lower than the nuclear one, to the uniform matter in the neutron star core. Moreover, it would be interesting to analyze what

it happens at high density once isospin-antisymmetric matter is taken into account. In such a case, the contribution of δ-meson could be important and influence the properties of dense matter (Kubis and Kutschera, 1997a,b).

An important tool to understand the EOS of the matter at nuclear density, to analyze the instabilities of the neutron stars, as well as to prove or discard the strange and the quark stars hypothesis (Zheng et al., 2007), is the study of oscillations, namely the neutron star modes; (for an extended review see e.g. Stergioulas, 2003, and references therein).

An open issue about our work is related to the minimum energy configuration. More precisely, in this chapter we compared and contrasted the TOV-like solution, in which local charge neutrality applies with our new EMTF solution, in which global charge neutrality applies. In the former, there is no electric field and in its surface, and the crust has both inner and outer crusts, while in the latter the core is charged, an overcritical electric field appear in the thin transition layer in between the core and the crust, and the inner crust might disappear due to the fast decreasing of the matter density in the transition layer. As mentioned in section 2.1, there can exist two kind of possible sub-configurations: the configuration with $\rho_{\rm crust} = \rho_{\rm drip}$ separates neutron stars with and without inner crust. In this chapter we faced the configuration for which $\rho_{\rm crust} = \rho_{\rm drip}$, showing examples with $\rho_{\rm crust} < \rho_{\rm drip}$ too. It would be interesting to construct configurations with $\rho_{\rm drip} < \rho_{\rm crust} < \rho_{\rm nuc}$, and consequently to analyze which has the minimum energy, namely, which is the most stable configuration.

In addition, it is of interest to study the effects of the above new structure on the cooling of neutron stars, since the thermal evolution is very sensitive on the mass-radius relation and the properties of strongly compressed hadronic matter (Schramm et al., 2013).

The electromagnetic structure of the neutron star presented here is of clear astrophysical relevance. The process of gravitational collapse of a core endowed with electromagnetic structure leads to signatures and energetics markedly different from the ones of a core endowed uniquely of gravitational interactions; see e.g. Ruffini et al. (2003a,b); Ruffini and Xue (2008); Ruffini et al. (2010).

It is clear that the release of gravitational energy in the process of gravitational collapse of the core, following the classic work of Gamow and Schoenberg (see Gamow and Schoenberg (1941); Arnett et al. (1996)), is carried away by neutrinos. The additional nuclear and electromagnetic energy $\sim 10^{51}$ erg of the collapsing core introduced in this chapter are expected to be carried away by electron-positron plasma created in the overcritical electromagnetic field in the collapsing core.

Chapter 3

Neutron Star Equilibrium Configurations in the Hartle-Thorne Slow-Rotation Approximation

3.1 Introduction

As shown in Chap. 2 (see Rotondo et al., 2011c; Rueda et al., 2011; Belvedere et al., 2012, for details), the equations of Tolman-Oppenheimer-Volkoff (TOV) (Tolman, 1939; Oppenheimer and Volkoff, 1939), traditionally used to describe the neutron star equilibrium configurations, are superseded once the strong, weak, electromagnetic and gravitational interactions are taken into account. Instead, the Einstein-Maxwell system of equations coupled with the general relativistic Thomas-Fermi equations of equilibrium have to be used; what we called the Einstein-Maxwell-Thomas-Fermi (EMTF) system of equations. While in the TOV approach the condition of local charge neutrality, $n_e(r) = n_p(r)$, (being n_i the particle density of the i-species), is imposed (see e.g. Haensel et al., 2007, and references therein), the EMTF approach requests the less stringent condition of global charge neutrality, namely

$$\int \rho_{\rm ch} d^3r = \int e[n_p(r) - n_e(r)] d^3r = 0\,, \tag{3.1}$$

where $\rho_{\rm ch}$ is the charge density, e is the fundamental electric charge, and the integral is carried out on the entire volume of the system.

The Lagrangian density taking into account all the interactions include the free-fields terms $\mathcal{L}_g$, $\mathcal{L}_\gamma$, $\mathcal{L}_\sigma$, $\mathcal{L}_\omega$, $\mathcal{L}_\rho$ (respectively for the gravitational,

the electromagnetic, and the three mesonic fields), the three fermion species (electrons, protons and neutrons) term $\mathcal{L}_f$ and the interacting part in the minimal coupling assumption, $\mathcal{L}_{\rm int}$, as shown in Subsec. 2.2.1, Eq. (2.1) and in Appendix A, Eqs. (A.2)–(A.8), where the description of the strong interactions between the nucleons is made through the σ-ω-ρ nuclear model in the version of Boguta and Bodmer (1977).

As introduced in the previous chapter, the nuclear model is fixed once the values of the coupling constants and the masses of the three mesons are fixed: in this chapter we use the NL3 parameter set Lalazissis et al. (1997): $m_\sigma = 508.194$ MeV, $m_\omega = 782.501$ MeV, $m_\rho = 763.000$ MeV, $g_\sigma = 10.2170$, $g_\omega = 12.8680$, $g_\rho = 4.4740$, plus two constants that give the strength of the self-scalar interactions, $g_2 = -10.4310$ fm^{-1} and $g_3 = -28.8850$; see Tab. 2.1 and (Belvedere et al., 2012) for details.

From the equations of motion of the above Lagrangian we obtain the EMTF equations, see Appendix A and (Rueda et al., 2011; Belvedere et al., 2012) for details. The solution of the EMTF coupled differential equations leads to a new structure of the star, as shown in Fig. 2.1: a positively charged core at supranuclear densities, $\rho > \rho_{\rm nuc} \sim 2.7\times10^{14}$ g cm^{-3}, surrounded by an electron distribution of thickness $\gtrsim \hbar/(m_e c)$ and, at lower densities $\rho < \rho_{\rm nuc}$, a neutral ordinary crust.

The thermodynamic equilibrium is ensured by the constancy of the particle Klein potentials (Klein, 1949) generalized to the presence of electrostatic and strong fields (Rotondo et al., 2011c; Rueda et al., 2011; Belvedere et al., 2012)

$$\frac{1}{u^t}\left[\mu_i + (q_i A_\alpha + g_\omega \omega_\alpha + g_\rho \tau_{3,i} \rho_\alpha) u^\alpha\right] = \text{constant}\,, \tag{3.2}$$

where the subscript i stands for each kind of particle, μ_i is the particle chemical potential, and q_i is the particle electric charge. In the static case only the time components of the vector fields, A_0, ω_0, ρ_0 are present. In the above equation $u^t = (g_{tt})^{-1/2}$ is the time component of the fluid four-velocity which satisfies $u_\alpha u^\alpha = 1$; g_{tt} is the t–t component of the spherically symmetric metric; see Eq. (2.2).

The equilibrium conditions (3.2) lead to a discontinuity in the density at the core-crust transition and, correspondingly, an overcritical electric field $\sim (m_\pi/m_e)^2 E_c$, where $E_c = m_e^2 c^3/(e\hbar) \sim 1.3 \times 10^{16}$ Volt cm^{-1}, appears in the core-crust boundary interface. The constancy of the Klein potentials is necessary to fulfill the requirement of thermodynamical equilibrium, together with the constancy of the gravitationally red-shifted temperature (Tolman condition) (Tolman, 1930; Klein, 1949), if finite temperatures are considered (see e.g. Rueda et al., 2011). In particular, the continuity of the electron Klein potential leads to a decreasing of the electron chemical potential μ_e and

density at the core-crust boundary interface. They reach values $\mu_e^{\rm crust} < \mu_e^{\rm core}$ and $\rho_{\rm crust} < \rho_{\rm core}$ at the base of the crust, where global charge neutrality is achieved.

As it is shown in Fig. 2.15 (see Belvedere et al., 2012, for details), the solution of this new set of equilibrium equations leads to a more compact neutron star with a less massive and thinner crust. Consequently, it gives a new mass-radius relation which markedly differs from the one described through the solution of the TOV equations in the case of local charge neutrality; see Fig. 2.15

We extend in this chapter the previous results to the case in which the neutron star is rotating as a rigid body. To this end we use the Hartle approach (Hartle, 1967) which solves the Einstein equations accurately up to second order approximation in the angular velocity of the star, Ω (see next section 3.2 for details).

In this rotating case, the condition of the constancy of the particle Klein potential has the same form as Eq. (3.2), but the fluid inside the star now moves with a four-velocity of a rigid rotating body, $u^\alpha = (u^t, 0, 0, u^\phi)$, with (see Hartle and Sharp (1967) and Appendix B, for details)

$$u^t = (g_{tt} + 2\Omega\, g_{t\phi} + \Omega^2\, g_{\phi\phi})^{-1/2}, \qquad u^\phi = \Omega u^t\,, \tag{3.3}$$

where ϕ is the azimuthal angular coordinate with respect to which the metric is symmetric, namely the metric is independent of ϕ (axial symmetry). The metric functions $g_{\alpha\beta}$ are now given by Eq. (3.4) below. It is then clear that in a frame comoving with the rotating star, $u^t = (g_{tt})^{-1/2}$, and the Klein equilibrium condition becomes the same as Eq. (3.2), as expected.

We applied the Hartle formalism to the seed static solution obtained from the integration of the EMTF equations (Belvedere et al., 2012). For the construction of the new mass-radius relation we take into account the Keplerian mass-shedding limit and the secular axisymmetric instability (see Sec. 3.3). We compute in Sec. 3.4 the mass M, polar R_p and equatorial $R_{\rm eq}$ radii, angular momentum J, eccentricity ϵ, and quadrupole moment Q, as a function of the central density and the rotation angular velocity Ω of the stable neutron star both in the globally and locally neutral cases. Based on the criteria of equilibrium we calculate the maximum stable neutron star mass and from the gravitational binding energy of the configurations establish the minimum mass under which the neutron star becomes gravitationally unbound. We construct in section 3.5 the new neutron star mass-radius relation. In Sec. 3.6 we calculate the moment of inertia as a function of the central density and total mass of the neutron star. The eccentricity ϵ, the rotational to gravitational energy ratio T/W, and quadrupole moment Q

are shown in section 3.7. The observational constraints on the mass-radius relation are discussed in Sec. 3.8. We finally summarize the results in Sec. 3.9 and suggest some perspectives in Sec. 3.10. We use in this chapter geometric units $G = c = 1$.

3.2 Hartle Slow Rotation Approximation

In his pioneering work, Hartle (1967) computed the equilibrium equations of slowly rotating stars in the context of General Relativity. The solutions of the Einstein equations are obtained through a perturbative method, expanding the metric functions up to the second order in the angular velocity Ω. Under this assumption the structure of compact objects can be approximately described by the total mass M, angular momentum J and quadrupole moment Q. The slow rotation regime implies that the perturbations owing to the rotation are relatively small with respect to the known non-rotating geometry. The interior solution is derived by solving numerically a system of ordinary differential equations for the perturbation functions. The exterior solution for the vacuum surrounding the star, can be written analytically in terms of M, J, and Q (see Hartle, 1967; Hartle and Thorne, 1968, for details). The numerical values for all the physical quantities are derived by matching the interior and the exterior solution on the border of the star.

The spacetime metric for the rotating configuration up to the second order of Ω is given by (Hartle, 1967)

$$\begin{aligned} ds^2 &= e^{\nu}\,(1+2h)\,dt^2 - e^{\lambda}\left[1+\frac{2m}{r-2M_0}\right]dr^2 \\ &\quad -r^2\,(1+2k)\left[d\theta^2+\sin^2\theta\,(d\phi-\omega dt)^2\right]\,, \end{aligned} \tag{3.4}$$

where $\nu = \nu(r)$, $\lambda = \lambda(r)$, and $M_0 = M^{J=0}(r)$ are the metric functions and mass profiles of the corresponding seed non-rotating star with the same central density as the rotating one; see Eq. (2.2). The functions $h = h(r,\theta)$, $m = m(r,\theta)$, $k = k(r,\theta)$ and the fluid angular velocity in the local inertial frame, $\omega = \omega(r)$, have to be calculated from the Einstein equations. Expanding up to the second order the metric in spherical harmonics we have

$$h(r,\theta) = h_0(r) + h_2(r)P_2(\cos\theta)\,, \tag{3.5}$$

$$m(r,\theta) = m_0(r) + m_2(r)P_2(\cos\theta)\,, \tag{3.6}$$

$$k(r,\theta) = k_0(r) + k_2(r)P_2(\cos\theta)\,, \tag{3.7}$$

where $P_2(cos\theta)$ is the Legendre polynomial of second order. Because the metric does not change under transformations of the type $r \to f(r)$, it is possible to assume $k_0(r) = 0$.

The functions $h = h(r,\theta)$, $m = m(r,\theta)$, $k = k(r,\theta)$ have analytic form in the exterior (vacuum) spacetime and they can be found in Appendix B. The mass, angular momentum, and quadrupole moment are computed from the matching condition between the interior and exterior metrics.

First the angular momentum is computed. It is introduced the angular velocity of the fluid relative to the local inertial frame, $\bar{\omega}(r) = \Omega - \omega(r)$. It can be shown from the Einstein equations at first order in Ω that $\bar{\omega}$ satisfies the differential equation

$$\frac{1}{r^4}\frac{d}{dr}\left(r^4 j \frac{d\bar{\omega}}{dr}\right) + \frac{4}{r}\frac{dj}{dr}\bar{\omega} = 0\,, \tag{3.8}$$

where $j(r) = e^{-(\nu+\lambda)/2}$ with ν and λ the metric functions of the seed non-rotating solution, Eq. (2.2).

From the matching equations, the angular momentum of the star results to be given by

$$J = \frac{1}{6}R^4\left(\frac{d\bar{\omega}}{dr}\right)_{r=R}\,, \tag{3.9}$$

so the angular velocity Ω is related to the angular momentum as

$$\Omega = \bar{\omega}(R) + \frac{2J}{R^3}\,. \tag{3.10}$$

The total mass of the rotating star, M, is given by

$$M = M_0 + \delta M\,, \qquad \delta M = m_0(R) + J^2/R^3\,, \tag{3.11}$$

where δM is the contribution to the mass owing to rotation. The second order functions m_0 and p_0^* (related to the pressure perturbation) are computed from the solution of the differential equation

$$\frac{dm_0}{dr} = 4\pi r^2 \frac{d\mathcal{E}}{dP}(\mathcal{E}+P)p_0^* + \frac{1}{12}j^2 r^4\left(\frac{d\bar{\omega}}{dr}\right)^2 - \frac{1}{3}\frac{dj^2}{dr}r^3\bar{\omega}^2\,, \tag{3.12}$$

$$\begin{aligned}\frac{dp_0^*}{dr} = &-\frac{m_0(1+8\pi r^2 P)}{(r-2M_0)^2} - \frac{4\pi r^2(\mathcal{E}+P)}{(r-2M_0)}p_0^* \\ &+ \frac{1}{12}\frac{j^2 r^4}{(r-2M_0)}\left(\frac{d\bar{\omega}}{dr}\right)^2 + \frac{1}{3}\frac{d}{dr}\left(\frac{r^3 j^2\bar{\omega}^2}{r-2M_0}\right)\,,\end{aligned} \tag{3.13}$$

where $\mathcal{E}$ and P are the total energy-density and pressure.

Turning to the quadrupole moment of the neutron star, it is given by

$$Q = \frac{J^2}{M_0} + \frac{8}{5}\mathcal{K}M_0^3\,, \tag{3.14}$$

where $\mathcal{K}$ is a constant of integration. This constant is fixed from the matching of the second order function h_2 obtained in the interior from

$$\begin{aligned}\frac{dk_2}{dr} =& -\frac{dh_2}{dr} - h_2\frac{d\nu}{dr} + \left(\frac{1}{r} + \frac{1}{2}\frac{d\nu}{dr}\right) \\ & \times \left[-\frac{1}{3}r^3\bar{\omega}^2\frac{dj^2}{dr} + \frac{1}{6}r^4 j^2\left(\frac{d\bar{\omega}}{dr}\right)^2\right], \qquad (3.15)\\ \frac{dh_2}{dr} =& \, h_2\left\{-\frac{d\nu}{dr} + \frac{r}{r-2M_0}\left(\frac{d\nu}{dr}\right)^{-1}\left[8\pi(\mathcal{E}+P) - \frac{4M_0}{r^3}\right]\right\} \\ & - \frac{4(k_2+h_2)}{r(r-2M_0)}\left(\frac{d\nu}{dr}\right)^{-1} \\ & + \frac{1}{6}\left[\frac{r}{2}\frac{d\nu}{dr} - \frac{1}{r-2M_0}\left(\frac{d\nu}{dr}\right)^{-1}\right] r^3 j^2\left(\frac{d\bar{\omega}}{dr}\right)^2 \\ & - \frac{1}{3}\left[\frac{r}{2}\frac{d\nu}{dr} + \frac{1}{r-2M_0}\left(\frac{d\nu}{dr}\right)^{-1}\right] r^2\bar{\omega}^2\frac{dj^2}{dr}, \qquad (3.16)\end{aligned}$$

with its exterior counterpart (see Hartle (1967) and Appendix B).

It is worth to underline that the influence of the induced magnetic field owing to the rotation of the charged core of the neutron star in the globally neutral case is negligible (Boshkayev et al., 2012b). In fact, for a rotating neutron star of period $P = 10$ ms and radius $R \sim 10$ km, the radial component of the magnetic field B_r in the core interior reaches its maximum at the poles with a value $B_r \sim 2.9\times10^{-16}B_c$, where $B_c = m_e^2c^3/(e\hbar) \approx 4.4\times10^{13}$ G is the critical magnetic field for vacuum polarization. The angular component of the magnetic field B_θ, instead, has its maximum value at the equator and, as for the radial component, it is very low in the interior of the neutron star core, i.e. $|B_\theta| \sim 2.9\times10^{-16}B_c$. In the case of a sharp core-crust transition as the one studied by Belvedere et al. (2012) and shown in Fig. 2.1, this component will grow in the transition layer to values of the order of $|B_\theta| \sim 10^2 B_c$ (see Boshkayev et al., 2012b, for further details). However, since we are here interested in the macroscopic properties of the neutron star, we can ignore at first approximation the presence of electromagnetic fields in the macroscopic regions where they are indeed very small, and safely apply the original Hartle formulation without any generalization.

3.3 Stability of Uniformly Rotating Neutron Stars

3.3.1 Secular Axisymmetric Instability

In a sequence of increasing central density in the M-ρ_c curve, $\rho_c \equiv \rho(0)$, the maximum mass of a non-rotating neutron star is defined as the first maximum of such a curve, namely the point where $\partial M/\partial \rho_c = 0$. This derivative defines the secular instability point, and, if the perturbation obeys the same equation of state (EOS) as the equilibrium configuration, it coincides also with the dynamical instability point (see e.g. Shapiro and Teukolsky, 1983). In the rotating case, the situation becomes more complicated and in order to find the axisymmetric dynamical instability points, the perturbed solutions with zero frequency modes (the so-called neutral frequency line) have to be calculated. Friedman et al. (1988) however, following the works of Sorkin (1981, 1982), described a turning-point method to obtain the points at which secular instability is reached by uniformly rotating stars. In a constant angular momentum sequence, the turning point is located in the maximum of the mass-central density relation, namely the onset of secular axisymmetric instability is given by

$$\left[\frac{\partial M\left(\rho_c, J\right)}{\partial \rho_c}\right]_{J=\text{constant}} = 0\,, \tag{3.17}$$

and once the secular instability sets in, the star evolves quasi-stationarily until it reaches a point of dynamical instability where gravitational collapse sets in (Stergioulas, 2003).

The above equation defines an upper limit for the mass at a given J for a uniformly rotating star, however this criterion is a sufficient but not necessary condition for the instability. This means that all the configurations with the given angular momentum J on the right side of the turning point defined by Eq. (3.17) are secularly unstable, but it does not imply that the configurations on the left side of it are stable. An example of dynamically unstable configurations on the left side of the turning-point limiting boundary in neutron stars was recently shown by Takami et al. (2011), for a specific EOS.

3.3.2 Keplerian Mass-Shedding Instability

The maximum velocity for a particle to remain in equilibrium on the equator of a star, kept bound by the balance between gravitational and centrifugal force, is the Keplerian velocity of a free particle computed at the same

location. As shown, for instance in (Stergioulas, 2003), a star rotating at Keplerian rate becomes unstable due to the loss of mass from its surface. The mass shedding limiting angular velocity of a rotating star is the Keplerian angular velocity evaluated at the equator, $r = R_{\rm eq}$, i.e. $\Omega_K^{J\neq 0} = \Omega_K(r = R_{\rm eq})$. Friedman et al. (1986) introduced a method to obtain the maximum possible angular velocity of the star before reaching the mass-shedding limit; however Torok et al. (2008) and Bini et al. (2013), showed a simpler way to compute the Keplerian angular velocity of a rotating star. They showed that the mass-shedding angular velocity, $\Omega_K^{J\neq 0}$, can be computed as the orbital angular velocity of a test particle in the external field of the star and co-rotating with it on its equatorial plane at the distance $r = R_{\rm eq}$. For the Hartle external solution, this is given by

$$\Omega_K^{J\neq 0}(r) = \sqrt{\frac{M}{r^3}}\left[1 - jF_1(r) + j^2F_2(r) + qF_3(r)\right] , \tag{3.18}$$

where $j = J/M^2$ and $q = Q/M^3$ are the dimensionless angular momentum and quadrupole moment. Further details and the analytical expression of the functions F_i can be found in Appendix B.

3.3.3 Gravitational Binding Energy

Besides the above stability requirements, one should check if the neutron star is gravitationally bound. In the non-rotating case, the binding energy of the star can be computed as

$$W_{J=0} = M_0 - M^0_{\rm rest} , \qquad M^0_{\rm rest} = m_b A_{J=0} , \tag{3.19}$$

where $M^0_{\rm rest}$ is the rest-mass of the star, m_b is the rest-mass per baryon, and $A_{J=0}$ is the total number of baryons inside the star. So the non-rotating star is considered bound if $W_{J=0} < 0$.

In the slow rotation approximation the total binding energy is given by (Hartle and Thorne, 1968)

$$W_{J\neq 0} = W_{J=0} + \delta W , \qquad \delta W = \frac{J^2}{R^3} - \int_0^R 4\pi r^2 B(r) dr , \tag{3.20}$$

where

$$
\begin{aligned}
B(r) =&(\mathcal{E}+P)p_0^*\Bigg\{\frac{d\mathcal{E}}{dP}\left[\left(1-\frac{2M}{r}\right)^{-1/2}-1\right] \\
&-\frac{du}{dP}\left(1-\frac{2M}{r}\right)^{-1/2}\Bigg\}(\mathcal{E}-u)\left(1-\frac{2M}{r}\right)^{-3/2} \\
&\times\left[\frac{m_0}{r}+\frac{1}{3}j^2r^2\bar{\omega}^2\right]-\frac{1}{4\pi r^2}\left[\frac{1}{12}j^2r^4\left(\frac{d\bar{\omega}}{dr}\right)^2-\frac{1}{3}\frac{dj^2}{dr}r^3\bar{\omega}^2\right], \quad (3.21)
\end{aligned}
$$

where $u = \mathcal{E} - m_b n_b$ is the internal energy of the star, with n_b the baryon number density.

We will therefore request that the binding energy be negative, namely $W_{J\neq 0} < 0$. As we will show below in Sec. 3.4.2 this condition leads to a minimum mass for the neutron star under which the star becomes gravitationally unbound.

3.4 Structure of Uniformly Rotating Neutron Stars

In this section we show the results of the integration of the Hartle equations for the globally and locally charge neutrality neutron stars; see e.g. Fig. 2.1. Following Belvedere et al. (2012), we adopt, as an example, globally neutral neutron stars with a density at the edge of the crust equal to the neutron drip density, $\rho_{\rm crust} = \rho_{\rm drip} \approx 4.3 \times 10^{11}$ g cm^{-3}.

3.4.1 Secular Instability Boundary

In Fig. 3.1 we show the mass-central density curve for globally neutral neutron stars in the region close to the axisymmetric stability boundaries. Specifically are shown some J-constant sequences to stress that indeed along each of these curves there exist a maximum mass point (turning point). The line joining all the turning points defines the secular instability limit and the axisymmetric stable zone is on the left side of this instability line.

Clearly we can to transform the mass-central density relation in a mass-radius relation. In Fig. 3.2 we shown the mass versus the equatorial radius of the neutron star that correspond to the range of densities of Fig. 3.1. In this plot the stable zone is on the right side of the instability line.

We can construct a fitting curve joining the turning points of the J-constant sequences line which determines the secular axisymmetric instability

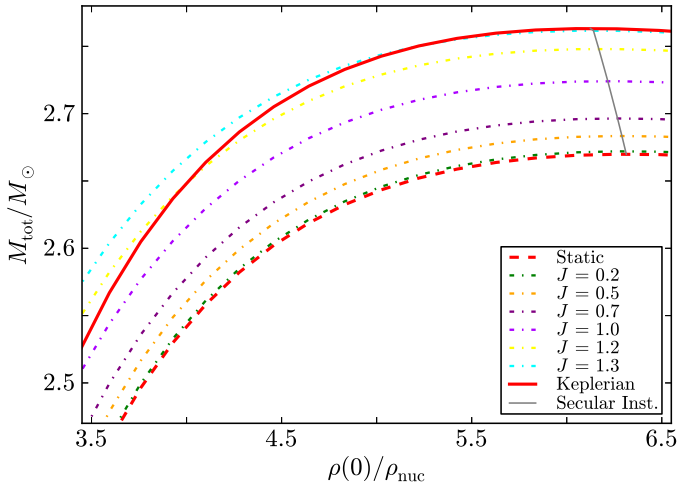

Figure 3.1: Total mass versus central density of globally neutral neutron stars. The solid line represents the configuration with Keplerian angular velocity, the dashed line represents the static configuration, the dotted-dashed lines represent the J-constant sequences (in units of 10^{11} cm^2). The gray line joins all the turning points of the J-constant sequences, so it defines the secular instability boundary.

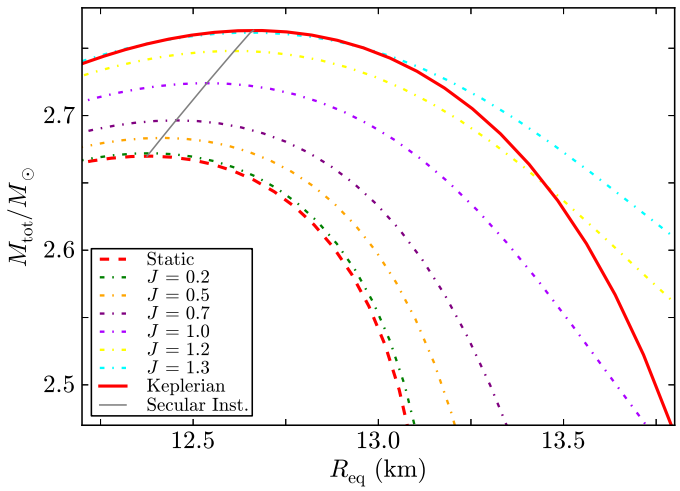

Figure 3.2: Total mass versus equatorial radius of globally neutral neutron stars. The solid line represents the configuration with Keplerian angular velocity, the dashed line represents the static configuration, the dotted-dashed lines represent the J-constant sequences (in units of 10^{11} cm^2). The gray curve joins all the turning points of the J-constant sequences, so it defines the secular instability boundary.

boundary. Defining $M_{\rm max,0}$ as the maximum stable mass of the non-rotating neutron star constructed with the same EOS, we find that for globally neutral configurations the instability line is well fitted by the function

$$\frac{M_{\rm sec}^{\rm GCN}}{M_\odot} = 21.22 - 6.68\frac{M_{\rm max,0}^{\rm GCN}}{M_\odot} - \left(77.42 - 28\frac{M_{\rm max,0}^{\rm GCN}}{M_\odot}\right)\left(\frac{R_{\rm eq}}{10\,{\rm km}}\right)^{-6.08}, \qquad (3.22)$$

where $12.38\,{\rm km} \lesssim R_{\rm eq} \lesssim 12.66\,{\rm km}$, and $M_{\rm max,0}^{\rm GCN} \approx 2.67 M_\odot$.

The turning points of locally neutral configurations in the mass-central density plane are shown in Fig. 3.3. the corresponding mass-equatorial radius plane is plotted in Fig. 3.4.

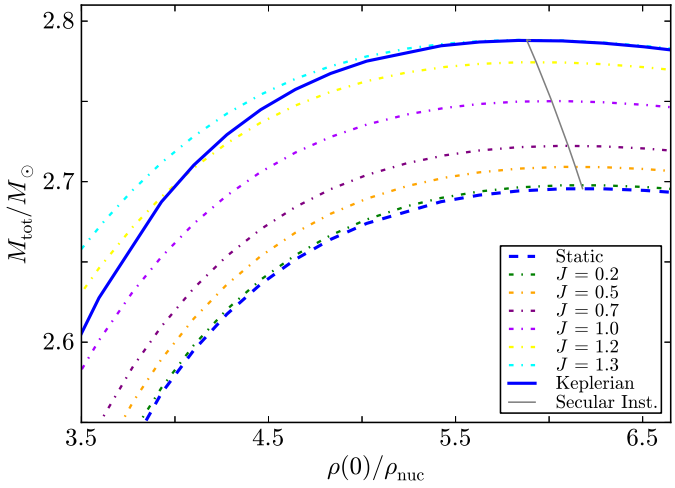

Figure 3.3: Total mass versus central density of locally neutral neutron stars. The solid line represents the configuration with Keplerian angular velocity, the dashed line represents the static configuration, the dotted-dashed lines represent the J-constant sequences (in units of 10^{11} cm^2). The gray line joins all the turning points of the J-constant sequences, so it defines the secular instability boundary.

For locally neutral neutron stars, the secular instability line is fitted by

$$\frac{M_{\rm sec}^{\rm LCN}}{M_\odot} = 20.51 - 6.35\frac{M_{\rm max,0}^{\rm LCN}}{M_\odot} - \left(80.98 - 29.02\frac{M_{\rm max,0}^{\rm LCN}}{M_\odot}\right)\left(\frac{R_{\rm eq}}{10\,{\rm km}}\right)^{-5.71}, \qquad (3.23)$$

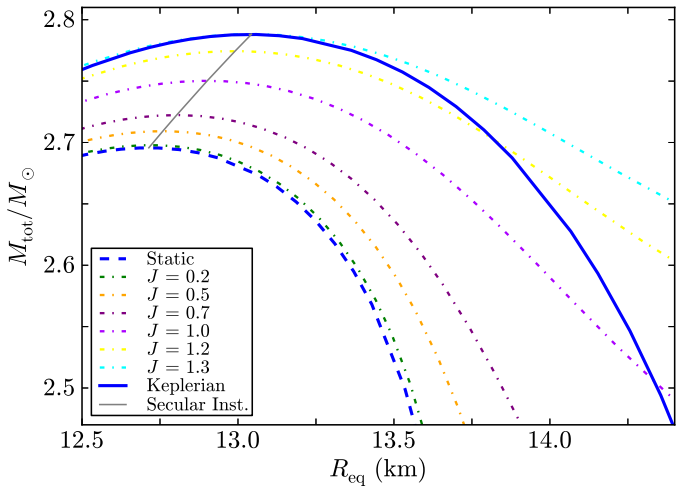

Figure 3.4: Total mass versus equatorial radius of locally neutral neutron stars. The solid line represents the configuration with Keplerian angular velocity, the dashed line represents the static configuration, the dotted-dashed lines represent the J-constant sequences (in units of 10^{11} cm^2). The gray curve joins all the turning points of the J-constant sequences, so it defines the secular instability boundary.

where $12.71\,\mathrm{km} \lesssim R_{\rm eq} \lesssim 13.06\,\mathrm{km}$, and $M^{\rm LCN}_{\rm max,0} \approx 2.70 M_\odot$.

3.4.2 Keplerian Mass-Shedding Sequence

We turn now to analyze in detail the behavior of the different properties of the neutron star along the Keplerian mass-shedding sequence. For the sake of reference we have indicated in the following plots stars with the selected masses $M \approx [1, 1.4, 2.04, 2.5]\, M_\odot$. The cyan star indicates the fastest observed pulsar, PSR J1748–2446ad (Hessels et al., 2006), with a rotation frequency of $f \approx 716$ Hz. The gray filled circles indicate the last stable configuration of the Keplerian sequence, namely the point where the Keplerian and the secular stability boundaries cross each other.

Maximum Mass and Rotation Frequency

The total mass of the rotating star is computed from Eq. (3.11). In Fig. 3.5 is shown the total mass of the neutron star as a function of the rotation frequency for the Keplerian sequence. It is clear that for a given mass, the rotational frequency is higher for a globally neutral neutron star with respect to the locally neutral one.

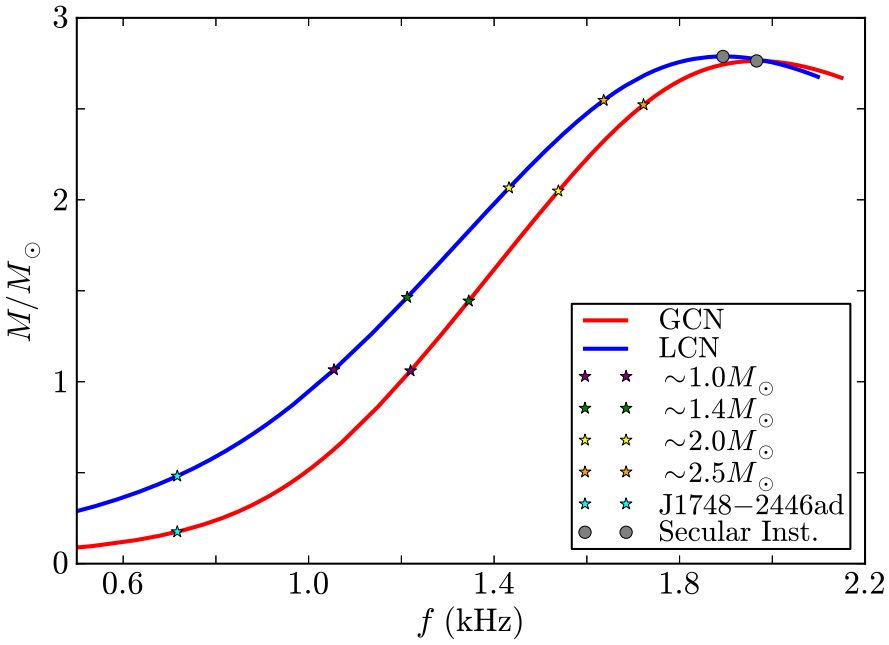

Figure 3.5: Total mass versus rotational Keplerian frequency both for the global (red) and local (blue) charge neutrality cases.

The configuration of maximum mass, $M_{\rm max}^{J\neq 0}$, occurs along the Keplerian sequence, and it is found before the secular instability line crosses the Keplerian curve. Thus, the maximum mass configuration is secularly stable. This implies that the configuration with maximum rotation frequency, $f_{\rm max}$, is located beyond the maximum mass point, specifically at the crossing point between the secular instability and the Keplerian mass-shedding sequence. The results are summarized in Table 3.1.

It is important to discuss briefly the validity of the present perturbative solution for the computation of the properties of maximally rotating neutron stars. The expansion of the radial coordinate of a rotating configuration $r(R,\theta)$ in powers of angular velocity is written as (Hartle, 1967)

$$r = R + \xi(R,\theta) + O(\Omega^4)\,, \tag{3.24}$$

where ξ is the difference in the radial coordinate, r, between a point located at the polar angle θ on the surface of constant density $\rho(R)$ in the rotating configuration, and the point located at the same polar angle on the same constant density surface in the non-rotating configuration.

In the slow rotation regime, the fractional displacement of the surfaces of constant density due to the rotation have to be small, namely $\xi(R,\theta)/R \ll 1$,

	Global Neutrality	Local Neutrality
$M_{\rm max}^{J=0}$ $(M_\odot)$	2.67	2.70
$R_{\rm max}^{J=0}$ (km)	12.38	12.71
$M_{\rm max}^{J\neq0}$ $(M_\odot)$	2.76	2.79
$R_{\rm max}^{J\neq0}$ (km)	12.66	13.06
$\delta M_{\rm max}$	3.37%	3.33%
$\delta R_{\rm eq}^{\rm max}$	2.26%	2.75%
$f_{\rm max}$ (kHz)	1.97	1.89
$P_{\rm min}$ (ms)	0.51	0.53

Table 3.1: $M_{\rm max}^{J=0}$ and $R_{\rm max}^{J=0}$: maximum mass and corresponding radius of non-rotating stars as computed in (Belvedere et al., 2012); $M_{\rm max}^{J=0}$ and $R_{\rm max}^{J=0}$: maximum mass and corresponding radius of rotating stars; $\delta M_{\rm max}$ and $\delta R_{\rm eq}^{\rm max}$: increase in mass and radius of the maximum mass configuration with respect to its non-rotating counterpart; $f_{\rm max}$ and $P_{\rm min}$: maximum rotation frequency and associated minimum period.

where $\xi(R,\theta) = \xi_0(R) + \xi_2(R)P_2(\cos\theta)$ and $\xi_0(R)$ and $\xi_2(R)$ are function of R, proportional to Ω^2. From Table 3.1, we can see that the configuration with the maximum possible rotation frequency has a maximum fractional displacement $\delta R_{\rm eq}^{\rm max} = \xi(R,\pi/2)/R$ as low as $\approx 2\%$ and $\approx 3\%$, for the globally and locally neutral neutron stars respectively.

In this line, it is worth to quote the results of Benhar et al. (2005), who showed that the inclusion of a third-order expansion Ω^3 in the Hartle's method improves the value of the maximum rotation frequency by less than 1% for different EOS. The reason for this is that as mentioned above, along the Keplerian sequence the deviations from sphericity decrease with density and frequency (see Figs. 3.14 and 3.15), which ensures the accuracy of the perturbative solution.

Turning to the increase of the maximum mass, Weber and Glendenning (1992) showed that the mass of maximally rotating neutron stars, computed with the Hartle's second order approximation, is accurate within an error as low as $\lesssim 4\%$.

Minimum Mass and Rotation Frequency

We compute now the gravitational binding energy of the neutron star from Eq. (3.20) as a function of the central density and angular velocity. We make this for central densities higher than the nuclear density, thus we impose the neutron star to have a supranuclear hadronic core. In Fig. 3.6 we

plot the binding energy W of the neutron star as a function of the neutron star mass along the Keplerian sequence. For the sake of comparison we show also the binding energy of the non-rotating configurations.

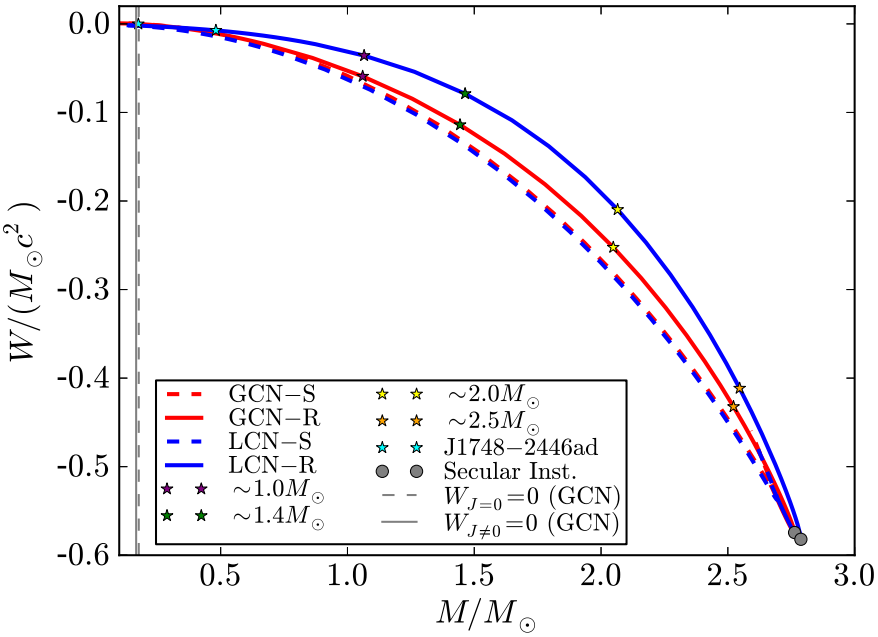

Figure 3.6: Neutron star binding energy versus total mass along the Keplerian sequence both for the global (red) and local (blue) charge neutrality.

We found that the globally neutral neutron stars studied here are bound up to some minimum mass at which the gravitational binding energy vanishes. For the static and Keplerian configurations we find that $W_{J=0} = 0$, and $W_{J\neq 0} = 0$ respectively at

$$M^{J=0}_{\rm min} \approx 0.177\, M_\odot\,, \qquad M^{K}_{\rm min} \approx 0.167\, M_\odot\,, \tag{3.25}$$

where with the superscript K we indicate that this value corresponds to the minimum mass on the Keplerian sequence. Clearly this minimum mass value decreases with decreasing frequency until it reaches the above value $M^{J=0}_{\rm min}$ of the non-rotating case.

We did not find any unbound configuration in the local charge neutrality case for the present EOS (see Fig. 3.6). The corresponding plot of W as a function of the central density is shown in Fig. 3.7.

The configuration with the minimum mass, $M^{K}_{\rm min} \approx 0.167\, M_\odot$, has a rotation frequency

$$f^{K}_{\rm min} = f(M^{K}_{\rm min}) \approx 700.59\,{\rm Hz}\,, \tag{3.26}$$

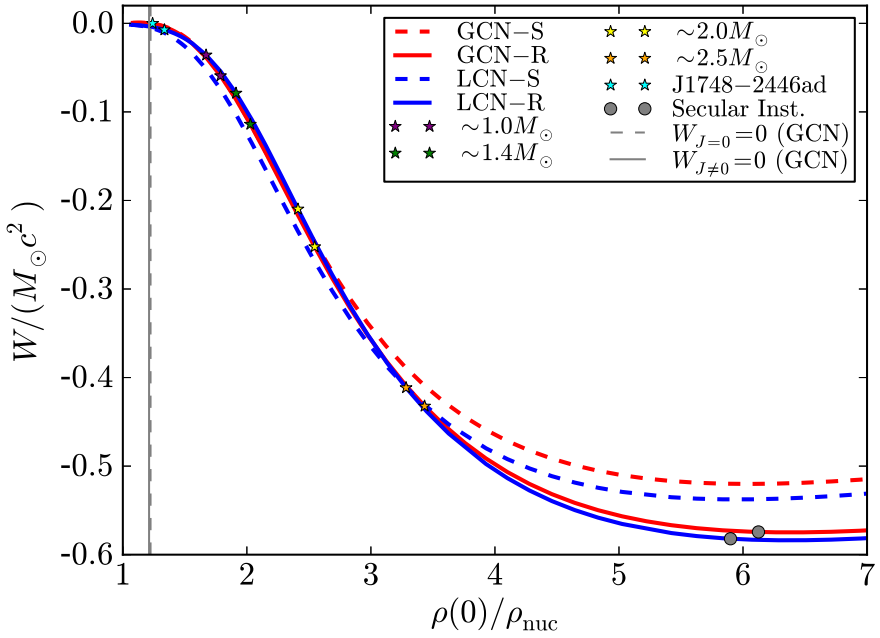

Figure 3.7: Neutron star binding energy versus central density along the Keplerian sequence both for the global (red) and local (blue) charge neutrality.

that is the minimum rotation rate that globally neutral configurations can have along the Keplerian sequence in order to be gravitationally bound. Interestingly, the above value is slightly lower than the frequency of the fastest observed pulsar, PSR J1748–2446ad, which has a frequency of 716 Hz (Hessels et al., 2006). Further discussions on this issue are given below in Sec. 3.8.

In Fig. 3.8 we show in detail the dependence of W on the rotation frequency.

3.5 Neutron Star Mass-Radius Relation

In this section are summarized the above results in form of a new mass-radius relation of uniformly rotating neutron stars, including the Keplerian and secular instability boundary limits. In Fig. 3.9 we show a summary plot of the equilibrium configurations of rotating neutron stars. In particular we show the total mass versus the equatorial radius: the dashed lines represent the static (non-rotating, $J = 0$) sequences, while the solid lines represent the corresponding Keplerian mass-shedding sequences. The secular instability boundaries are plotted in pink-red and light blue color for the global and local charge neutrality cases, respectively.

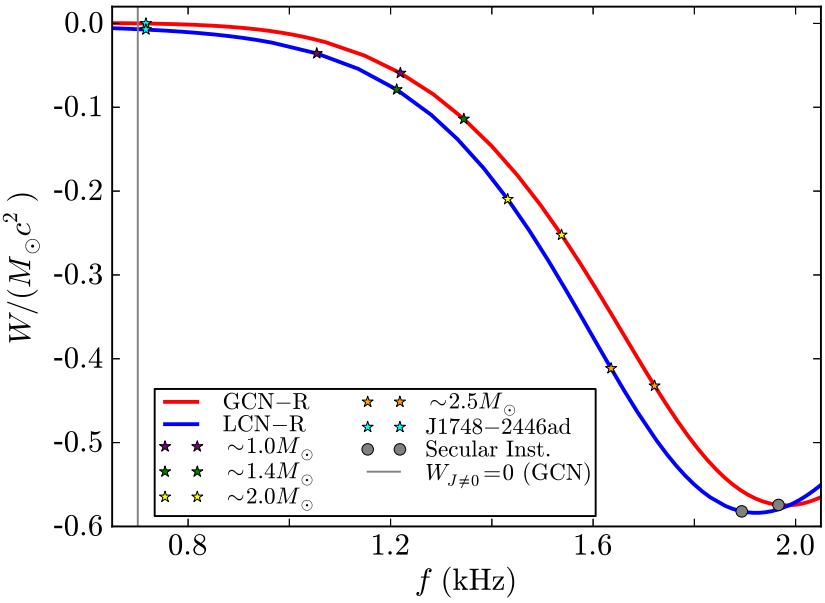

Figure 3.8: Neutron star binding energy versus frequency for the Keplerian sequence both for the global (red) and local (blue) charge neutrality neutron stars.

It can be seen that due to the deformation for a given mass the radius of the rotating case is larger than the static one, and similarly the mass of the rotating star is larger than the corresponding static one. It can be also seen that the configurations obeying global charge neutrality are more compact with respect to the ones satisfying local charge neutrality.

3.6 Moment of Inertia

The neutron star moment of inertia I can be computed from the relation

$$I = \frac{J}{\Omega}\,, \tag{3.27}$$

where J is the angular momentum and Ω are related via Eq. (3.10). Since J is a first-order quantity and so proportional to Ω, the moment of inertia given by Eq. (3.27) does not depend on the angular velocity and does not take into account deviations from the spherical symmetry. This implies that Eq. (3.9) gives the moment of inertia of the non-rotating unperturbed seed object. In order to find the perturbation to I, say δI, the perturbative treatment has to be extended to the next order Ω^3, in such a way that

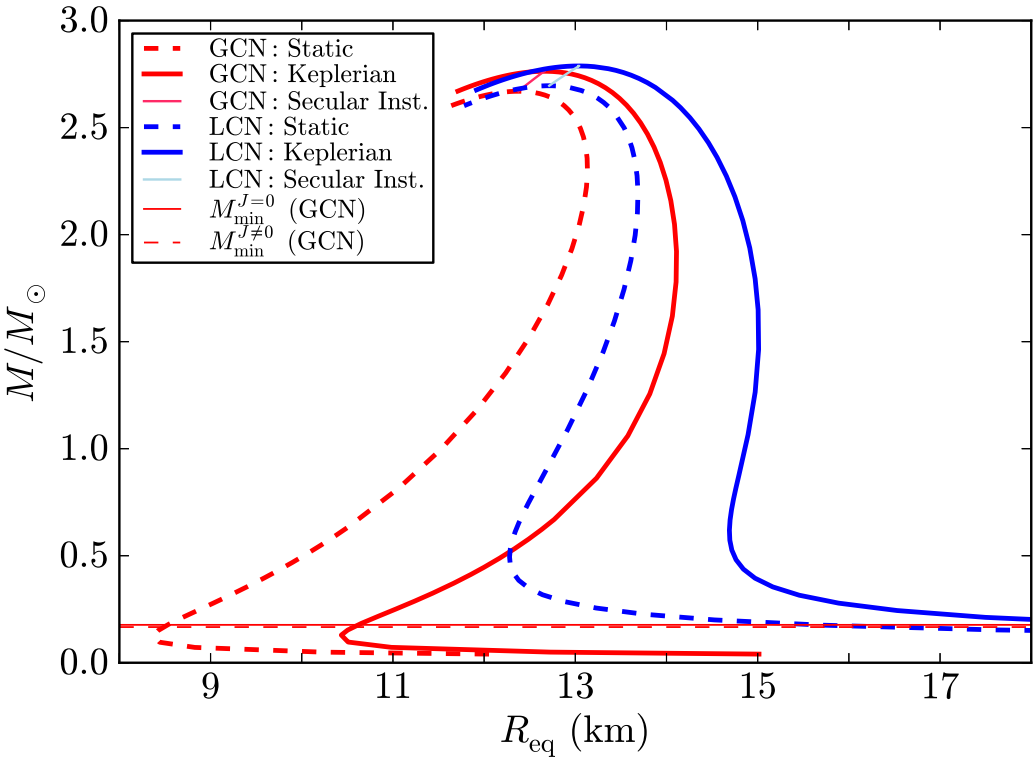

Figure 3.9: Total mass versus total equatorial radius for the global (red) and local (blue) charge neutrality cases. The dashed curves represent the static configurations, while the solid lines are the uniformly rotating neutron stars. The pink-red and light-blue color lines define the secular instability boundary for the globally and locally neutral cases, namely the lines given by Eqs. (3.22) and (3.23), respectively.

$I = I_0 + \delta I = (J_0 + \delta J)/\Omega$, becomes of order Ω^2, with δJ of order Ω^3 (see e.g. Hartle, 1973; Benhar et al., 2005). In this work we keep the solution up to second order and therefore the moment of inertia is the one for the non-rotating configurations. In any case, as seen in Sec. 3.4 even the fastest observed pulsars rotate at frequencies much lower than the Keplerian rate, and under such conditions we expect that the moment of inertia can be approximated with high accuracy by the one of the corresponding static configurations. Moreover, owing to the high density of neutron stars, most of the observed pulsars are accurately described by a perturbed spherical geometry and the accuracy of the moment of inertia of the non-rotating star is a good approximation for the actual value of the rotating object. The accuracy of the approximation increases for stiffer EOS (see Benhar et al., 2005, for details), as it is the case of the EOS obtained from σ-ω-ρ relativistic nuclear mean field models (Boguta and Bodmer, 1977) such as the one used here.

In Figs. 3.10 and 3.11 we show the behavior of the total momentum of inertia, i.e. $I = I_{\rm core} + I_{\rm crust}$, with respect to the total mass and central density for both globally and locally neutral non-rotating neutron stars.

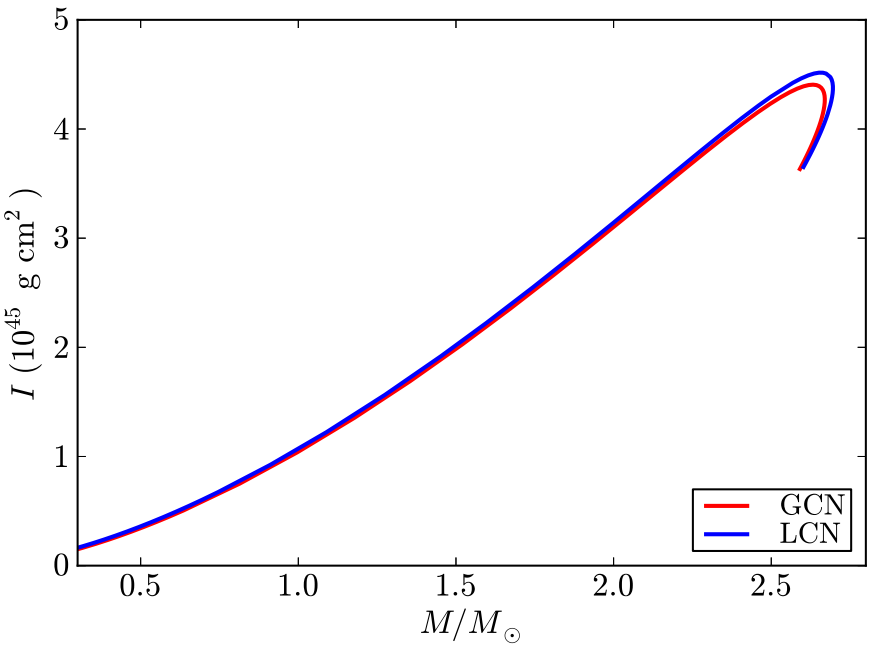

Figure 3.10: Total moment of inertia versus total mass both for globally (red) and locally (blue) neutral non-rotating neutron stars.

We can see from Figs. 3.10 and 3.11 that the total moment of inertia is

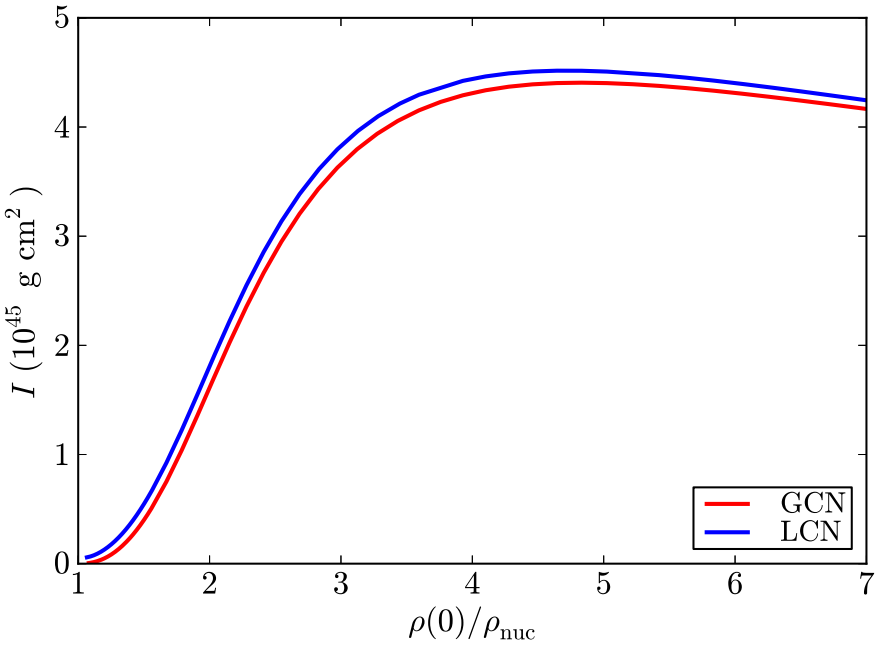

Figure 3.11: Total moment of inertia versus central density for globally (red) and locally (blue) neutral non-rotating neutron stars.

quite similar for both global and local charge neutrality cases. This is due to the fact that the globally neutral configurations differ from the locally ones mostly in the structure of the crust, which however contributes much less than the neutron star core to the total moment of inertia (see below in section 3.6.1).

3.6.1 Core and Crust Moment of Inertia

In order to study the single contribution of the core and the crust to the moment of inertia of the neutron star, it shall to be used the integral expression for the moment of inertia. Multiplying Eq. (3.8) by r^3 and making the integral of it, the following relation we obtain[1]

$$I(r) = -\frac{2}{3}\int_0^r r^3 \frac{dj}{dr}\frac{\bar{\omega}(r)}{\Omega}dr = \frac{8\pi}{3}\int_0^r r^4(\mathcal{E}+P)e^{(\lambda-\nu)/2}\frac{\bar{\omega}(r)}{\Omega}dr\,, \qquad (3.28)$$

where the integration is carried out in the region of interest. Thus, the contribution of the core, I_{core}, is obtained integrating from the origin up to

[1]It is clear that this expression approaches, in the weak field limit, the classic Newtonian expression $I_{\mathrm{Newtonian}} = (8\pi/3)\int r^4\rho\, dr$ where ρ is the mass-density (Hartle, 1967).

the radius of the core, and the contribution of the crust, $I_{\rm crust}$, integrating from the base of the crust to the total radius of the neutron star.

We show in Figs. 3.12 and 3.13 the ratio between the moment of inertia of the crust and the one of the core as a function of the total mass and central density, respectively, for both the globally and locally neutral configurations.

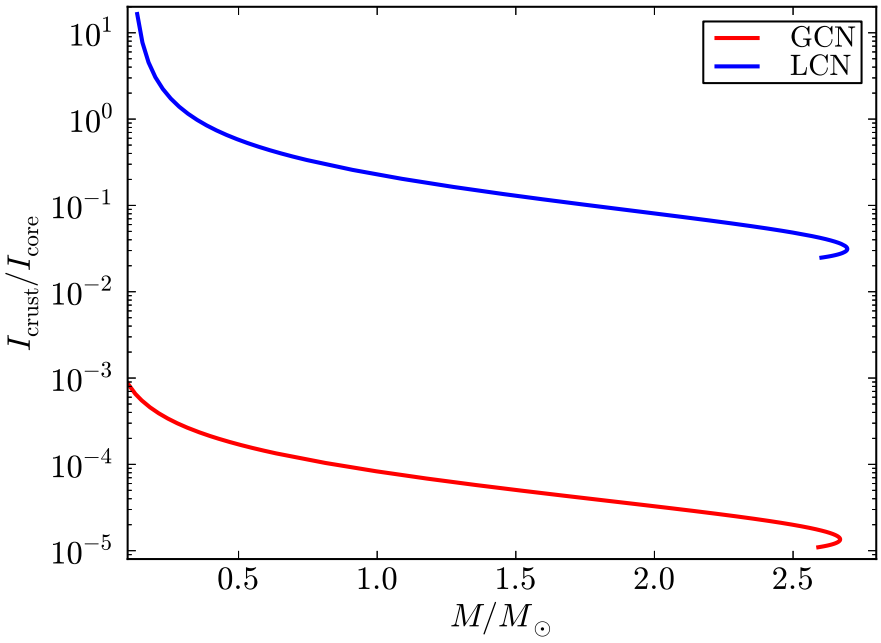

Figure 3.12: Crust to core moment of inertia ratio versus the total mass of both globally and locally neutral non-rotating neutron stars.

3.7 Deformation of the Neutron Star

In this section we explore the deformation properties of the neutron star. The behavior of the eccentricity, the rotational to gravitational energy ratio, as well as the quadrupole moment, are investigated as a function of the mass, density, and rotation frequency of the neutron star.

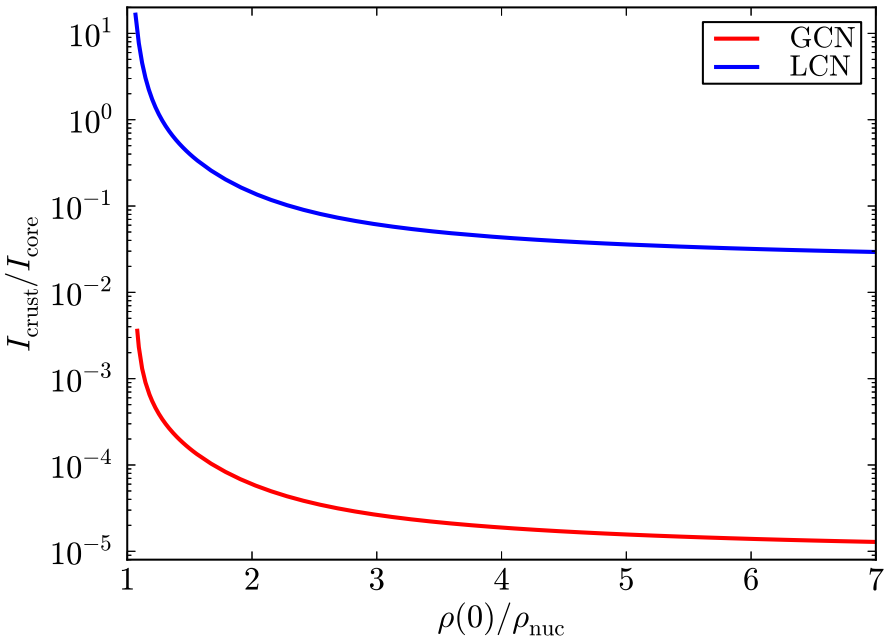

Figure 3.13: Crust to core moment of inertia ratio versus the central density both globally and locally neutral non-rotating neutron stars.

3.7.1 Eccentricity

A measurement of the level of deformation of the neutron star can be estimated with the eccentricity

$$\epsilon = \sqrt{1 - \left(\frac{R_p}{R_{\rm eq}}\right)^2}\,, \tag{3.29}$$

where R_p and $R_{\rm eq}$ are the polar and equatorial radii of the configuration. Thus, $\epsilon = 0$ defines the spherical limit and $0 < \epsilon < 1$ corresponds to oblate configurations.

In Fig. 3.14, we show the behavior of the total eccentricity (3.29), as a function of the neutron star frequency.

We can see that in general the globally neutral neutron star has an eccentricity larger than the one of the locally neutral configuration for almost the entire range of frequencies and the corresponding central densities, except for the low frequencies $f \lesssim 0.8$ kHz and central densities $\rho(0) \lesssim 1.3\rho_{\rm nuc}$; see also Fig. 3.15. Starting from low values of the frequency f and central density $\rho(0)$, the neutron stars increase their oblateness, and after reaching the maximum value of the eccentricity, the compactness increases and the configurations tend to a more spherical shape.

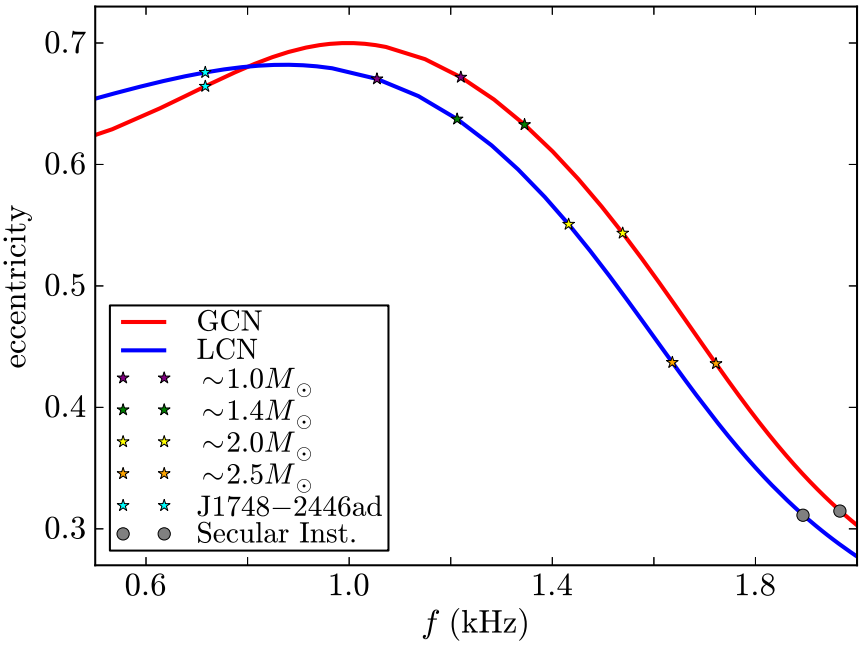

Figure 3.14: Eccentricity (3.29) versus frequency for the Keplerian sequence both for the global (red) and local (blue) charge neutrality cases.

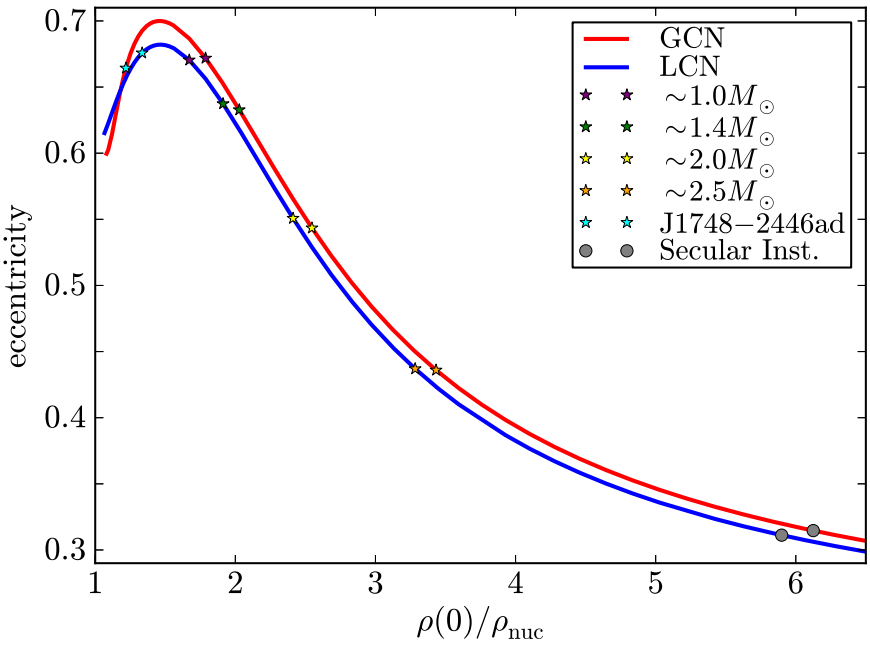

Figure 3.15: Eccentricity (3.29) versus central density for the Keplerian sequence both for the global (red) and local (blue) charge neutrality cases.

3.7.2 Rotational to Gravitational Energy Ratio

Other property of the star related to the centrifugal deformation of the star is the ratio between the gravitational energy and the rotational energy of the star. The former is given by Eq. (3.20), whereas the latter is

$$T = \frac{1}{2} I \Omega^2 \,, \tag{3.30}$$

We show in Fig. 3.16 the ratio $T/|W|$ as a function of the mass of the neutron stars along the Keplerian sequence. In Fig. 3.17 instead we plot the dependence of the ratio on the central density and in Fig. 3.18 on the Keplerian frequency.

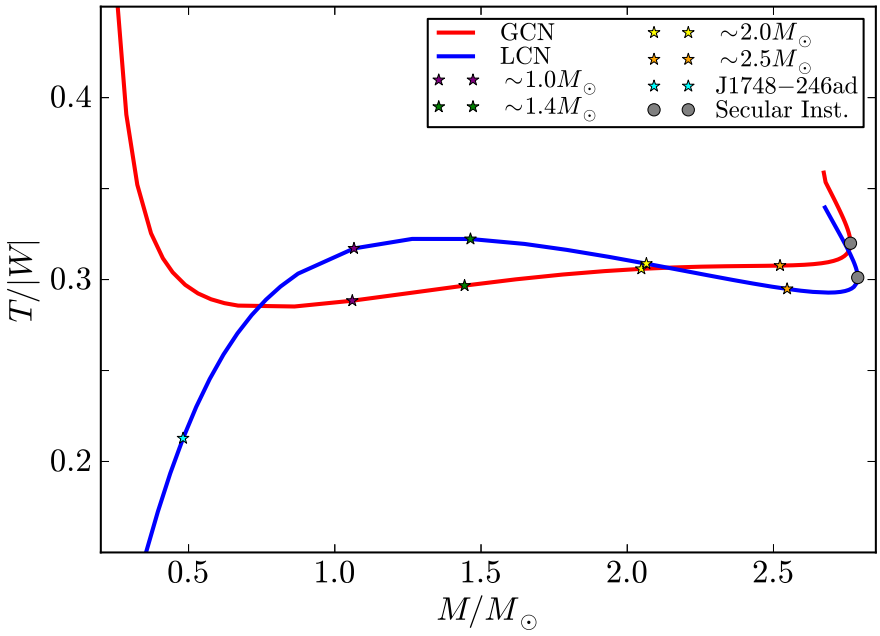

Figure 3.16: Rotational to gravitational binding energy ratio versus total mass along the Keplerian sequence both for the global (red) and local (blue) charge neutrality.

3.7.3 Quadrupole Moment

In Figs. 3.19 and 3.20 we show the quadrupole moment, Q given by Eq. (3.14), as a function of the total mass and central density for both globally and locally neutral neutron stars along the Keplerian sequence. The dependence of Q on the rotation frequency is shown in Fig. 3.21. Here,

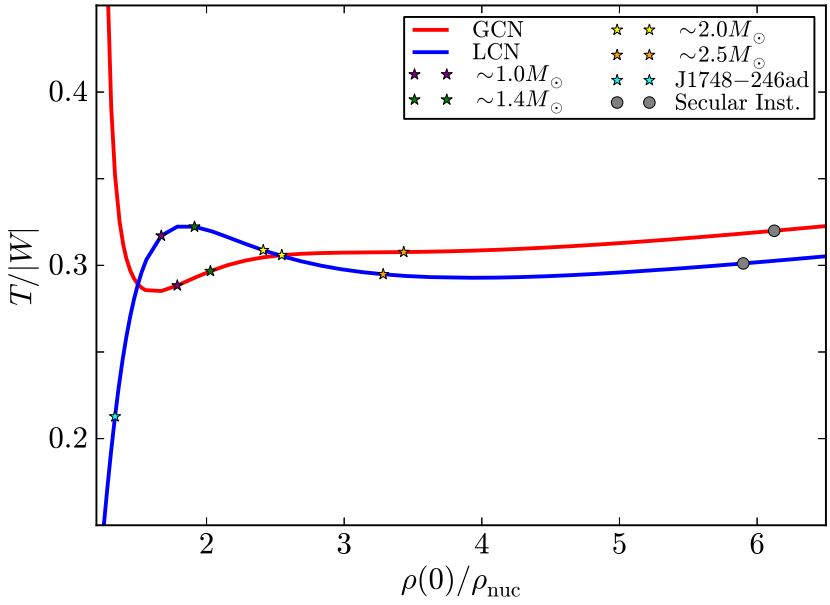

Figure 3.17: Rotational to gravitational binding energy ratio versus central density along the Keplerian sequence both for the global (red) and local (blue) charge neutrality.

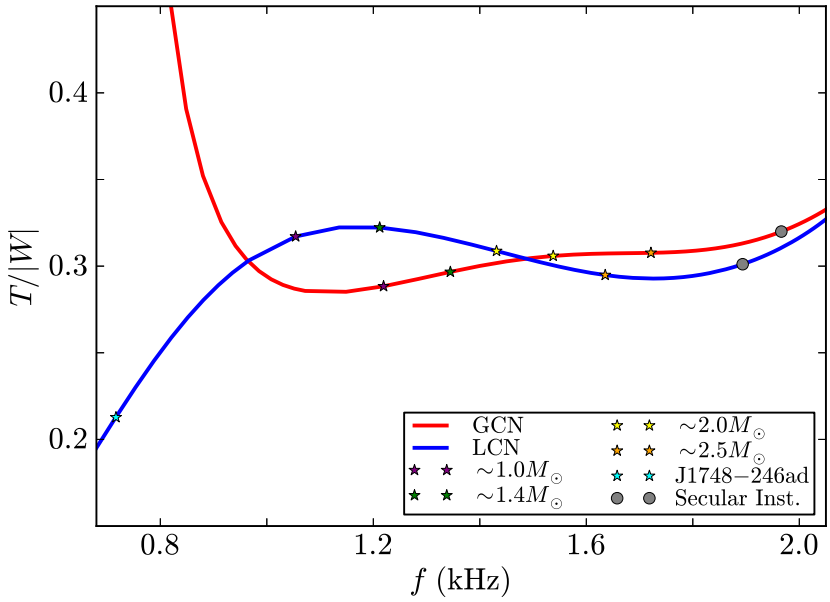

Figure 3.18: Rotational to gravitational binding energy ratio versus frequency along the Keplerian sequence both for the global (red) and local (blue) charge neutrality cases.

we have normalized the quadrupole moment Q to the quantity MR^2 of the non-rotating configuration with the same central density.

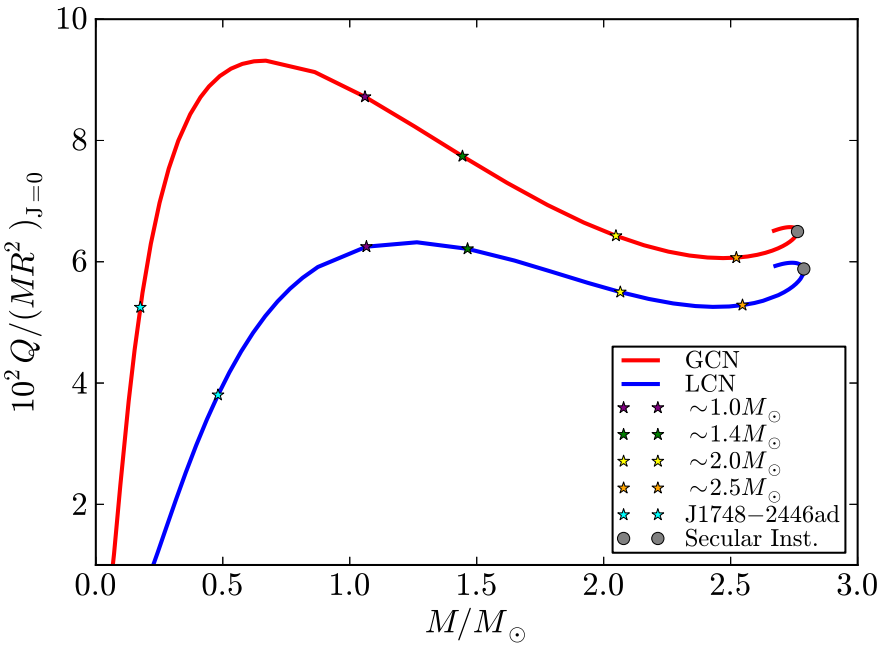

Figure 3.19: Total quadrupole moment versus total mass along the Keplerian sequence both for the global (red) and local (blue) charge neutrality cases. The quadrupole moment Q is here in units of the quantity MR^2 of the non-rotating configuration with the same central density.

3.8 Observational Constraints

In Fig. 3.22 we show the above mass-radius relations together with the most recent and stringent constraints indicated by Trümper (2011a):

1) ***The largest mass***

Until 2013 it was given by the mass of the 3.15 millisecond pulsar PSR J1614–2230 $M = (1.97 \pm 0.04) M_\odot$ (Demorest et al., 2010), however the recent reported mass $(2.01 \pm 0.04) M_\odot$ for the neutron star in the relativistic binary PSR J0348+0432 (Antoniadis et al., 2013) puts an even more stringent request to the nuclear EOS. Thus, the maximum mass of the neutron star has to be larger than the mass of PSR J0348+0432, this constraint is represented by the orange-color stars in Fig. 3.22.

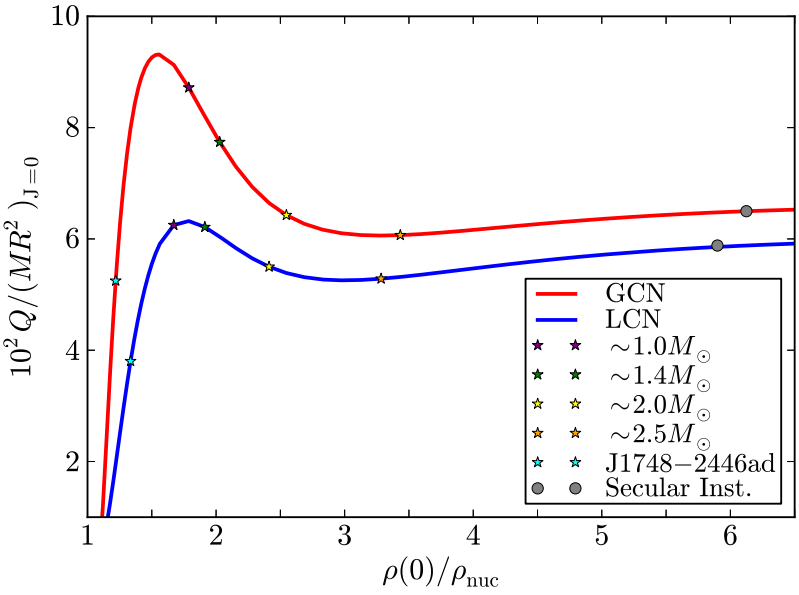

Figure 3.20: Total quadrupole moment versus central density along the Keplerian sequence both for the global (red) and local (blue) charge neutrality cases. The quadrupole moment Q is here in units of the quantity MR^2 of the non-rotating configuration with the same central density.

2) ***The largest radius***

It is given by the lower limit to the radius of RX J1856–3754. The lower limit to the radius as seen by an observer at infinity is $R_\infty = R[1 - 2GM/(c^2R)]^{-1/2} > 16.8$ km, as given by the fit of the optical and X-ray spectra of the source (Trümper et al., 2004); so in the mass-radius relation this constraint reads $2GM/c^2 > R - R^3/(R_\infty^{\rm min})^2$, with $R_\infty^{\rm min} = 16.8$ km. This constraint is represented by the dotted-dashed curve in Fig. 3.22.

3) ***The maximum surface gravity***

Using a neutron star of $M = 1.4 M_\odot$ to fit the Chandra data of the low-mass X-ray binary X7, it turns out that the radius of the star satisfies at 90% confidence level, $R = 14.5^{+1.8}_{-1.6}$ km, which gives $R_\infty = [15.64, 18.86]$ km, respectively (Heinke et al., 2006). Using the same formula as before, $2GM/c^2 > R - R^3/(R_\infty^{\rm min})^2$, we obtain the dotted curves shown in Fig. 3.22.

4) ***The highest rotation frequency***

The fastest observed pulsar is PSR J1748–2446ad with a frequency of 716 Hz (Hessels et al., 2006). It is shown the constant rotation

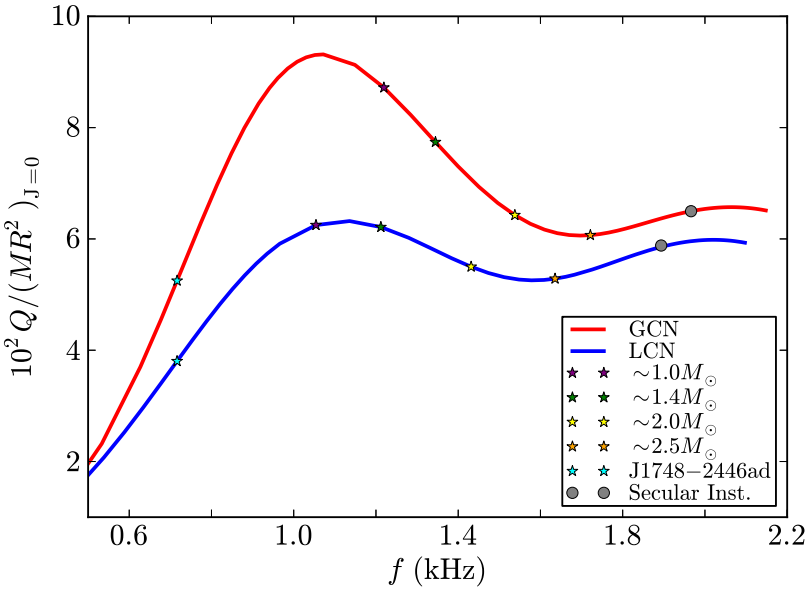

Figure 3.21: Total quadrupole moment versus frequency along the Keplerian sequence both for the global (red) and local (blue) charge neutrality cases. The quadrupole moment Q is here in units of the quantity MR^2 of the non-rotating configuration with the same central density.

frequency sequence $f = 716$ Hz for both globally (dashed pink) and locally (dashed light blue) neutral neutron stars. We indicated with cyan-color stars the point where these curves cross the corresponding Keplerian sequences in the two cases (see Fig. 3.22).

Every f-constant sequence crosses the stability region of the objects in two points: these crossing points define the minimum and maximum possible mass that an object rotating with such a frequency may have in order to be stable. In the case of PSR J1748–2446ad, the cut of the $f = 716$ Hz constant sequence with the Keplerian curve establishes the minimum mass of this pulsar. We find that its minimum mass is $\approx 0.175\,M_\odot$ and corresponding equatorial radius 10.61 km for the globally neutral neutron star. For the locally neutral configuration we find $\approx 0.48\,M_\odot$ and 14.8 km, respectively for the minimum mass and corresponding equatorial radius. This implies that the mass of PSR J1748–2446ad is poorly constrained to be larger than the above values.

It is interesting that the above minimum mass, given by its constant rotation frequency sequence, is slightly larger than the minimum mass for bound configurations on the Keplerian sequence, $M^K_{\rm min} \approx 0.167\,M_\odot$; see Eq. (3.25). In fact, as we shown in Eq. (3.26) the minimum rotation frequency along the

Keplerian sequence for bound configurations in the globally neutral case is, $f^K_{\rm min} \approx 700.59$ Hz, which is slightly lower than the frequency of PSR J1748–2446ad. It would imply that PSR J1748–2446ad is very likely rotating at a rate much lower than the Keplerian one.

Similarly to what presented by Belvedere et al. (2012) for the static neutron stars and introduced by Trümper (2011a), the above observational constraints show a preference on stiff EOS that provide highest maximum masses for neutron stars. It is evident from Fig. 3.22 that mass-radius relations for both the static and the rotating case presented here, are consistent with all the observational constraints. In Table 3.2 we show the radii predicted by our mass-radius relation both for the static and the rotating case for a canonical neutron star as well as for the most massive neutron stars discovered, namely, the millisecond pulsar PSR J1614–2230 (Demorest et al., 2010), $M = (1.97 \pm 0.04) M_\odot$, and the most recent PSR J0348+0432, $M = (2.01 \pm 0.04) M_\odot$ (Antoniadis et al., 2013).

$M(M_\odot)$	$R^{J=0}$ (km)	$R^{J\neq 0}_{\rm eq}$ (km)
1.40	12.313	13.943
1.97	12.991	14.104
2.01	13.020	14.097

Table 3.2: Radii for a canonical neutron star of $M = 1.4 M_\odot$ and for PSR J1614–2230 Demorest et al. (2010), $M = (1.97 \pm 0.04) M_\odot$, and PSR J0348+0432 (Antoniadis et al., 2013), $M = (2.01 \pm 0.04) M_\odot$. These configurations are computed under the constraint of global charge neutrality and for a density at the edge of the crust equal to the neutron drip density. The nuclear parameterizations NL3 has been used.

3.9 Conclusions

We have constructed equilibrium configurations of uniformly rotating neutron stars in both the global charge neutrality and local charge neutrality cases, generalizing our previous work (Belvedere et al., 2012) and described in chapter 2. To do this we have applied the Hartle method to the seed static solution obtained from the integration of the Einstein-Maxwell-Thomas-Fermi equations (Belvedere et al., 2012). We calculated the mass, polar and equatorial radii, angular momentum, moment of inertia, quadrupole moment, and eccentricity, as functions of the central density and the rotation angular velocity of the neutron star.

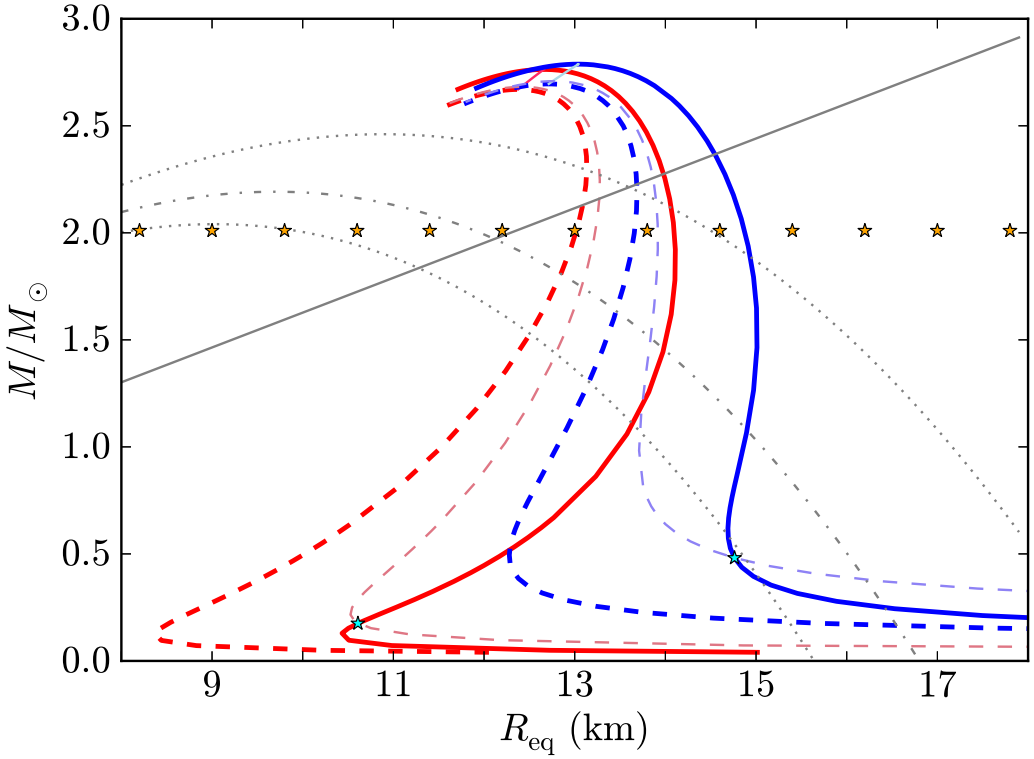

Figure 3.22: Observational constraints on the mass-radius relation given by Trümper (2011a) and the theoretical mass-radius relation presented in this work in Fig. 3.9. The red lines represent the configuration with global charge neutrality, while the blue lines represent the configuration with local charge neutrality. The pink-red line and the light-blue line represent the secular axisymmetric stability boundaries for the globally neutral and the locally neutral case, respectively. The red and blue solid lines represent the Keplerian sequences and the red and blue dashed lines represent the static cases presented by Belvedere et al. (2012).

The Keplerian mass-shedding limit and the secular axisymmetric instability have been analyzed for the construction of the region of stability of rotating neutron stars. We have given fitting curves of the secular instability boundary in Eqs. (3.22) and (3.23) for global and local charge neutrality, respectively. With this analysis we have established in section 3.4.2 the maximum mass and maximum rotation frequency of the neutron star. We computed in section 3.4.2 the gravitational binding energy of the configurations as a function of the central density and rotation rate. We did this for central densities higher than the nuclear one, so imposing that the neutron star has a supranuclear hadronic core. We found that, in the case of a globally neutral neutron star, there is a minimum mass under which the neutron star becomes gravitationally unbound. Along the Keplerian sequence, to this minimum mass object we associate a minimum frequency under which an object rotating at the Keplerian rate becomes unbound; see Eq. (3.26). We found that locally neutral neutron stars with supranuclear cores remained always bound for the present EOS. In Table 3.3 are summarized all these results.

	Global Neutrality	Local Neutrality
$M_{\rm max}^{J=0}(M_\odot)$	2.67	2.70
$M_{\rm max}^{J\neq 0}(M_\odot)$	2.76	2.79
$f_{\rm max}$ (kHz)	1.97	1.89
$P_{\rm min}$ (ms)	0.51	0.53
$M_{\rm min}^{J=0}(M_\odot)$	0.18	–
$M_{\rm min}^{K}(M_\odot)$	0.17	–
$f_{\rm min}^{K}$ (kHz)	0.70	–

Table 3.3: Maximum mass, maximum frequency, minimum period, minimum mass of globally and locally neutral neutron stars.

We finally analyzed in section 3.8 the current observational constraints on the mass-radius relation of neutron stars. We constructed the constant frequency sequence of PSR J1748–2446ad to obtain the minimum possible mass of this source, which is given by the crossing point of the $f = 716$ Hz constant sequence with the Keplerian one. It gives $\approx 0.17\, M_\odot$ and $\approx 0.48\, M_\odot$ for the global and charge neutrality cases, respectively. The very low mass inferred for PSR J1748–2446ad assuming that it rotates at the Keplerian rate implies that its frequency is unlikely to be actually the Keplerian. Otherwise, it would imply that PSR J1748–32446ad could be the less massive neutron star ever observed.

It would be interesting to analyze the generality of the neutron star fea-

tures shown in this work since the most recent measurement of the mass PSR J0348+0432, $M = (2.01 \pm 0.04)M_{\odot}$ (Antoniadis et al., 2013), favors stiff nuclear EOS as the one used here.

3.10 Perspectives

Regarding the topic faced in this chapter, here we could make similar considerations as for the first one. Namely, it would be interesting to study the changes in the configuration of the neutron stars for different nuclear models. In addition to a different nuclear model, it should be studied the configurations with $\rho_{\rm drip} < \rho_{\rm crust}$, as well as the cooling of the rotating neutron stars and the axisymmetric oscillations.

Moreover, once rotation is taken into account, differential rotation should be studied too, in addition to the uniform one. As shown in (Baumgarte et al., 2000; Morrison et al., 2004), differential rotation can lead to an increase in the maximum stable mass for configurations dynamically stable against radial collapse and bar formation. Furthermore, Shapiro (2000) studied the effects of magnetic braking and viscous damping on a differentially rotating star, suggesting a delay in the star collapse after a binary neutron star merger and the possibility to generate both a delayed gravitational wave burst and a gamma-ray burst.

Of course, since in this work we expanded the Hartle-Thorne metric only up to the second order in the angular velocity Ω, would be interesting to reach higher order expansion to see the effects on moment of inertia I as well as on the quadrupole moment Q.

On regard the Hartle-Thorne method to describe uniformly rotating neutron star, it should be implemented to give a wider and more realistic description of the stars, generalizing it by taking into account the contribution of both the electric and magnetic fields.

Still, a possible work to face with, would be to study the relation between the presence of the internal transition layer in between the core and the crust and the glitch phenomenon, to analyze the connection among mechanical and electromagnetic energy.

Chapter 4

Astrophysical Consequences of Realistic Neutron Stars

4.1 Introduction

In chapters 2 and 3, we have shown both for the static and the rotating case, how the traditional approach to study the equilibrium configurations for neutron stars, based on the solution of the Tolman-Oppenheimer-Volkoff (TOV) system of equations (Oppenheimer and Volkoff, 1939; Tolman, 1939), has to be superseded once the weak, strong, gravitational and electromagnetic interactions within a general relativistic framework are taken into account. The TOV equations must be then replaced by the Einstein-Maxwell system of equations coupled to the general relativistic Thomas-Fermi equations of equilibrium, giving raise to the what we have called the Einstein-Maxwell-Thomas-Fermi (EMTF) equations, (see Rotondo et al., 2011c; Rueda et al., 2011; Belvedere et al., 2012, for details). Uniform rotation has been introduced via the Hartle formalism. From the numerical integration of the EMTF equations in this rotating case, we computed the mass, equatorial and polar radii, eccentricity, moment of inertia I, quadrupole moment, the sequence of maximally rotating (Keplerian, $\Omega = \Omega_K$), as well as the bounds to mass, radius, and rotation frequency imposed by the secular axisymmetric instability.

From all we have shown in the previous chapters, it is clear that in the intervening years from the seminal work of Oppenheimer and Volkoff (1939) on neutron stars, much more has been learned concerning the EOS including the nuclear interactions, and on a more complex description of the structure parameters and stability of both static and rotating neutron stars.

However, it is common in the pulsar literature to infer neutron star as-

trophysical observables such as the surface magnetic field and radiation efficiency, by adopting fiducial structure parameters for the mass, radius, and moment of inertia. In this line, we would like also to introduce a word of caution on the use of analytic formulas existing in the literature for the determination of the maximum rotation frequency and of the moment of inertia of a neutron star.

In the first part of this chapter, we compare and contrast our values of Ω_K and I with the ones estimated through the claimed universal analytic formulas 1) for the Keplerian sequence by Lattimer and Prakash (2004), and 2) for the moment of inertia as a function of the compactness by Ravenhall and Pethick (1994) and by Lattimer and Schutz (2005), respectively. We show that those simple universal analytic formulas cannot properly describe the above properties of neutron stars, leading instead to inaccurate qualitative and quantitative results. We show that such inadequacy of the universal formulas is equally severe for both globally and locally neutral neutron stars.

In the second part of this chapter, we show that the use of realistic parameters of rotating neutron stars obtained from numerical integration of the self-consistent axisymmetric general relativistic equations of equilibrium leads to values of the magnetic field and radiation efficiency of pulsars very different from estimates based on fiducial parameters assuming a neutron star mass, $M = 1.4\ M_\odot$, radius $R = 10$ km, and moment of inertia, $I = 10^{45}$ g cm^2. We apply these considerations to the specific class high-magnetic field pulsars. We show that indeed all these sources can be described as canonical pulsars driven by the rotational energy of the neutron star with magnetic fields lower than the quantum critical field, for appropriate values of the neutron star mass.

This chapter is organized as follows. In section 4.2 we construct the Keplerian sequence of globally and locally neutral neutron stars, and compare qualitatively and quantitatively our results with the approximate analytic formula given by Lattimer and Prakash (2004). We analyze specifically the case of the fastest observed pulsar PSR J1748–2446ad (Hessels et al., 2006) with a frequency of 716 Hz, which is often used in the literature to constraint the mass-radius relation and so the EOS of the neutron stars (see e.g. Trümper, 2011b). In section 4.3 we calculate the moment of inertia of globally and locally neutral neutron stars and compare and contrast the results with the approximate formulas given by Ravenhall and Pethick (1994) and also Lattimer and Schutz (2005) for the moment of inertia as a function of the star compactness. We analyze in section 4.4 the estimates of the magnetic field and radiation efficiency of the high-magnetic field pulsars class, for which overcritical magnetic fields are inferred with fiducial parameters (see e.g. Ng and Kaspi, 2011). In section 4.5 we discuss our results and in section

4.6 we conclude giving some perspectives.

We use geometric units with $G = c = 1$ throughout unless otherwise specified.

4.2 Accuracy of Approximate Analytic Formulas for the Keplerian Sequence

It has been obtained by Lattimer and Prakash (2004) that the numerical value of the Keplerian frequency, namely the maximum rotation frequency, of a neutron star accounting for the effects of general relativity, deformation, and independent on the EOS, can be well fitted from the simple formula

$$f_K^{\rm L\&P} = \frac{\Omega_K^{\rm L\&P}}{2\pi} = 1045 \left(\frac{M_0}{M_\odot}\right)^{1/2} \left(\frac{10\,{\rm km}}{R}\right)^{3/2} {\rm Hz}\,, \tag{4.1}$$

providing the neutron star mass is not very close to the maximum stable value, where $\Omega_K^{\rm L\&P}$ is the Keplerian angular velocity described in (Lattimer and Prakash, 2004) and M_0 and R are the mass and the radius of the non-rotating star, respectively.

The Eq. (4.1) is often used to impose a constraint to the neutron star mass-radius relation (see e.g. Trümper, 2011b), by replacing $f_K^{\rm LP}$ with the frequency of the fastest observed pulsar PSR J1748–2446ad (Hessels et al., 2006), 716 Hz. Specifically, by doing this it can be obtained either an upper bound to the radius or a lower bound to the mass:

$$M_0 \geq \left(\frac{716}{1045}\right)^2 \left(\frac{R}{10\,{\rm km}}\right)^3 M_\odot \approx 0.47 \left(\frac{R}{10\,{\rm km}}\right)^3 M_\odot\,. \tag{4.2}$$

In Fig. 4.1 we show the approximate constraint, given by Eq. (4.2), represented by the gray dot-dashed curve together with the Keplerian sequence of globally and locally neutral neutron stars obtained in this work. We have also constructed the constant frequency sequence for fastest observed pulsar PSR J1748–2446ad with $f = 716$ Hz. The crossing point of this constant frequency curve with the Keplerian one is represented by a cyan-color star.

One should therefore expect that, if accurate, the dot-dashed curve passes over (or close to) the two cyan-color stars at the bottom of Fig. 4.1. It is clear that Eq. (4.2) is very far from representing correctly the position of a star on the Keplerian sequence, and this inconsistency is equally severe for both globally and locally neutral neutron stars. Quantitatively, we can see that Eq. (4.2) would predict for the same radius a much larger mass, namely

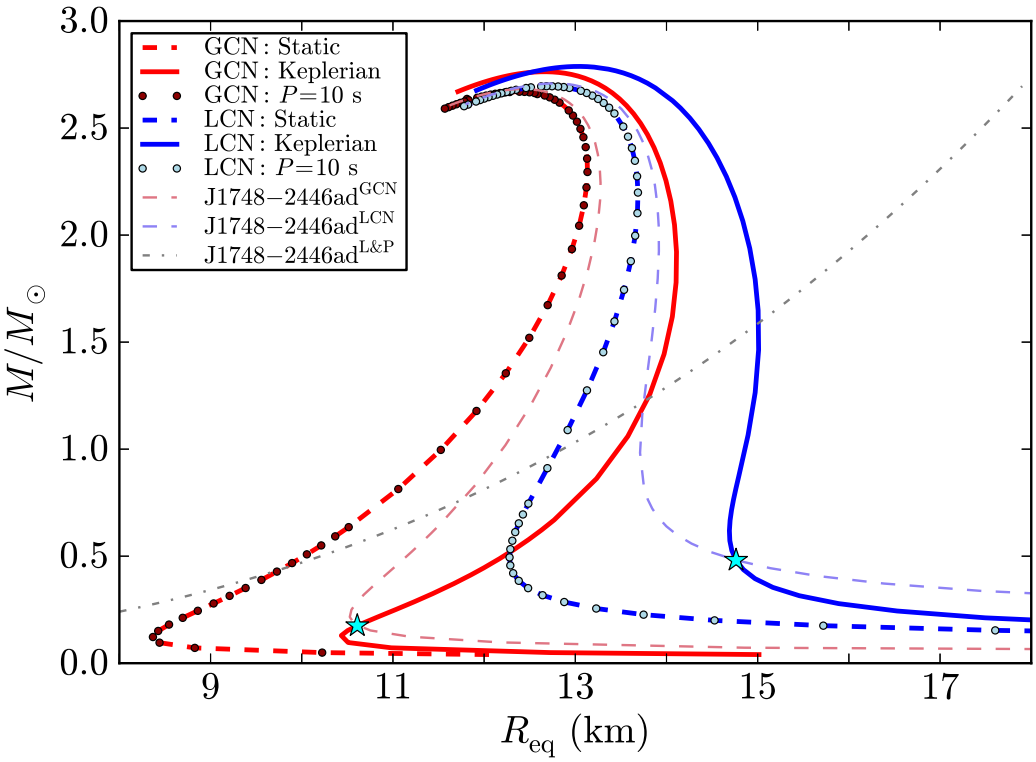

Figure 4.1: Gray dot-dashed line: constraint on the mass-radius relation given by Eq. 4.2, as shown in (Trümper, 2011b). Light-red and light-blue dashed lines: mass-radius relation for a constant rotational frequency f = 716 Hz, for the global and local charge neutrality respectively. The two cyan-color stars at the bottom of the plot represent the pulsar PSR J1748–2446ad for our new configuration and the traditional one, both along the Keplerian sequence. For the sake of comparison, we show also the sequences of constant rotation period $P = 10$ s ($f = 0.1$ Hz).

$M \approx 0.56\ M_\odot$ in the globally neutral case and $M \approx 1.5\ M_\odot$ in the locally neutral one; see Fig. 4.1.

The reason of the discrepancy between Eq. (4.1) and the real results, is as follows. The maximum Keplerian velocity can be written in terms of the non-rotating mass and radius of the neutron star as (see Belvedere et al., 2014)

$$\Omega_K^{J\neq 0} = \mathcal{C}\sqrt{\frac{M_0}{R^3}}\,, \tag{4.3}$$

or in terms of rotation frequency

$$f_K = \mathcal{C} \times 1833 \left(\frac{M_0}{M_\odot}\right)^{1/2} \left(\frac{10\,\mathrm{km}}{R}\right)^{3/2} \mathrm{Hz}\,, \tag{4.4}$$

where $\rho_c \equiv \rho(0)$ is the central density, and $\mathcal{C}$ is a coefficient given by

$$\mathcal{C} = \sqrt{\frac{1+\delta M/M_0}{(1+\delta R/R)^3}}\left[1 - jF_1(r) + j^2F_2(r) + qF_3(r)\right]\,, \tag{4.5}$$

with $\delta M = M - M_0$, $\delta R = R_{\rm eq} - R$ being M and $R_{\rm eq}$ the total mass and equatorial radius of the rotating star, $j = J/M_0^2$ and $q = Q/M_0^3$ are the dimensionless angular momentum and quadrupole moment. The functions F_i can be found in Appendix B.2 and Appendix A of (Belvedere et al., 2014), and the angular momentum J and the quadrupole moment Q are given by Eqs. 3.9 and 3.14, respectively.

In Fig. 4.2 we plot the dependence of the coefficient $\mathcal{C}$ in Eq. (4.3) as a function of the static neutron star mass, M_0. In contrast to the constancy of such a coefficient in the approximate analytic formula (4.1), we find that $\mathcal{C}$ has a non-trivial dependence on the central density (or the mass) of the star. Indeed, we obtain $0.720 \lesssim \mathcal{C}_{\rm GCN} \lesssim 0.912$ and $0.750 \lesssim \mathcal{C}_{\rm LCN} \lesssim 0.916$ for the global and local charge neutrality cases, respectively (see Fig. 4.2). This dependence is caused by the effects of general relativity, the angular momentum, the quadrupole deformation, and the specific EOS used. Therefore, the Eqs. (4.1) and (4.2) are, in general, not applicable for all neutron star models.

We show in Fig. 4.3 the accuracy of the approximate analytic formula for the Keplerian sequence given by Eq. (4.1) with respect to the actual value obtained from our numerical integrations, $1 - f_K^{\rm L\&P}/f_K$, where f_K is obtained via Eqs. (4.4) and (4.5).

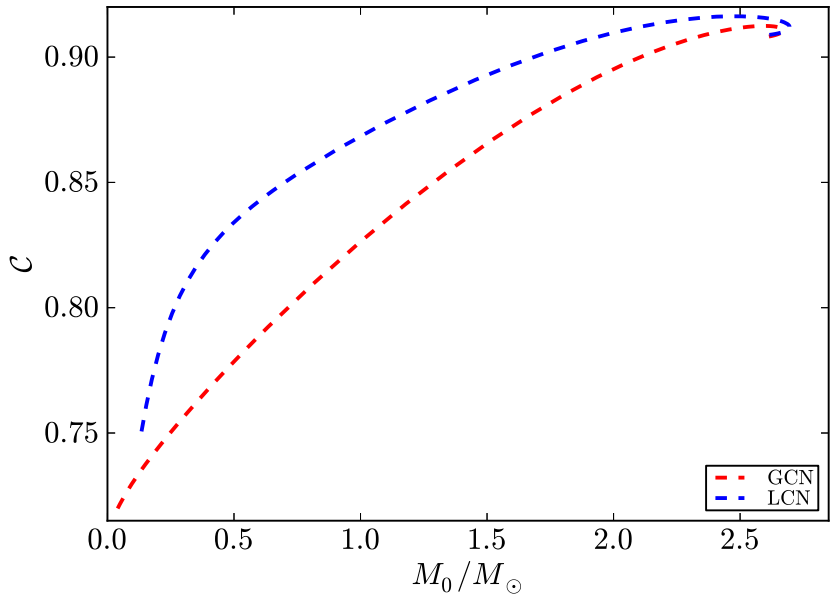

Figure 4.2: Coefficient $\mathcal{C}$ in Eq. (4.3) as a function of the mass of the non-rotating neutron star for both global and local charge neutrality.

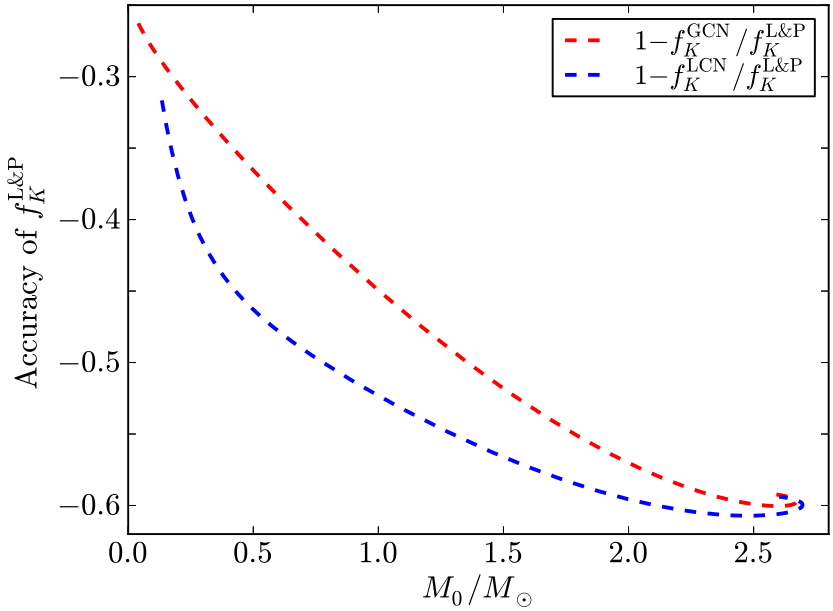

Figure 4.3: Accuracy of the approximate formula (4.1) by Lattimer and Prakash (2004) with respect to the numerical values obtained from Eqs. (4.4) and (4.5) for both global (red dashed) and local (blue dashed) charge neutrality cases, as a function of the non-rotating neutron star mass, M_0.

4.3 Accuracy of Approximate Analytic Formulas for the Moment of Inertia

It has been claimed in the literature the possibility of constructing model-independent approximate analytic formulas to compute the moment of inertia of a neutron star as a function of its compactness, $GM_0/(c^2R)$.

Ravenhall and Pethick (1994) for instance obtained that, within 10% of accuracy, the moment of inertia for a large variety of the EOS existing at the time is fitted by the formula

$$\frac{I_{\rm R\&P}}{M_0R^2} = 0.21\left(1-2\frac{GM_0}{c^2R}\right)^{-1}, \tag{4.6}$$

except for those configurations with masses $M_0 \lesssim M_\odot$.

Lattimer and Schutz (2005) calculated the moment of inertia for several hadronic EOS and concluded that $I/(M_0R^2)$ follows approximately the following universal expression

$$\frac{I_{\rm L\&S}}{M_0R^2} = (0.237\pm 0.008)\left[1+2.84\frac{GM_0}{c^2R}+18.9\left(\frac{GM_0}{c^2R}\right)^4\right], \tag{4.7}$$

for EOS that leads to maximum masses larger than $1.6M_\odot$ and for values $M_0/R \gtrsim 0.07\ M_\odot/\text{km}$ and $M \geq M_\odot$.

In Fig. 4.4 we compare the approximate formulas (4.6) and (4.7) with the actual behavior of $I/(M_0R^2)$ as a function of the neutron star compactness.

We show in Fig. 4.5 the accuracy of the approximate formulas (4.6) and (4.7) with respect to the numerical values obtained from Eq. (3.27) for both globally and locally neutral neutron stars. Namely, we plot as a function of the compactness the value of $1-I_{\rm GCN}/I_{\rm R\&P,L\&S}$ and $1-I_{\rm LCN}/I_{\rm R\&P,L\&S}$. We can see the performance of the above approximate formulas is in general not accurate. The accuracy improves with increasing compactness and in particular for configurations very close to the one of maximum mass. However, it is clear that the above approximate formulas cannot be considered as good approximations for the moment of inertia of any neutron star since the qualitative and quantitative behavior of it depends very strongly on the nuclear EOS. As we have shown here, these particular descriptions fail in the case of stiff EOS as the ones given by relativistic nuclear mean field theory models.

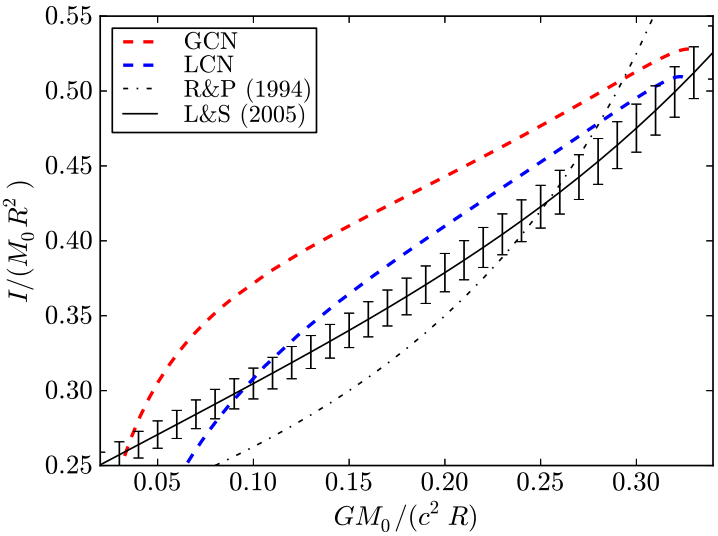

Figure 4.4: Comparison between the approximate formulas (4.7) and (4.6) by Lattimer and Schutz (2005) and Ravenhall and Pethick (1994), respectively, with the real behavior of $I/(M_0R^2)$ as a function of the compactness parameter of the neutron star, $GM_0/(c^2R)$. We have also plotted the errors of the formula (4.7) as calculated by Lattimer and Schutz (2005).

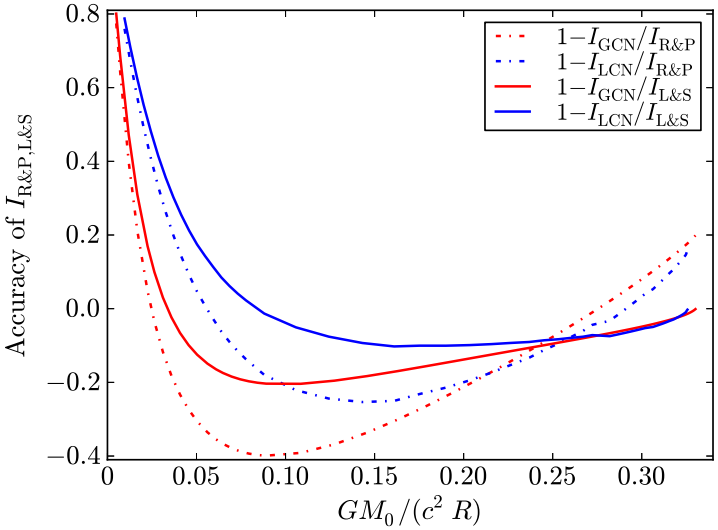

Figure 4.5: Accuracy of the approximate formulas (4.7) and (4.6) by Lattimer and Schutz (2005) and Ravenhall and Pethick (1994), respectively, with respect to the numerical values obtained from Eq. (3.27) for both globally and locally neutral neutron stars, as a function of the compactness, $GM_0/(c^2R)$.

4.4 Implications on the Magnetic-Dipole Model of Pulsars

The upper limit on the magnetic field of a pulsar (see e.g. (Ferrari and Ruffini, 1969)), obtained by requesting that the rotational energy loss due to the dipole field be smaller than the electromagnetic emission of the dipole, is given by

$$B = \left(\frac{3c^3}{8\pi^2}\frac{I}{R^6}P\dot{P}\right)^{1/2}, \tag{4.8}$$

where P and $\dot{P}$ are the rotational period and the spin-down rate of the pulsar which are observational properties, and the moment of inertia I and the radius R of the object are model dependent properties.

In literature of pulsars are generally used fiducial parameters of the canonical neutron star $M = 1.4M_\odot$, $R = 10$ km, and moment of inertia $I = 10^{45}$ g cm^2, for which Eq. (4.8) becomes

$$B_f = 3.2 \times 10^{19}\left(P\dot{P}\right)^{1/2}\,\mathrm{G}\,. \tag{4.9}$$

The loss of rotational energy within this model is given by

$$\dot{E}_{\rm rot} = -4\pi^2 I\frac{\dot{P}}{P^3}\,, \tag{4.10}$$

that for the aforementioned fiducial values becomes

$$\dot{E}^f_{\rm rot} = -3.95 \times 10^{46}\frac{\dot{P}}{P^3} \quad \mathrm{erg\ s^{-1}}\,. \tag{4.11}$$

There is an interesting family of pulsars known as high-magnetic field pulsars characterized by surface magnetic fields, inferred from their period and spin-down rates thorough Eq. (4.9), close or in some cases even larger than the quantum critical field (see e.g. Ng and Kaspi, 2011; Zhu et al., 2011, and Table 4.1 for details):

$$B_c = \frac{m_e^2c^2}{e\hbar} = 4.41 \times 10^{13}\ \mathrm{G}\,. \tag{4.12}$$

Due to this fact, it has been suggested the possibility that this family of pulsars can be the missing link, i.e. transition objects, between rotation powered pulsars and the so-called magnetars: neutron stars powered by the decay of overcritical magnetic fields. In principle this would lead to a large unseen

population of magnetars in a quiescence state which could be disguised as radio pulsars (see e.g. Zhu et al., 2011, for details).

However, as we shall show below, these conclusions might be premature since the magnetic fields, inferred using a neutron star of fiducial parameters, are in general overestimated. Indeed, lower values of the magnetic field are obtained when realistic structure parameters are used. In particular, they could be in some cases larger by almost an order of magnitude when compared with the magnetic field obtained from Eq. (4.8) using realistic mass-radius relations and the corresponding general relativistic moment of inertia. We shall show that both different theoretical models or, for a fixed model, different structure parameters as a function of the central density and/or rotation frequency of the star, can give rise to quite different quantitative estimates of the astrophysical observables.

To analyze the magnetic fields and the efficiency of pulsars in converting rotational energy into electromagnetic radiation, we focus, in particular, on what it is known in the literature as the high-magnetic field pulsar class (see Ng and Kaspi, 2011). In Table 4.1, we show a sample of this class for which magnetic fields higher than the critical value (4.12) have been inferred (see second column of the table) using fiducial values of the neutron star parameters.

High-Magnetic Field Pulsars				
J-Name	B_f/B_c	L_X (10^{33} erg s^{-1})	P (s)	$\dot{P}$ (10^{-12})
J1846–0258	1.11	$25-28^{1}$, $120-170^{2}$	0.32568424880	7.083300
J1819–1458	1.13	$1.8-2.4$	4.26316403290	0.575171
J1734–3333	1.18	$0.1-3.4$	1.16900829800	2.278980
J1814–1744	1.24	<43	1.16934068500	2.279410
J1718–3718	1.67	$0.14-2.6$	3.37820652870	1.598150
J1847–0130	2.13	<34	6.70704572410	1.274900

[1] in 2000, prior to the 2006 outburst
[2] during the outburst in 2006

Table 4.1: Magnetic fields of the overcritical high-magnetic field pulsars obtained assuming fiducial neutron star parameters, $R = 10$ km and $I = 10^{45}$ g cm^2, respectively, namely using Eq. (4.9). See Zhu et al. (2011); Ng and Kaspi (2011) for additional details of these pulsars.

In Fig. 4.6 we show the ratio between the magnetic field obtained via Eq. (4.8) using the realistic mass-radius relations of globally and locally neutral neutron stars used in this work and the one obtained with fiducial parameters given by Eq. (4.9), which we denote to as B_f. We did this for both

static and maximally rotating (Keplerian sequence) neutron stars. For the rotating stars we substitute the radius R in Eq. (4.8) by the mean-radius, $\langle R\rangle = (2R_{\rm eq} + R_p)/3$, where $R_{\rm eq}$ and R_p are, respectively, the equatorial and polar radii.

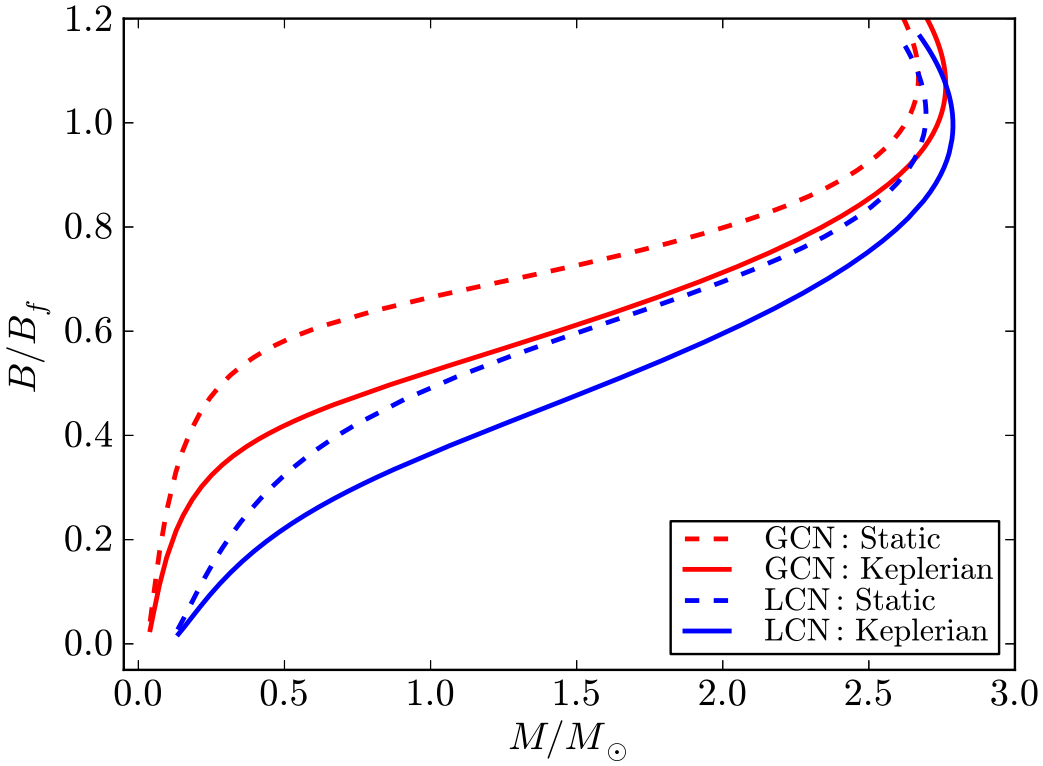

Figure 4.6: Ratio between the magnetic field given by Eq. (4.8) obtained with the realistic mass-radius relations of globally and locally neutral neutron stars of this work and the one obtained with fiducial parameters, given by Eq. (4.9).

We can see from this figure that the inferred magnetic field decreases with the neutron star mass. Therefore, the configurations of maximum and minimum mass give us respectively upper and lower limits to the magnetic field.

In Fig. 4.8 we plotted our theoretical prediction for magnetic fields of the pulsars of Table 4.1 as a function of the neutron star mass. In this case we use the static approximation, namely we adopted the radius of the non-rotating configurations to be consistent with the moment of inertia obtained by the Hartle approach at second order, which as we mentioned above does not account for the effects of deformation due to rotation. This is in principle

a good approximation for this family of pulsars since their rotation periods are well far the millisecond region, where appreciable deviations from spherical symmetry are expected. See for instance in Fig. 4.7 the sequence of configurations with rotation period $P = 10$ s which practically overlaps the static mass-radius relation. It can be also noticed from Fig. 4.6, that the non-rotating approximation give us an upper limit to the magnetic field with respect to the value obtained from the actual rotating configuration.

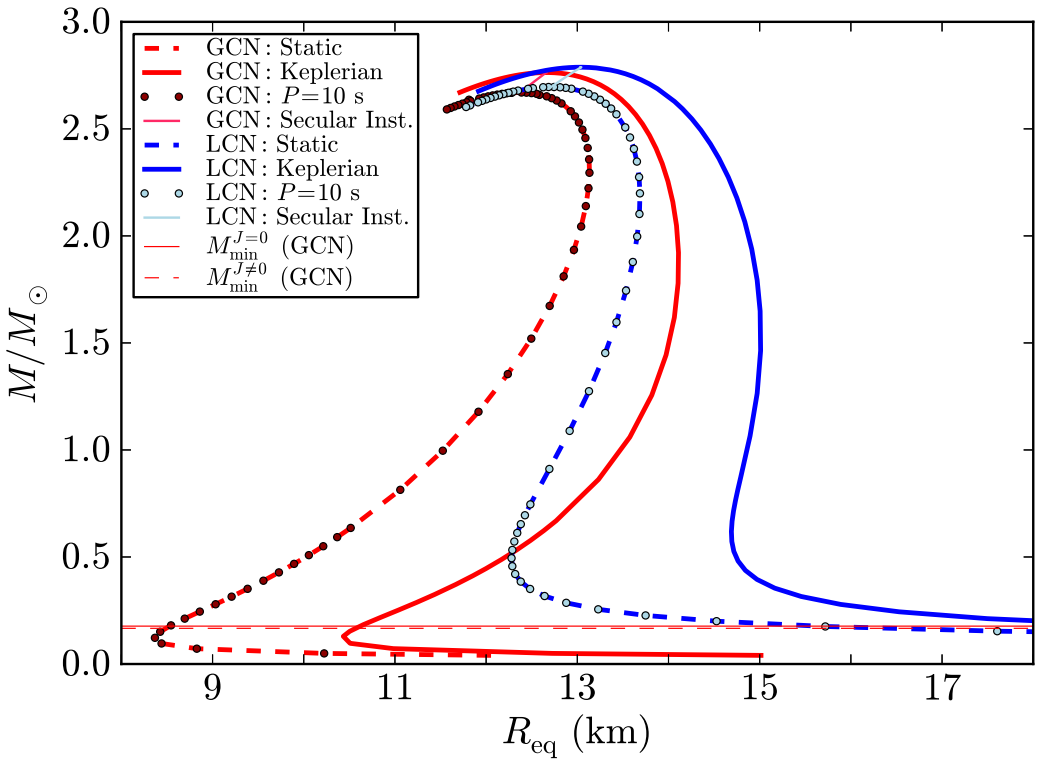

Figure 4.7: Comparison between the mass-radius relation for the $P = 10$ s, the static and the Keplerian sequences. As can be seen, the $P = 10$ s lines, here in darkred and lightblue color for the global and the local charge neutron star respectively, almost overlap the static configurations.

We find that, in the global neutrality case, PSR J1847–0130 and PSR J1718–3718 are under-critical up to a mass $M_0 \approx 0.25\ M_\odot$, and $M_0 \approx 0.65\ M_\odot$, respectively, while the other pulsars are under-critical up to masses $M_0 \approx 2.3$–$2.5\ M_\odot$. In the local charge neutrality case, PSR J1847–0130 and PSR J1718–3718 are under-critical up to a mass $M_0 \approx 0.9\ M_\odot$ and $M_0 \approx 1.5\ M_\odot$ respectively, while the other sources up to masses $M_0 \approx 2.5$–$2.7\ M_\odot$.

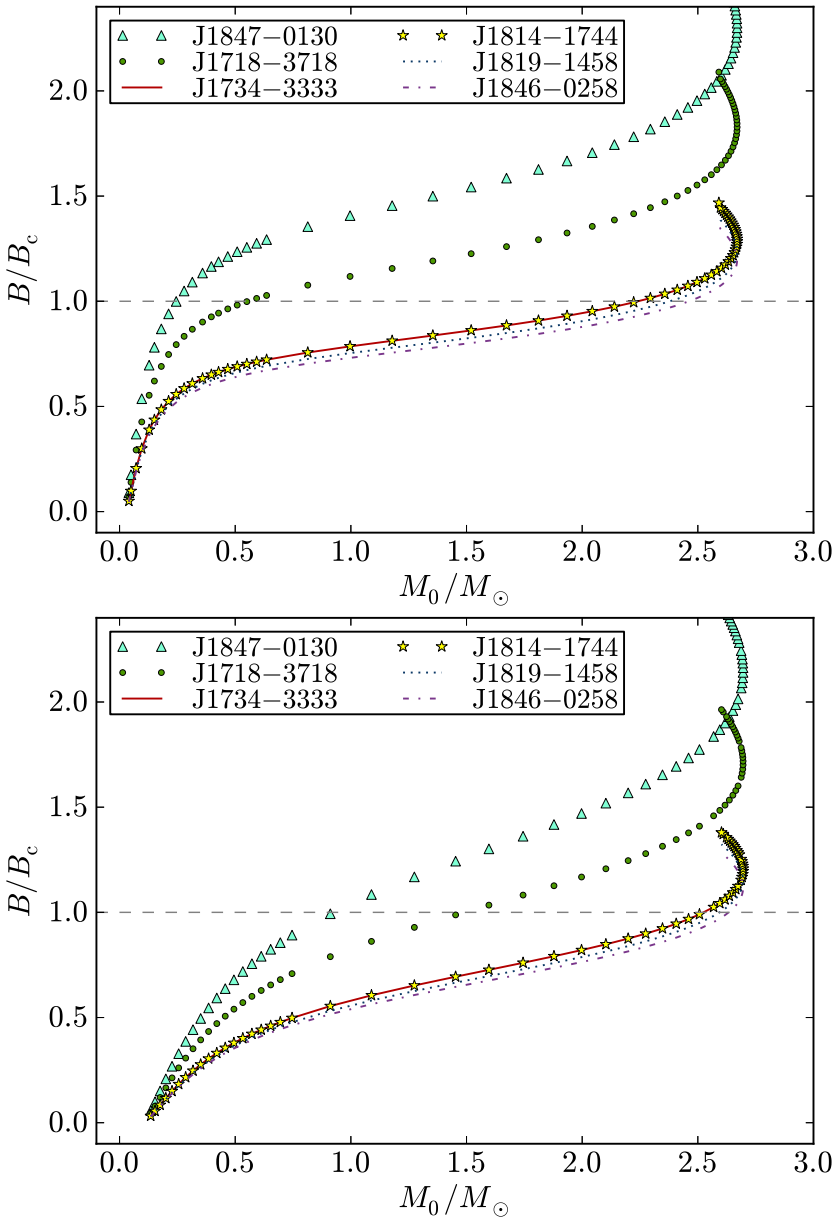

Figure 4.8: Magnetic field B in the dipole approximation, in units of critical magnetic field B_c, as function of the mass (in solar masses) for static neutron stars in the global (upper panel) and local (lower panel) charge neutrality cases. We show the high-magnetic field pulsar of Table 4.1 for which overcritical values ($B/B_c > 1$) are obtained using fiducial neutron star parameters.

Concerning the efficiency of pulsars in converting rotational energy into electromagnetic radiation, we show in Fig. 4.9 the X-ray luminosity to rotation energy loss ratio, $L_X/\dot{E}_{\rm rot}$, as a function of the neutron star mass, for both global and local charge neutrality.

We find that for both globally and locally neutral neutron stars $L_X < \dot{E}_{\rm rot}$: 1) in PSR J1718–3718 for $M_0 \gtrsim 1.2\ M_\odot$ and for the entire range of masses adopting, respectively, the observational upper or lower limits on L_X; 2) in PSR J1814–1744 for $M_0 \gtrsim 0.8\ M_\odot$ using the upper limit on L_X; 3) for the rest of the objects in the entire range of stable masses.

The only exception to the above rule are PSR J1847–0130 and PSR J1819–1458, for which no range of masses with $L_X < \dot{E}_{\rm rot}$ was obtained. However, for PSR J1847–0130 we have only an upper limit for L_X, so there is still room for solutions with $L_X < \dot{E}_{\rm rot}$ if future observations lead to an observed value lower than the present upper limit. In this line, the only object with $L_X > \dot{E}_{\rm rot}$ for any mass is PSR J1819–1458. For this particular object there is still the possibility of being a rotation powered neutron star since the currently used value of the distance to the source, 3.6 kpc, inferred from its dispersion measure, is poorly accurate with a considerable uncertainty of at least 25% (see McLaughlin et al., 2007, for details). Indeed, a distance to the source 25% shorter than the above value would imply $L_X < \dot{E}_{\rm rot}$ for this object in the mass range $M_0 \gtrsim 0.6\ M_\odot$.

It is also worth to mention that the rotation energy loss (4.10) depends on the neutron star structure only through the moment of inertia, whose quantitative value can be different for different nuclear EOS and/or owing to an improved value accounting for deviations from the spherical geometry, for instance considering a third-order series expansion in Ω. However, the latter effect is negligible for this specific case ($P \approx 4.3$ s), see for instance Fig. 5 in (Benhar et al., 2005), where no deviations of I from its spherical value appear for such long rotation periods.

4.5 Conclusions

It is common in the pulsar literature to infer neutron star astrophysical observables such as the surface magnetic field and radiation efficiency, by adopting fiducial structure parameters for the mass, radius, and moment of inertia. In addition, in order to put constraints to the mass-radius relation, simple analytic formulas for the sequence of neutron stars with maximum rotation frequency are used.

However, in this chapter we explored the consequences of a realistic model for neutron stars on the inference of the astrophysical observables of pulsars.

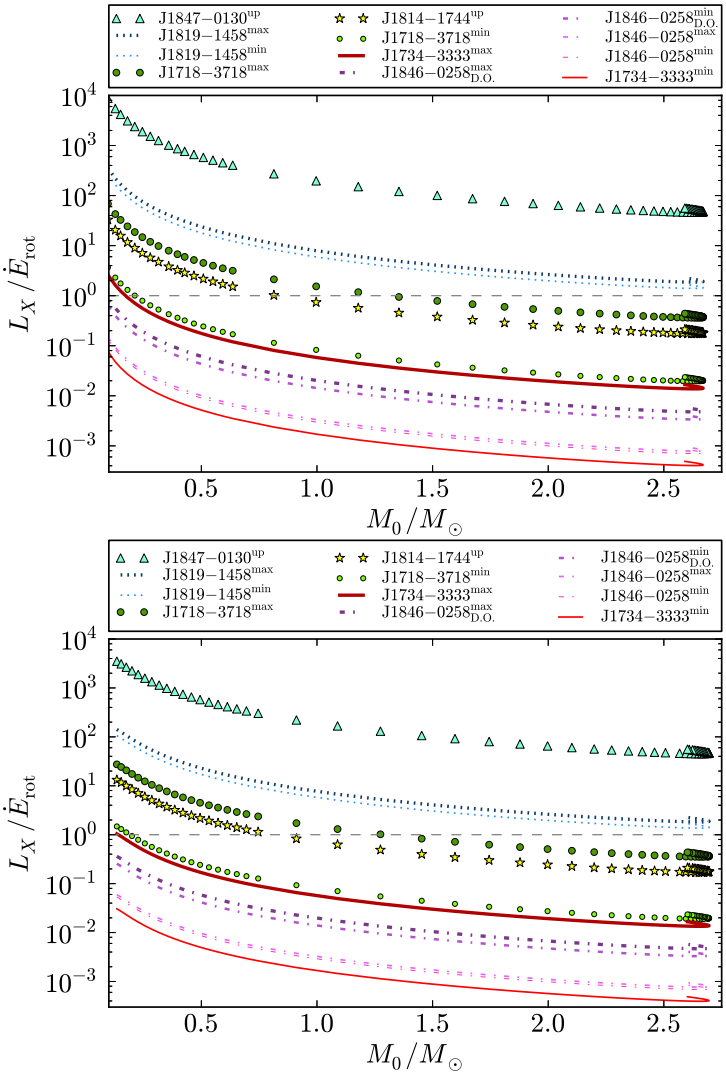

Figure 4.9: Ratio between the observed X-ray luminosity L_X and the loss of rotational energy $\dot{E}_{rot}$ versus total mass of the non-rotating neutron star, in units of $M_\odot$. Are drawn the high-B pulsar from the work by Ng and Kaspi (2011) for which a magnetic field higher than the critical field B_c is inferred, once the fiducial value for the moment of inertia $I = 10^{45}$ g cm^2 is taken into account (see Table 4.1). Pulsars with luminosity L_X defined by an upper limit are labeled with "up", for pulsars with luminosity L_X not well established we have assumed the existent lower limits (label "min") and upper limits (label "max") on it. The values for the pulsar PSR J1846–0258 are dived in prior the 2006 outburst and during the 2006 outburst (label "D.O."). Top plot: global charge neutrality. Bottom plot: local charge neutrality. The magnetic fields shown are referred to the high-magnetic field pulsars of Table 4.1.

We have shown here that the properties of neutron stars obtained from the solution of the Einstein-Maxwell-Thomas-Fermi equations for uniform rotation leads to a very different results with respect to the ones obtained with such simple formulas and fiducial parameters.

We showed the inaccuracy of the analytic universal formulas by Lattimer and Prakash (2004) for the Keplerian sequence, and by Ravenhall and Pethick (1994) and Lattimer and Schutz (2005) for the moment of inertia of neutron stars. Indeed, no simple formulas can be found for the neutron star properties analyzed in this work, and the use of universal formulas leads, instead, to inadequate qualitative and quantitative results owing to the effects of general relativity, angular momentum, quadrupole deformation, and the specific EOS used; see Figs. 4.2–4.5.

We showed that the magnetic field inferred from the magnetic-dipole formula can be overestimated up to one order of magnitude if fiducial parameters are adopted. We analyzed in addition the specific case of the high-magnetic field pulsar class, for which overcritical magnetic fields have been obtained in the literature with the use of fiducial neutron star parameters. We found that, instead, the magnetic field of all the high-magnetic field pulsars turn to be under-critical for appropriate values of the neutron star mass. This non-trivial dependence of the inferred magnetic field on the neutron star mass, in addition to the dependence on P and $\dot{P}$, namely $B = B(I(M_0), R(M_0), P, \dot{P})$, leads to the impossibility of accommodating the pulsars in a typical $\dot{P} - P$ diagram together with a priori fixed values of the magnetic field; see Fig. 4.8.

We finally computed the range of neutron star masses for which the X-ray luminosity of these pulsars can be well explained via the loss of rotational energy and therefore they fall into the family of ordinary rotation powered pulsars. The only possible exceptions were found to be PSR J1847–0130 and PSR J1819–1458, which however, as we argued, still present observational uncertainties in the determination of their distances and/or luminosities that leave room for a possible explanation in terms of spin-down power.

We also discussed the possible effects of different nuclear models as well as the improved values of the moment of inertia given by further expansion orders of the slow rotation approximation or full numerical integration of the equilibrium equations in the rotating case. However, the former effect appears to be negligible for the long rotation periods, $P \sim 10$ s, of the high-magnetic field pulsars (see e.g. Fig. 5 in Benhar et al., 2005).

It is worth to underline that the validity of the results of this work will very likely apply also to different nuclear EOS consistent with the current observational constraints, as suggested by the high value of the recently measured mass of PSR J0348+0432, $M = 2.01 \pm 0.04 M_\odot$ (Antoniadis et al., 2013). Such a high value favors stiff nuclear EOS, as the one used here based on

relativistic nuclear mean field theory á la Boguta and Bodmer (1977), which lead to a critical mass of the neutron star higher than the above value.

We have shown that the above results apply both for global charge neutrality as well as in the limit of local neutrality.

4.6 Perspectives

As for the chapters 2 and 3, all the quantities studied here, should be compared and contrasted both once a different nuclear model is taken into account and a higher order expansion of the Hartle-Thorne metric on respect the angular velocity Ω is carried out. In particular, to perform an expansion of the metric to an order higher than the third, would take into account the effects of rotation on the moment of inertia I and, as consequence, on the quadrupole moment Q and the dipole magnetic field B. In this way, it would be possible to study the magnetic field of neutron stars rotating at a higher rate with respect to the one analyzed here. In fact, in this work we analyzed stars rotating at a rate so slow that allow us to neglect the rotation itself on respect the moment of inertia. Considering higher order expansion in Ω would lead to introduce the effect of rotation on the quantities involved in the description of dipole magnetic field, namely to analyze the effect of the flattening of the star due to the fast rotation. In principle this means that other family of pulsar in addition the ones studied here could be taken into account, as, for example, the millisecond pulsars.

Chapter 5

Conclusions

We have formulated the equations of equilibrium of neutron stars both in the static and the uniformly rotating configurations. The strong, weak, electromagnetic, and gravitational interactions are taken into due account within the framework of general relativity. The nuclear forces are modeled through the σ-ω-ρ strong forces model, where the interactions between nucleons are described by the exchange of the σ, ω, and ρ virtual mesons.

We shown how the TOV system of equations has to be superseded withe EMTF one, and we solved such a system in the case of zero temperature for different parameterizations of the nuclear model.

We performed the integration of the equilibrium equations both for the static and the rotating case, both for the global charge neutrality case and a traditional configuration with the local charge neutrality.

We found a new structure for the neutron stars. We have a charged core at supranuclear density, surrounded by a tiny layer of opposite charge screening it, in its turn enclose by a neutral ordinary crust at lower density.

The equilibrium condition are given by the constancy of the Klein potentials along the configuration, leading to a discontinuity in the density at the transition from the core to the crust, and correspondingly an overcritical electric field $\sim (m_\pi/m_e)^2 E_c$ develops in the boundary interface. The continuity of the Klein potentials at the core-crust boundary interface leads to a decreasing of the electron chemical potential and density, until values $\mu_e^{\rm crust} < \mu_e^{\rm core}$ and $\rho_{\rm crust} < \rho_{\rm core}$ at the edge of the crust, where global charge neutrality is achieved.

For each central density, an entire family of core-crust interface boundaries and, correspondingly, an entire family of crusts with different mass and thickness, exist. The larger $\rho_{\rm crust}$, the smaller the thickness of the interface, the peak of the electric field, and the larger the mass and the thickness of the crust. The configuration with $\rho_{\rm crust} = \rho_{\rm drip} \sim 4.3 \times 10^{11}$ g/cm^3 separates

neutron stars with and without inner crust. In this work we limited our analysis to configuration with density $\lesssim \rho_{\rm drip}$.

Our new neutron stars have crusts with masses and thickness smaller than the ones obtained from the traditional TOV treatment, and our new mass-radius relation is in line with observations.

To construct the equilibrium configurations of uniformly rotating neutron stars in the slow rotation regime, we applied the Hartle-Thorne formalism. This approach perform an expansion of the metric on respect the angular velocity Ω of the star. We performed the expansion of the metric up to the third order in Ω, so to calculate the mass, polar and equatorial radii, angular momentum, moment of inertia, quadrupole moment, and eccentricity, as functions of the central density and the rotation angular velocity of the neutron star.

To construct the region of stability of rotating neutron stars, we analyzed the Keplerian mass-shedding limit and the secular axisymmetric instability.

We have established the maximum mass and maximum rotation frequency of the neutron star. We computed the gravitational binding energy of the configurations as a function of the central density and rotation rate. We found that there is a minimum mass under which the neutron star becomes gravitationally unbound once a globally neutral neutron star is considered, while the locally neutral neutron stars are always bound. Even for the rotating neutron stars, our mass-radius relation is in line with observations.

At the end, we compared and contrasted some physical quantities of neutron stars obtained through the integrations of our system of equations, with the same quantities derived through the adoption of fiducial values and by using approximate analytic formulas in the literature. We shown that the use of both the fiducial values and the analytical formulas should be done with caution.

We, then, applied our results to the astrophysics of pulsars. We showed that the magnetic field inferred from the magnetic-dipole formula can be overestimated up to one order of magnitude if fiducial parameters are adopted. We analyzed in addition the specific case of the high-magnetic field pulsar class, for which overcritical magnetic fields have been obtained in the literature with the use of fiducial neutron star parameters. We found that, instead, the magnetic field of all the high-magnetic field pulsars turn to be under-critical for appropriate values of the neutron star mass. We finally showed that the X-ray luminosity of these pulsars can be well explained via the loss of rotational energy and therefore they fall into the family of ordinary rotation powered pulsars.

Chapter 6

IRAP & ICRANet–Sapienza University of Rome Ph.D Activities

In this section are listed my activities during my IRAP PhD–Sapienza University of Rome period.

Research Experiences

During my IRAP PhD (International Relativistic Astrophysics Ph.D.) held at Sapienza–University of Rome, I have been working with Professor Ruffini and Dr. Jorge Rueda on a new configuration for the neutron stars. Initially, we formulated the equilibrium equations for static neutron stars, taking into account strong, weak, electromagnetic, and gravitational interactions within the framework of general relativity and relativistic nuclear mean field theory. We shown that the Tolman-Oppenheimer-Volkoff (TOV) equations are superseded and the use of the Einstein-Maxwell-Thomas-Fermi (EMTF) system of equations is mandatory. The key points are the constancy of the general relativistic Fermi energies of particles, the "Klein potentials", throughout the configuration, and the use of the global charge neutrality over the whole configuration as requested by the EMTF system of equations, replacing the generally used local one. The solution of the EMTF equations leads to a new structure of the neutron stars: a positively charged core at supranuclear density, surrounded by an electron layer of thickness of the order of the electron screening scale, and at lower density, a neutral ordinary crust.

Then, we introduced rotation on the new neutron stars model, following

the slow rotation approximation in the Hartle-Thorne formalism. Integrating the equations of equilibrium for different central densities and circular velocities, we have been able to compute mass, polar and equatorial radii, angular momentum, eccentricity and quadrupole moment of the configurations. We took account of the Keplerian mass-shedding limit and the axisymmetric secular instability. We computed the minimum mass for the globally neutral neutron stars, under which them result gravitationally unbound. No unbound configurations have been found for the locally neutral neutron stars, meaning that no minimum mass limit exist for this case.

Afterward, we showed the inaccuracy of some analytic universal formulas, generally used in the literature, for the Keplerian sequence and for the moment of inertia of neutron stars. The values for the moment of inertia I and the Keplerian rotational frequency f_K, obtained through our model, have been compared and contrasted with such formulas. We analyzed the effect on the magnetic field of pulsars on respect to the case in which fiducial parameters are used. We showed that the magnetic field inferred from the magnetic-dipole formula can be overestimated up to one order of magnitude if fiducial parameters are adopted. We analyzed in particular the case of the high-magnetic field pulsar class. We found that the magnetic field of all the high-magnetic field pulsars can turn to be under-critical for appropriate values of the neutron star mass. We finally computed the range of neutron star masses for which the X-ray luminosity of these pulsars can be well explained via the loss of rotational energy and therefore they fall into the family of ordinary rotation powered pulsars.

Schools, Meetings, Conferences, Seminars and Workshops

- 3^{rd} **Stuckelberg Workshop**, (main lectures by Prof. G.'t Hooft) Pescara, Italy, July 8-18 2008.

- **12**th **Marcel Grossmann Meeting on General Relativity**, Paris, France, July 12-18 2009.

- **6**th **Italian-Sino Workshop in Relativistic Astrophysics**, Pescara, Italy, June 29 - July 1 2009.

- **The Shocking Universe Meeting**, S.Servolo-Venezia, Italy, September 14-18 2009.

- **IRAP Ph.D. Lectures**, Nice Observatoire de la Cote d'Azur, Nice, France, February 1-19 2010.
- **IRAP Ph.D. School**, Università di Ferrara, Italy, March 22-26 2010.
- **The second Galileo - Xu Guangqi meeting**, Ventimiglia, Italy, July 12-18 2010.
- **25th Texas symposium on Relativistic Astrophysics (Texas 2010)**, Heidelberg, Germany, December 6-10 2010.
- **Recent News from the GeV and TeV Gamma-Ray Domains: Results and Interpretations Workshop**, Pescara, Italy, March 21-25 2011.
- **IRAP Ph.D. Erasmus Mundus Workshop From Nuclei to White Dwarfs and Neutron Stars**, Les Houches, France, April 3-8 2011.
- **First Caribbean Symposium on Nuclear and Astroparticle Physics - STARS2011**, La Habana, Cuba, May 1-4 May 2011.
- **2nd International Symposium on Strong Electromagnetic Fields and Neutron Stars - SMFNS2011**, Varadero, Cuba, May 5-7 2011.
- **IRAP Ph.D. Erasmus Mundus school**, Universite de Nice Sophia Antipolis, Nice, France, May 25 - June 10 2011.
- **12th Italian-Korean Symposium**, Pescara, Italy, July 4-8 2011.
- **Erasmus Mundus - Irap PhD Lectures**, Universite de Nice Sophia Antipolis, Nice, France, September 5-16 2011.
- **Second Ferrara Workshop on X-Ray Astrophysics up to 511 keV**, Università di Ferrara, Italy, September 14-16 2011.
- **The Sun, the Stars, the Universe and General Relativity - Third Galileo - Xu Guangqi meeting**, National Astronomical Observatories, Beijing, China, October 11-15 2011.
- **CompStar: the physics and astrophysics of compact stars**, Tahiti, French Polynesia, June 4-8 2012.
- 13th **Marcel Grossmann Meeting**, Stockholm, Sweden, July 1-7 2012.
- 39th **COSPAR Scientific Assembly**, Mysore, India, July 14-22 2012.

- **CompStar 2012 School-Equation of State for Compact Star Interiors and Supernovae**, Zadar, Croatia, September 24-28 2012.

Given Talks

- Recent News from the GeV and TeV Gamma-Ray Domains: Results and Interpretations Workshop, Pescara, Italy, March 21-25 2011. *Mass, Radius and Moment of Inertia of Neutron Stars* (talk).

- IRAP Ph.D. Erasmus Mundus Workshop From Nuclei to White Dwarfs and Neutron Stars, Les Houches, France, April 3-8 2011. *Mass, Radius and Moment of Inertia of Neutron Stars* (talk).

- IRAP Ph.D. Erasmus Mundus school, Universite de Nice Sophia Antipolis, Nice, France, May 25 - June 10 2011. *Mass, Radius and Moment of Inertia of Neutron Stars* (PhD school lecture).

- Erasmus Mundus - Irap PhD Lectures,Universite de Nice Sophia Antipolis, Nice, France, September 5-16 2011. *Neutron stars: a new approach* (PhD school lecture).

- 12^{th} Italian-Korean Symposium, Pescara, Italy, July 4-8 2011. *Mass, Radius and Moment of Inertia of Neutron Stars* (Invited talk).

- Erasmus Mundus - Irap PhD Lectures, Universite de Nice Sophia Antipolis, Nice, France, September 5-16 2011. *Neutron Stars: a new approach and an introductory lesson* (PhD school lecture).

- Second Ferrara Workshop on X-Ray Astrophysics up to 511 keV, Ferrara, September 14-16 2011.
  Mass, Radius and Moment of Inertia of Neutron Stars (Invited talk) (http:adsabs.harvard.edu/abs/2011xau5.confE...7B).

- The Sun, the Stars, the Universe and General Relativity - Third Galileo - Xu Guangqi meeting, National Astronomical Observatories, Beijing, China, October 11-15 2011. *Neutron Star Core in the Global Charge Neutrality Picture* (talk).

- CompStar: the physics and astrophysics of compact stars, Tahiti, French Polynesia, June 4-8 2012. textitNeutron star equilibrium configurations within a fully relativistic theory with strong, weak, electromagnetic, and gravitational interactions (talk).

- 13^{th} Marcel Grossmann Meeting, Stockholm, Sweden, July 1-7 2012. *Neutron star equilibrium configurations within a fully relativistic theory with strong, weak, electromagnetic and gravitational interactions* (talk).
- 39^{th} COSPAR Scientific Assembly, Mysore, India, July 14-22 2012. *Moment of inertia, radii, surface emission from a new theoretical understanding of Neutron Stars* (talk).
- Invited talk to the Catania INFN section, by Prof. Fiorella Burgio, Catania, Italy, October 28-31 2012. *Neutron star equilibrium configurations within a fully relativistic theory with strong, weak, electromagnetic and gravitational interactions* (invited talk).

Publications

Published Papers

1. R. Belvedere, Jorge A. Rueda, R. Ruffini and S.-S. Xue, *"The influence of the core on the structure of the outer crust of neutron stars"*. Published online as volume 123 in *Proceedings of Science (POS)*.
2. R. Belvedere, Jorge A. Rueda and R. Ruffini, *"Mass, radius and moment of inertia of neutron stars"*, Int. J. Mod. Phys. E **20**, (2011) 208–213.
3. R. Belvedere, D. Pugliese, Jorge A. Rueda, R. Ruffini and S.-S. Xue, *"Neutron star equilibrium configurations within a fully relativistic theory with strong, weak, electromagnetic, and gravitational interactions"*. Nucl. Phys. A **883**, (2012) 1–24.
4. R. Belvedere, Jorge A. Rueda and R. Ruffini, *"Neutron stars within a general relativistic theory including strong,weak and electromagnetic interactions"*. Nuovo Cimento C **36** Issue 1 Suppl. 1, (2013) 5–13.
5. R. Belvedere, Jorge A. Rueda, and R. Ruffini, *"Neutron star cores in the general relativistic Thomas-Fermi treatment"*. Int. J. Mod. Phys. Conf. Ser. **23**, (2013) 185–192.
6. R. Belvedere, K. Boshkayev, Jorge A. Rueda, and R. Ruffini, *"Uniformly rotating neutron stars in the global and local charge neutrality case"*. Nucl. Phys. A **921**, (2014) 33–59; arXiv:1307.2836

Papers Accepted and in Print

1. R. Belvedere, Jorge A. Rueda, and R. Ruffini, *"Neutron stars: mass-radius relation and global charge neutrality"*. Accepted for publication in *World Scientific Publishing in the Astrophysics series* edited by Profs. Fang Li-Zhi and Ruffini Remo.

2. R. Belvedere, D. Pugliese, Jorge A. Rueda, R. Ruffini and S.-S. Xue, *"Neutron star equilibrium configurations within a fully relativistic theory with strong, weak, electromagnetic and gravitational interactions"*. Accepted for publication in *International Journal of Modern Physics D (IJMPD)*.

Papers Submitted and in Preparation

1. R. Belvedere, Jorge A. Rueda, and R. Ruffini, *"On static and rotating globally and locally neutron stars"*. Submitted to *Journal of the Korean Physical Society*.

2. R. Belvedere, Jorge A. Rueda, R. Ruffini, *"On the Keplerian frequency and moment of inertia of neutron stars"*. Submitted to *A&A Letters*.

3. R. Belvedere, Jorge A. Rueda, R. Ruffini, *"On the magnetic field of pulsars with realistic neutron star configurations"*. Submitted to *ApJ Letters*.

Appendices

Appendix A

Neutron Stars, Einstein-Maxwell-Thomas-Fermi Equations and Relativistic Mean Field Theory

For a system composed by neutrons, protons and electrons, taking into account strong, weak, electromagnetic, and gravitational interactions in the context of a fully general relativistic theory, the total Lagrangian density is given by (see Belvedere et al. (2012) for details and Rueda et al. (2011) for the general case with finite temperature)

$$\mathcal{L} = \mathcal{L}_g + \mathcal{L}_f + \mathcal{L}_\sigma + \mathcal{L}_\omega + \mathcal{L}_\rho + \mathcal{L}_\gamma + \mathcal{L}_{\rm int}\,, \tag{A.1}$$

where the Lagrangian densities for the free-fields are

$$\mathcal{L}_g = -\frac{R}{16\pi G}\,, \tag{A.2}$$

$$\mathcal{L}_\gamma = -\frac{1}{16\pi}F_{\mu\nu}F^{\mu\nu}\,, \tag{A.3}$$

$$\mathcal{L}_\sigma = \frac{1}{2}\nabla_\mu\sigma\nabla^\mu\sigma - U(\sigma)\,, \tag{A.4}$$

$$\mathcal{L}_\omega = -\frac{1}{4}\Omega_{\mu\nu}\Omega^{\mu\nu} + \frac{1}{2}m_\omega^2\omega_\mu\omega^\mu\,, \tag{A.5}$$

$$\mathcal{L}_\rho = -\frac{1}{4}\mathcal{R}_{\mu\nu}\mathcal{R}^{\mu\nu} + \frac{1}{2}m_\rho^2\rho_\mu\rho^\mu\,, \tag{A.6}$$

where $\Omega_{\mu\nu} \equiv \partial_\mu\omega_\nu - \partial_\nu\omega_\mu$, $\mathcal{R}_{\mu\nu} \equiv \partial_\mu\rho_\nu - \partial_\nu\rho_\mu$, $F_{\mu\nu} \equiv \partial_\mu A_\nu - \partial_\nu A_\mu$ are the field strength tensors for the ω^μ, ρ and A^μ fields respectively, ∇_μ stands for

covariant derivative and R is the Ricci scalar. We adopt the Lorenz gauge for the fields A_μ, ω_μ, and ρ_μ.

The Lagrangian density for the three fermion species is

$$\mathcal{L}_f = \sum_{i=e,N} \bar{\psi}_i \left(i\gamma^\mu D_\mu - m_i \right) \psi_i \,, \tag{A.7}$$

where ψ_N is the nucleon isospin doublet, ψ_e is the electronic singlet, m_i states for the mass of each particle-specie and $D_\mu = \partial_\mu + \Gamma_\mu$, being Γ_μ the Dirac spin connections.

The interacting part of the Lagrangian density is, in the minimal coupling assumption, given by

$$\mathcal{L}_{\rm int} = -g_\sigma \sigma \bar{\psi}_N \psi_N - g_\omega \omega_\mu J^\mu_\omega - g_\rho \rho_\mu J^\mu_\rho + e A_\mu J^\mu_{\gamma,e} - e A_\mu J^\mu_{\gamma,N} \,, \tag{A.8}$$

where the conserved currents are

$$\begin{aligned}
J^\mu_\omega &= \bar{\psi}_N \gamma^\mu \psi_N \,, & \text{(A.9)} \\
J^\mu_\rho &= \bar{\psi}_N \tau_3 \gamma^\mu \psi_N \,, & \text{(A.10)} \\
J^\mu_{\gamma,e} &= \bar{\psi}_e \gamma^\mu \psi_e \,, & \text{(A.11)} \\
J^\mu_{\gamma,N} &= \bar{\psi}_N \left(\frac{1+\tau_3}{2} \right) \gamma^\mu \psi_N \,. & \text{(A.12)}
\end{aligned}$$

The coupling constants of the σ, ω and ρ-fields are g_σ, g_ω and g_ρ, and e is the fundamental electric charge. The Dirac matrices γ^μ and the isospin Pauli matrices satisfy the Dirac algebra in curved spacetime (see e.g. Ruffini and Bonazzola (1969); Lee and Pang (1987) for details)

$$\begin{aligned}
\{\gamma^\mu, \gamma^\nu\} &= 2g^{\mu\nu} \,, & \text{(A.13)} \\
\{\gamma_\mu, \gamma_\nu\} &= 2g_{\mu\nu} \,, & \text{(A.14)} \\
\{\gamma^\mu, \gamma_\nu\} &= 2\delta^\mu_\nu \,, & \text{(A.15)} \\
[\tau_i, \tau_j] &= 2\imath \epsilon_{ijk} \tau^k \,. & \text{(A.16)}
\end{aligned}$$

The equations of the motion of the above Lagrangians lead to the Einstein-Maxwell-Dirac system of equations

$$\begin{aligned}
G_{\mu\nu} + 8\pi G T_{\mu\nu} &= 0 \,, & \text{(A.17)} \\
\nabla_\mu F^{\mu\nu} - e J^\nu_{ch} &= 0 \,, & \text{(A.18)} \\
\nabla_\mu \Omega^{\mu\nu} + m^2_\omega \omega^\nu - g_\omega J^\nu_\omega &= 0 \,, & \text{(A.19)} \\
\nabla_\mu \mathcal{R}^{\mu\nu} + m^2_\rho \rho^\nu - g_\rho J^\nu_\rho &= 0 \,, & \text{(A.20)} \\
\nabla_\mu \nabla^\mu \sigma + \partial_\sigma U(\sigma) + g_s n_s &= 0 \,, & \text{(A.21)} \\
\left[\gamma_\mu \left(i D^\mu - V^\mu_N \right) - \tilde{m}_N \right] \psi_N &= 0 \,, & \text{(A.22)} \\
\left[\gamma_\mu \left(i D^\mu + e A^\mu \right) - m_e \right] \psi_e &= 0 \,, & \text{(A.23)}
\end{aligned}$$

where the nucleon effective mass is $\tilde{m}_N \equiv m_N + g_\sigma \sigma$, m_e is the electron mass, the scalar density n_s within the mean-field approximation, is given by the following expectation value

$$n_s = \langle \bar{\psi}_N \psi_N \rangle = \frac{2}{(2\pi)^3} \sum_{i=n,p} \int d^3k \frac{\tilde{m}_N}{\epsilon_i(p)} \,, \tag{A.24}$$

where $\epsilon_i(p) = \sqrt{p^2 + \tilde{m}_i^2}$ is the single particle energy, and

$$V_N^\mu \equiv g_\omega \omega^\mu + g_\rho \tau \rho^\mu + e \left(\frac{1+\tau_3}{2} \right) A^\mu \,, \tag{A.25}$$

is the effective four potential of nucleons.

The energy-momentum tensor of free-fields and free-fermions $T^{\mu\nu}$ of the system (A.3)–(A.6) is

$$T^{\mu\nu} = T_f^{\mu\nu} + T_\gamma^{\mu\nu} + T_\sigma^{\mu\nu} + T_\omega^{\mu\nu} + T_\rho^{\mu\nu} \,, \tag{A.26}$$

where

$$T_\gamma^{\mu\nu} = \frac{1}{4\pi} \left(F_\alpha^\mu F^{\alpha\nu} + \frac{1}{4} g^{\mu\nu} F_{\alpha\beta} F^{\alpha\beta} \right) \,, \tag{A.27}$$

$$T_\sigma^{\mu\nu} = \nabla^\mu \sigma \nabla^\nu \sigma - g^{\mu\nu} \left[\frac{1}{2} \nabla_\sigma \sigma \nabla^\sigma \sigma - U(\sigma) \right] \,, \tag{A.28}$$

$$\begin{aligned} T_\omega^{\mu\nu} &= \Omega_\alpha^\mu \Omega^{\alpha\nu} + \frac{1}{4} g^{\mu\nu} \Omega_{\alpha\beta} \Omega^{\alpha\beta} \\ &\quad + m_\omega^2 \left(\omega^\mu \omega^\nu - \frac{1}{2} g^{\mu\nu} \omega_\alpha \omega^\alpha \right) \,, \end{aligned} \tag{A.29}$$

$$\begin{aligned} T_\rho^{\mu\nu} &= \mathcal{R}_\alpha^\mu \mathcal{R}^{\alpha\nu} + \frac{1}{4} g^{\mu\nu} \mathcal{R}_{\alpha\beta} \mathcal{R}^{\alpha\beta} \\ &\quad + m_\rho^2 \left(\mathcal{R}^\mu \mathcal{R}^\nu - \frac{1}{2} g^{\mu\nu} \rho_\alpha \rho^\alpha \right) \,, \end{aligned} \tag{A.30}$$

$$T_f^{\mu\nu} = (\mathcal{E} + \mathcal{P}) u^\mu u^\nu - \mathcal{P} g^{\mu\nu} \,, \tag{A.31}$$

where the energy-density $\mathcal{E}$ and the pressure $\mathcal{P}$ are given by

$$\mathcal{E} = \sum_{i=n,p,e} \mathcal{E}_i, \qquad \mathcal{P} = \sum_{i=n,p,e} \mathcal{P}_i \,, \tag{A.32}$$

being $\mathcal{E}_i$ and $\mathcal{P}_i$ the single fermion fluid contributions (see Rueda et al. (2011) for details)

$$\mathcal{E}_i = \frac{2}{(2\pi)^3} \int_0^{P_i^F} \epsilon_i(p) \, 4\pi p^2 dp \,, \tag{A.33}$$

$$\mathcal{P}_i = \frac{1}{3} \frac{2}{(2\pi)^3} \int_0^{P_i^F} \frac{p^2}{\epsilon_i(p)} \, 4\pi p^2 dp \,. \tag{A.34}$$

It is worth to recall that the equation of state (A.32)–(A.34) satisfies the thermodynamic law

$$\mathcal{E} + \mathcal{P} = \sum_{i=n,p,e} n_i \mu_i \,, \tag{A.35}$$

where $\mu_i = \partial\mathcal{E}/\partial n_i = \sqrt{(P_i^F)^2 + \tilde{m}_i^2}$ and $n_i = (P_i^F)^3/(3\pi^2)$ are the free-chemical potential and number density of the i-specie with Fermi momentum P_i^F respectively.

In the static case, only the temporal components of the covariant currents survive, i.e. $\langle\bar{\psi}(x)\gamma^i\psi(x)\rangle = 0$. Thus, by taking the expectation values of Eqs. (A.9)–(A.12), it is possible to obtain the non-vanishing components of the currents

$$J_0^{ch} = n_{ch}u_0 = (n_p - n_e)u_0 \,, \tag{A.36}$$
$$J_0^{\omega} = n_b u_0 = (n_n + n_p)u_0 \,, \tag{A.37}$$
$$J_0^{\rho} = n_3 u_0 = (n_p - n_n)u_0 \,, \tag{A.38}$$

where $n_b = n_p + n_n$ is the baryon number density and $u_0 = \sqrt{g_{00}} = e^{\nu/2}$ is the covariant temporal component of the four-velocity of the fluid, which satisfies $u^\mu u_\mu = 1$.

Therefore, the Einstein-Maxwell equations (A.17)–(A.21), become

$$\mathrm{e}^{-\lambda(r)}\left(\frac{1}{r^2} - \frac{\lambda'}{r}\right) - \frac{1}{r^2} = -8\pi G T_0^0 \,, \tag{A.39}$$
$$\mathrm{e}^{-\lambda(r)}\left(\frac{1}{r^2} + \frac{1}{r}\frac{d\nu}{dr}\right) - \frac{1}{r^2} = -8\pi G T_1^1 \,, \tag{A.40}$$
$$\frac{d^2V}{dr^2} + \frac{dV}{dr}\left[\frac{2}{r} - \frac{1}{2}\left(\frac{d\nu}{dr} + \frac{d\lambda}{dr}\right)\right] = -\mathrm{e}^{\lambda} e J_0^{ch} \,, \tag{A.41}$$
$$\frac{d^2\sigma}{dr^2} + \frac{d\sigma}{dr}\left[\frac{2}{r} + \frac{1}{2}\left(\frac{d\nu}{dr} - \frac{d\lambda}{dr}\right)\right] = \mathrm{e}^{\lambda}\left[\partial_\sigma U(\sigma) + g_s n_s\right] \,, \tag{A.42}$$
$$\frac{d^2\omega}{dr^2} + \frac{d\omega}{dr}\left[\frac{2}{r} - \frac{1}{2}\left(\frac{d\nu}{dr} + \frac{d\lambda}{dr}\right)\right] = -\mathrm{e}^{\lambda}\left[g_\omega J_0^{\omega} - m_\omega^2\omega\right] \,, \tag{A.43}$$
$$\frac{d^2\rho}{dr^2} + \frac{d\rho}{dr}\left[\frac{2}{r} - \frac{1}{2}\left(\frac{d\nu}{dr} + \frac{d\lambda}{dr}\right)\right] = -\mathrm{e}^{\lambda}\left[g_\rho J_0^{\rho} - m_\rho^2\rho\right] \,, \tag{A.44}$$

where we have introduced the notation $\omega_0 = \omega$, $\rho_0 = \rho$, and $A_0 = V$.
The metric function λ is related to the mass $M(r)$ and the electric field $E(r) = -\mathrm{e}^{-(\nu+\lambda)/2}V'$ through

$$\mathrm{e}^{-\lambda(r)} = 1 - \frac{2GM(r)}{r} + Gr^2E^2(r) = 1 - \frac{2GM(r)}{r} + \frac{GQ^2(r)}{r^2} \,, \tag{A.45}$$

being $Q(r)$ the conserved charge, related to the electric field by $Q(r) = r^2 E(r)$.
The electron density n_e is, using the constancy of the generalized Fermi energy of the electons (see Eq. (2.9) in Subsec. 2.2.1), given by

$$n_e = \frac{\mathrm{e}^{-3\nu/2}}{3\pi^2}[\hat{V}^2 + 2m_e\hat{V} - m_e^2(\mathrm{e}^{\nu} - 1)]^{3/2}\,, \tag{A.46}$$

where $\hat{V} \equiv eV + E_e^F$. Substituting Eq.(A.46) into Eq. (A.41) one obtains the general relativistic extension of the relativistic Thomas-Fermi equation recently introduced for the study of compressed atoms by Rotondo et al. (2011b,a).

Appendix B

The Hartle Solution and Equatorial Circular Orbits

B.1 The Hartle-Thorne Vacuum Solution

It is possible to write the Hartle-Thorne metric given by eq. 3.4 in an analytic closed-form in the exterior vacuum case as function of the total mass M, angular momentum J, and quadrupole moment Q of the rotating star. The angular velocity of local inertial frames $\omega(r)$, proportional to Ω, and the functions h_0, h_2, m_0, m_2, k_2, proportional to Ω^2, are derived from the Einstein equations (see Hartle, 1967; Hartle and Thorne, 1968, for details). Following this prescriptions the eq. 3.4 become:

$$
\begin{aligned}
ds^2 = & \left(1-\frac{2M}{r}\right) \\
& \times \left[1+2k_1 P_2(\cos\theta)+2\left(1-\frac{2M}{r}\right)^{-1}\frac{J^2}{r^4}(2\cos^2\theta-1)\right]dt^2 \\
& + \frac{4J}{r}\sin^2\theta dt d\phi - \left(1-\frac{2M}{r}\right)^{-1} \\
& \times \left[1-2\left(k_1-\frac{6J^2}{r^4}\right)P_2(\cos\theta)-2\left(1-\frac{2M}{r}\right)^{-1}\frac{J^2}{r^4}\right]dr^2 \\
& - r^2[1-2k_2 P_2(\cos\theta)](d\theta^2+\sin^2\theta d\phi^2)\,, \qquad \text{(B.1)}
\end{aligned}
$$

where

$$k_1 = \frac{J^2}{Mr^3}\left(1+\frac{M}{r}\right)+\frac{5}{8}\frac{Q-J^2/M}{M^3}Q_2^2(x)\,, \tag{B.2}$$

$$k_2 = k_1+\frac{J^2}{r^4}+\frac{5}{4}\frac{Q-J^2/M}{M^2r\sqrt{1-2M/r}}Q_2^1(x)\,, \tag{B.3}$$

and

$$Q_2^1(x) = (x^2-1)^{1/2}\left[\frac{3x}{2}\ln\left(\frac{x+1}{x-1}\right)-\frac{3x^2-2}{x^2-1}\right]\,, \tag{B.4}$$

$$Q_2^2(x) = (x^2-1)\left[\frac{3}{2}\ln\left(\frac{x+1}{x-1}\right)-\frac{3x^3-5x}{(x^2-1)^2}\right]\,, \tag{B.5}$$

are the associated Legendre functions of the second kind, being $P_2(\cos\theta) = (1/2)(3\cos^2\theta-1)$ the Legendre polynomial, and where it has been effectuated the re-scaling $x = r/M-1$. The constants M, J and Q are the total mass, angular momentum and mass quadrupole moment of the rotating object, respectively. This form of the metric corrects some misprints of the original paper by Hartle and Thorne (1968) (see also Berti et al., 2005; Boshkayev et al., 2012a). To obtain the exact numerical values of M, J and Q, the exterior and interior metrics have to be matched at the surface of the star. It is worthy underline that in the terms involving J^2 and Q, the total mass M can be substituted by M_0 since δM is already a second order term in the angular velocity.

B.2 Angular Velocity of Equatorial Circular Orbits

It is possible to obtain the analytical expression for the angular velocity Ω given by Eq. (3.18) with respect to an observer at infinity, taking into account the parameterization of the four-velocity u of a test particle on a circular orbit in equatorial plane of axisymmetric stationary spacetime, regarding as parameter the angular velocity Ωitself:

$$u = \Gamma[\partial_t+\Omega\partial_\phi]\,, \tag{B.6}$$

where Γ is a normalization factor such that $u^\alpha u_\alpha = 1$. Normalizing and applying the geodesics conditions we get the following expressions for Γ and $\Omega = u^\phi/u^t$

$$\Gamma = \pm(g_{tt}+2\Omega g_{t\phi}+\Omega^2 g_{\phi\phi})^{-1/2}\,, \tag{B.7}$$

$$g_{tt,r}+2\Omega g_{t\phi,r}+\Omega^2 g_{\phi\phi,r} = 0\,. \tag{B.8}$$

Thus, the solution of Eqs. (B.7–B.8) can be written as

$$\Omega^{\pm}_{\rm orb}(r) = \frac{u^\phi}{u^t} = \frac{-g_{t\phi,r} \pm \sqrt{(g_{t\phi,r})^2 - g_{tt,r} g_{\phi\phi,r}}}{g_{\phi\phi,r}}\,, \tag{B.9}$$

where $+/-$ stands for co-rotating/counter-rotating orbits, u^ϕ and u^t are the angular and time components of the four-velocity respectively, and a colon stands for partial derivative with respect to the corresponding coordinate. To determine the mass shedding angular velocity (the Keplerian angular velocity) of the neutron stars, we need to consider only the co-rotating orbit, so from here and thereafter we take into account only the plus sign in Eq. (B.7) and we write $\Omega^{+}_{\rm orb}(r) = \Omega_{\rm orb}(r)$.

For the Hartle external solution given by Eq. (B.1) we obtain Eq. (3.18) with

$$F_1 = \left(\frac{M}{r}\right)^{3/2}\,, \tag{B.10}$$

$$F_2 = \frac{48M^7 - 80M^6 r + 4M^5 r^2 - 18M^4 r^3}{16M^2 r^4 (r-2M)} \tag{B.11}$$

$$+ \frac{40M^3 r^4 + 10M^2 r^5 + 15M r^6 - 15 r^7}{16M^2 r^4 (r-2M)} + F\,, \tag{B.12}$$

$$F_3 = \frac{6M^4 - 8M^3 r - 2M^2 r^2 - 3M r^3 + 3r^4}{16M^2 r (r-2M)/5} - F\,, \tag{B.13}$$

$$F = \frac{15(r^3 - 2M^3)}{32M^3} \ln \frac{r}{r-2M}\,. \tag{B.14}$$

$$\tag{B.15}$$

The maximum angular velocity possible for a rotating star at the mass-shedding limit is the Keplerian angular velocity evaluated at the equator ($r = R_{\rm eq}$), i.e.

$$\Omega_K^{J\neq 0} = \Omega_{\rm orb}(r = R_{\rm eq})\,. \tag{B.16}$$

In the static case i.e. when $j = 0$ hence $q = 0$ and $\delta M = 0$ we have the well-known Schwarzschild solution and the orbital angular velocity for a test particle $\Omega_K^{J=0}$ on the surface ($r = R$) of the neutron star is given by

$$\Omega_K^{J=0} = \sqrt{\frac{M^{J=0}}{R^3_{M^{J=0}}}}\,. \tag{B.17}$$

List of Figures

List of Tables

Bibliography

Antoniadis, J., Freire, P. C. C., Wex, N., Tauris, T. M., Lynch, R. S., van Kerkwijk, M. H., Kramer, M., Bassa, C., Dhillon, V. S., Driebe, T., Hessels, J. W. T., Kaspi, V. M., Kondratiev, V. I., Langer, N., Marsh, T. R., McLaughlin, M. A., Pennucci, T. T., Ransom, S. M., Stairs, I. H., van Leeuwen, J., Verbiest, J. P. W., and Whelan, D. G. (2013). A Massive Pulsar in a Compact Relativistic Binary. *Science*, 340:448.

Arnett, D., Farhi, E., and Olinto, A. (1996). Book Review: Supernovae and nucleosynthesis: an investigation of the history of matter, from the big bang to the present / Princeton University Press, 1996. *Space Science Reviews*, 78:559.

Baade, W. and Zwicky, F. (1934). Cosmic Rays from Super-novae. *Proceedings of the National Academy of Science*, 20:259–263.

Baumgarte, T. W., Shapiro, S. L., and Shibata, M. (2000). On the Maximum Mass of Differentially Rotating Neutron Stars. *ApJL*, 528:L29–L32.

Baym, G., Pethick, C., and Sutherland, P. (1971). The Ground State of Matter at High Densities: Equation of State and Stellar Models. *ApJ*, 170:299–+.

Belvedere, R., Boshkayev, K., Rueda, J. A., and Ruffini, R. (2014). Uniformly rotating neutron stars in the global and local charge neutrality cases. *Nucl. Phys. A*, 921:33;arXiv:1307.2836.

Belvedere, R., Pugliese, D., Rueda, J. A., Ruffini, R., and Xue, S.-S. (2012). Neutron star equilibrium configurations within a fully relativistic theory with strong, weak, electromagnetic, and gravitational interactions. *Nuclear Physics A*, 883:1–24.

Benhar, O., Ferrari, V., Gualtieri, L., and Marassi, S. (2005). Perturbative approach to the structure of rapidly rotating neutron stars. *Phys. Rev. D*, 72(4):044028–+.

Berti, E., White, F., Maniopoulou, A., and Bruni, M. (2005). Rotating neutron stars: an invariant comparison of approximate and numerical spacetime models. *MNRAS*, 358:923–938.

Bethe, H. A. and Critchfield, C. L. (1938). The Formation of Deuterons by Proton Combination. *Physical Review*, 54:248–254.

Bhattacharyya, S., Strohmayer, T. E., Miller, M. C., and Markwardt, C. B. (2005). Constraints on Neutron Star Parameters from Burst Oscillation Light Curves of the Accreting Millisecond Pulsar XTE J1814-338. *ApJ*, 619:483–491.

Bini, D., Boshkayev, K., Ruffini, R., and Siutsou, I. (2013). Equatorial circular geodesics in the Hartle-Thorne spacetime. *Il Nuovo Cimento C*, 36:31.

Boguta, J. (1981). Remarks on the beta stability in neutron stars. *Physics Letters B*, 106:255–258.

Boguta, J. (1989). Chiral nuclear interactions. *Nuclear Physics A*, 501:637–652.

Boguta, J. and Bodmer, A. R. (1977). Relativistic calculation of nuclear matter and the nuclear surface. *Nuclear Physics A*, 292:413–428.

Boguta, J. and Moszkowski, S. A. (1983). Nonlinear mean field theory for nuclear matter and surface properties. *Nuclear Physics A*, 403:445–468.

Boguta, J. and Rafelski, J. (1977). Thomas Fermi model of finite nuclei. *Physics Letters B*, 71:22–26.

Boguta, J. and Stocker, H. (1983). Systematics of nuclear matter properties in a non-linear relativistic field theory. *Physics Letters B*, 120:289–293.

Boshkayev, K., Quevedo, H., and Ruffini, R. (2012a). Gravitational field of compact objects in general relativity. *Phys. Rev. D*, 86(6):064043.

Boshkayev, K., Rotondo, M., and Ruffini, R. (2012b). On Magnetic Fields in Rotating Nuclear Matter Cores of Stellar Dimensions. *International Journal of Modern Physics Conference Series*, 12:58–67.

Bowers, R. L., Campbell, J. A., and Zimmerman, R. L. (1973a). Model Equation of State for Strongly Interacting Superdense Matter. *Phys. Rev. D*, 7:2289–2299.

Bowers, R. L., Campbell, J. A., and Zimmerman, R. L. (1973b). Relativistic Many-Body Theory for Strongly Interacting Matter. *Phys. Rev. D*, 7:2278–2288.

Cameron, A. G. W. (1959). Pycnonuclear Reations and Nova Explosions. *ApJ*, 130:916.

Chadwick, J. (1932). Possible Existence of a Neutron. *Nature*, 129:312.

Chandrasekhar, S. (1931). The Maximum Mass of Ideal White Dwarfs. *ApJ*, 74:81.

Comella, J. M., Craft, H. D., Lovelace, R. V. E., and Sutton, J. M. (1969). Crab Nebula Pulsar NP 0532. *Nature*, 221:453–454.

Debye, P. and Hückel, E. (1923). Zur theorie der elektrolyte. i. gefrierpunktserniedrigung und verwandte erscheinungen. *Physikalische Zeitschrift*, 24(185):305.

Demorest, P. B., Pennucci, T., Ransom, S. M., Roberts, M. S. E., and Hessels, J. W. T. (2010). A two-solar-mass neutron star measured using Shapiro delay. *Nature*, 467:1081–1083.

Dewitt, C. and Dewitt, B. S., editors (1973). *Black holes (Les astres occlus)*.

Dhiman, S. K., Kumar, R., and Agrawal, B. K. (2007). Nonrotating and rotating neutron stars in the extended field theoretical model. *Phys. Rev. C*, 76(4):045801.

Duerr, H. (1956). Relativistic Effects in Nuclear Forces. *Physical Review*, 103:469–480.

Evans, R. (1992). *Fundamentals of inhomogeneous fluids*. Decker, "New York".

Ferrari, A. and Ruffini, R. (1969). Theoretical Implications of the Second Time Derivative of the Period of the Pulsar NP 0532. *ApJL*, 158:L71.

Ferreirinho, J., Ruffini, R., and Stella, L. (1980). On the relativistic Thomas-Fermi model. *Physics Letters B*, 91:314–316.

Feynman, R. P., Metropolis, N., and Teller, E. (1949). Equations of State of Elements Based on the Generalized Fermi-Thomas Theory. *Physical Review*, 75:1561–1573.

Friedman, J. L., Ipser, J. R., and Sorkin, R. D. (1988). Turning-point method for axisymmetric stability of rotating relativistic stars. *ApJ*, 325:722–724.

Friedman, J. L., Parker, L., and Ipser, J. R. (1986). Rapidly rotating neutron star models. *ApJ*, 304:115–139.

Gamow, G. (1937). *Structure of atomic nuclei and nuclear transformations*. The international series of monographs on physics. pub-CLARENDON, pub-CLARENDON:adr, Second edition.

Gamow, G. and Schoenberg, M. (1941). Neutrino Theory of Stellar Collapse. *Physical Review*, 59:539–547.

Giacconi, R., Gursky, H., Paolini, F. R., and Rossi, B. B. (1962). Evidence for x Rays From Sources Outside the Solar System. *Physical Review Letters*, 9:439–443.

Gold, T. (1968). Rotating Neutron Stars as the Origin of the Pulsating Radio Sources. *Nature*, 218:731–732.

Gombás, P. (1950). Die statistische Theorie des Atoms und ihre Anwendungen (H. Hönl). *Zeitschrift Naturforschung Teil A*, 5:235.

Goriely, S., Chamel, N., Janka, H.-T., and Pearson, J. M. (2011). The decompression of the outer neutron star crust and r-process nucleosynthesis. *A&A*, 531:A78.

Gupta, N. and Arumugam, P. (2013). "Pasta phases" in neutron stars studied with extended relativistic mean field models. *Phys. Rev. C*, 87(2):028801.

Haensel, P., Potekhin, A. Y., and Yakovlev, D. G., editors (2007). *Neutron Stars 1 : Equation of State and Structure*, volume 326 of *Astrophysics and Space Science Library*.

Harrison, B. K., Wakano, M., and Wheeler, J. A. (1958). *Matter-energy at high density: end point of thermonuclear evolution*. "La structure et la évolutione de l'universe". Stoops R., "Brussels".

Hartle, J. B. (1967). Slowly Rotating Relativistic Stars. I. Equations of Structure. *ApJ*, 150:1005.

Hartle, J. B. (1973). Slowly Rotating Relativistic Stars. IX: Moments of Inertia of Rotationally Distorted Stars. *Ap&SS*, 24:385–405.

Hartle, J. B. and Sharp, D. H. (1967). Variational Principle for the Equilibrium of a Relativistic, Rotating Star. *ApJ*, 147:317–+.

Hartle, J. B. and Thorne, K. S. (1968). Slowly Rotating Relativistic Stars. II. Models for Neutron Stars and Supermassive Stars. *ApJ*, 153:807.

Hebeler, K., Lattimer, J. M., Pethick, C. J., and Schwenk, A. (2010). Constraints on Neutron Star Radii Based on Chiral Effective Field Theory Interactions. *Physical Review Letters*, 105(16):161102.

Heinke, C. O., Rybicki, G. B., Narayan, R., and Grindlay, J. E. (2006). A Hydrogen Atmosphere Spectral Model Applied to the Neutron Star X7 in the Globular Cluster 47 Tucanae. *ApJ*, 644:1090–1103.

Hessels, J. W. T., Ransom, S. M., Stairs, I. H., Freire, P. C. C., Kaspi, V. M., and Camilo, F. (2006). A Radio Pulsar Spinning at 716 Hz. *Science*, 311:1901–1904.

Hewish, A., Bell, S. J., Pilkington, J. D. H., Scott, P. F., and Collins, R. A. (1968). Observation of a Rapidly Pulsating Radio Source. *Nature*, 217:709–713.

Hewish, A. and Okoye, S. E. (1965). Evidence for an Unusual Source of High Radio Brightness Temperature in the Crab Nebula. *Nature*, 207:59–60.

Hirata, D., Toki, H., and Tanihata, I. (1995). Relativistic mean-field theory on the xenon, cesium and barium isotopes. *Nuclear Physics A*, 589:239–248.

Johnson, M. H. and Teller, E. (1955). Classical Field Theory of Nuclear Forces. *Physical Review*, 98:783–787.

Klein, O. (1949). On the Thermodynamical Equilibrium of Fluids in Gravitational Fields. *Reviews of Modern Physics*, 21:531–533.

Kodama, T. and Yamada, M. (1972). Theory of Superdense Stars. *Progress of Theoretical Physics*, 47:444–459.

Kubis, S. (2007). Nuclear symmetry energy and stability of matter in neutron stars. *Phys. Rev. C*, 76(2):025801.

Kubis, S. and Kutschera, M. (1997a). Nuclear matter in relativistic mean field theory with isovector scalar meson. *Physics Letters B*, 399:191–195.

Kubis, S. and Kutschera, M. (1997b). Nuclear matter in relativistic mean field theory with isovector scalar meson. *Physics Letters B*, 399:191–195.

Lalazissis, G. A., König, J., and Ring, P. (1997). New parametrization for the Lagrangian density of relativistic mean field theory. *Phys. Rev. C*, 55:540–543.

Landau, L. (1938). Origin of Stellar Energy. *Nature*, 141:333–334.

Landau, L. D. (1932). On the theory of stars. *Phys. Z. Sowjetunion*, 1:285–288.

Lattimer, J. M. (2012). The Nuclear Equation of State and Neutron Star Masses. *Annual Review of Nuclear and Particle Science*, 62:485–515.

Lattimer, J. M. and Prakash, M. (2004). The Physics of Neutron Stars. *Science*, 304:536–542.

Lattimer, J. M. and Schutz, B. F. (2005). Constraining the Equation of State with Moment of Inertia Measurements. *ApJ*, 629:979–984.

Lee, T. D. and Margulies, M. (1975). Interaction of a dense fermion medium with a scalar-meson field. *Phys. Rev. D*, 11:1591–1610.

Lee, T. D. and Pang, Y. (1987). Fermion soliton stars and black holes. *Phys. Rev. D*, 35:3678–3694.

Lee, T. D. and Wick, G. C. (1974). Vacuum stability and vacuum excitation in a spin-0 field theory. *Phys. Rev. D*, 9:2291–2316.

Lieb, E. H. (1981). Thomas-fermi and related theories of atoms and molecules. *Rev. Mod. Phys.*, 53:603–641.

Loan, D. T., Tan, N. H., Khoa, D. T., and Margueron, J. (2011). Equation of state of neutron star matter, and the nuclear symmetry energy. *Phys. Rev. C*, 83(6):065809.

Lyne, A. G. and Graham-Smith, F. (1998). *Pulsar astronomy*. Cambridge University Press.

McLaughlin, M. A., Rea, N., Gaensler, B. M., Chatterjee, S., Camilo, F., Kramer, M., Lorimer, D. R., Lyne, A. G., Israel, G. L., and Possenti, A. (2007). Discovery of Pulsations and a Possible Spectral Feature in the X-Ray Emission from Rotating Radio Transient J1819-1458. *ApJ*, 670:1307–1313.

Migdal, A. B., Popov, V. S., and Voskresenskiĭ, D. N. (1977). The vacuum charge distribution near super-charged nuclei. *Soviet Journal of Experimental and Theoretical Physics*, 45:436.

Migdal, A. B., Voskresenskiĭ, D. N., and Popov, V. S. (1976). Distribution of vacuum charge near supercharged nuclei. *ZhETF Pisma Redaktsiiu*, 24:186.

Miller, L. D. and Green, A. E. (1972). Relativistic Self-Consistent Meson Field Theory of Spherical Nuclei. *Phys. Rev. C*, 5:241–252.

Morrison, I. A., Baumgarte, T. W., and Shapiro, S. L. (2004). Effect of Differential Rotation on the Maximum Mass of Neutron Stars: Realistic Nuclear Equations of State. *ApJ*, 610:941–947.

Mott, N. F. (1936). The Electrical Resistance of Dilute Solid Solutions. *Proceedings of the Cambridge Philosophical Society*, 32:281.

Müller, B. and Rafelski, J. (1975). Stabilization of the Charged Vacuum Created by Very Strong Electrical Fields in Nuclear Matter. *Physical Review Letters*, 34:349–352.

Müther, H., Prakash, M., and Ainsworth, T. L. (1987). The nuclear symmetry energy in relativistic Brueckner-Hartree-Fock calculations. *Physics Letters B*, 199:469–474.

Myers, W. (1966). Nuclear masses and deformations. *Nucl. Phys.*, 81:1–60.

Ng, C.-Y. and Kaspi, V. M. (2011). High Magnetic Field Rotation-powered Pulsars. In Göğüş, E., Belloni, T., and Ertan, Ü., editors, *American Institute of Physics Conference Series*, volume 1379 of *American Institute of Physics Conference Series*, pages 60–69.

Olson, E. and Bailyn, M. (1975). Internal structure of multicomponent static spherical gravitating fluids. *Phys. Rev. D*, 12:3030–3036.

Oppenheimer, J. R. and Volkoff, G. M. (1939). On Massive Neutron Cores. *Phys. Rev.*, 55:374–381.

Pacini, F. (1967). Energy Emission from a Neutron Star. *Nature*, 216:567–568.

Pearson, J. M., Goriely, S., and Chamel, N. (2011). Properties of the outer crust of neutron stars from Hartree-Fock-Bogoliubov mass models. *Phys. Rev. C*, 83(6):065810.

Popov, V. (2010). From super-charged nuclei to massive nuclear density cores. *AIP Conference Proceedings*, 1205(1):127–131.

Ravenhall, D. G. and Pethick, C. J. (1994). Neutron star moments of inertia. *ApJ*, 424:846–851.

Rhoades, C. E. and Ruffini, R. (1974). Maximum Mass of a Neutron Star. *Physical Review Letters*, 32:324–327.

Rosseland, S. (1924). Electrical state of a star. *MNRAS*, 84:720–728.

Rotondo, M., Rueda, J. A., Ruffini, R., and Xue, S.-S. (2011a). Relativistic Feynman-Metropolis-Teller theory for white dwarfs in general relativity. *Phys. Rev. D*, 84(8):084007.

Rotondo, M., Rueda, J. A., Ruffini, R., and Xue, S.-S. (2011b). Relativistic Thomas-Fermi treatment of compressed atoms and compressed nuclear matter cores of stellar dimensions. *Phys. Rev. C*, 83(4):045805.

Rotondo, M., Rueda, J. A., Ruffini, R., and Xue, S.-S. (2011c). The self-consistent general relativistic solution for a system of degenerate neutrons, protons and electrons in β-equilibrium. *Physics Letters B*, 701:667–671.

Rotondo, M., Ruffini, R., and Xue, S.-S. (2008). Neutral Nuclear Core VS Super Charged One. In Kleinert, H., Jantzen, R. T., and Ruffini, R., editors, *The Eleventh Marcel Grossmann Meeting On Recent Developments in Theoretical and Experimental General Relativity, Gravitation and Relativistic Field Theories*, pages 1352–1355.

Rotondo, M., Ruffini, R., Xue, S.-S., and Popov, V. (2011d). On Gravitationally and Electrodynamically Bound Nuclear Matter Cores of Stellar Dimensions. *International Journal of Modern Physics D*, 20:1995–2002.

Rueda, J. A., Ruffini, R., and Xue, S.-S. (2011). The Klein first integrals in an equilibrium system with electromagnetic, weak, strong and gravitational interactions. *Nuclear Physics A*, 872:286–295.

Ruffini, R. (2008). The Role of Thomas-Fermi Approach in Neutron Star Matter. In *Path Integrals - New Trends and Perspectives*, pages 207–218.

Ruffini, R. and Bonazzola, S. (1969). Systems of Self-Gravitating Particles in General Relativity and the Concept of an Equation of State. *Physical Review*, 187:1767–1783.

Ruffini, R., Rotondo, M., and Xue, S.-S. (2007). Electrodynamics for Nuclear Matter in Bulk. *International Journal of Modern Physics D*, 16:1–9.

Ruffini, R. and Stella, L. (1981). Some comments on the relativistic Thomas-Fermi model and the Vallarta-Rosen equation. *Physics Letters B*, 102:442–444.

Ruffini, R., Vereshchagin, G., and Xue, S.-S. (2010). Electron-positron pairs in physics and astrophysics: From heavy nuclei to black holes. *Phys. Rep.*, 487:1–140.

Ruffini, R., Vitagliano, L., and Xue, S.-S. (2003a). On a separatrix in the gravitational collapse to an overcritical electromagnetic black hole. *Physics Letters B*, 573:33–38.

Ruffini, R., Vitagliano, L., and Xue, S.-S. (2003b). On plasma oscillations in strong electric fields. *Physics Letters B*, 559:12–19.

Ruffini, R. and Xue, S.-S. (2008). Dyadosphere formed in gravitational collapse. In Lee, D.-S. and Lee, W., editors, *American Institute of Physics Conference Series*, volume 1059 of *American Institute of Physics Conference Series*, pages 72–100.

Schramm, S., Dexheimer, V., Negreiros, R., Schürhoff, T., and Steinheimer, J. (2013). *Structure and Cooling of Neutron and Hybrid Stars*. Greiner, W.

Shapiro, S. L. (2000). Differential Rotation in Neutron Stars: Magnetic Braking and Viscous Damping. *ApJ*, 544:397–408.

Shapiro, S. L. and Teukolsky, S. A. (1983). *Black holes, white dwarfs, and neutron stars: The physics of compact objects*. Research supported by the National Science Foundation. New York, Wiley-Interscience, 1983, 663 p.

Sharma, B. K. and Pal, S. (2009). Nuclear symmetry energy effects in finite nuclei and neutron star. *Physics Letters B*, 682:23–26.

Sharma, M. M., Nagarajan, M. A., and Ring, P. (1993). Rho meson coupling in the relativistic mean field theory and description of exotic nuclei. *Physics Letters B*, 312:377–381.

Sorkin, R. (1981). A Criterion for the Onset of Instability at a Turning Point. *ApJ*, 249:254.

Sorkin, R. D. (1982). A Stability Criterion for Many Parameter Equilibrium Families. *ApJ*, 257:847.

Stergioulas, N. (2003). Rotating Stars in Relativity. *Living Reviews in Relativity*, 6:3.

Sugahara, Y. and Toki, H. (1994). Relativistic mean-field theory for unstable nuclei with non-linear σ and ω terms. *Nuclear Physics A*, 579:557–572.

Takami, K., Rezzolla, L., and Yoshida, S. (2011). A quasi-radial stability criterion for rotating relativistic stars. *MNRAS*, 416:L1–L5.

Tamii, A., Poltoratska, I., von Neumann-Cosel, P., Fujita, Y., Adachi, T., Bertulani, C. A., Carter, J., Dozono, M., Fujita, H., Fujita, K., Hatanaka, K., Ishikawa, D., Itoh, M., Kawabata, T., Kalmykov, Y., Krumbholz, A. M., Litvinova, E., Matsubara, H., Nakanishi, K., Neveling, R., Okamura, H., Ong, H. J., Özel-Tashenov, B., Ponomarev, V. Y., Richter, A., Rubio, B., Sakaguchi, H., Sakemi, Y., Sasamoto, Y., Shimbara, Y., Shimizu, Y., Smit, F. D., Suzuki, T., Tameshige, Y., Wambach, J., Yamada, R., Yosoi, M., and Zenihiro, J. (2011). Complete Electric Dipole Response and the Neutron Skin in Pb208. *Physical Review Letters*, 107(6):062502.

Tolman, R. C. (1930). On the Weight of Heat and Thermal Equilibrium in General Relativity. *Physical Review*, 35:904–924.

Tolman, R. C. (1939). Static Solutions of Einstein's Field Equations for Spheres of Fluid. *Physical Review*, 55:364–373.

Torok, G., Bakala, P., Stuchlik, Z., and Cech, P. (2008). Modeling the Twin Peak QPO Distribution in the Atoll Source 4U 1636-53. *Acta Astronomica*, 58:1–14.

Trümper, J. E. (2011a). Observations of neutron stars and the equation of state of matter at high densities. *Progress in Particle and Nuclear Physics*, 66:674–680.

Trümper, J. E. (2011b). Observations of neutron stars and the equation of state of matter at high densities. *Progress in Particle and Nuclear Physics*, 66:674–680.

Trümper, J. E., Burwitz, V., Haberl, F., and Zavlin, V. E. (2004). The puzzles of RX J1856.5-3754: neutron star or quark star? *Nuclear Physics B Proceedings Supplements*, 132:560–565.

Walecka, J. D. (1974). A theory of highly condensed matter. *Annals of Physics*, 83:491–529.

Weber, F. and Glendenning, N. K. (1992). Application of the improved Hartle method for the construction of general relativistic rotating neutron star models. *ApJ*, 390:541–549.

Zeldovich, Y. B. and Novikov, I. D. (1971). *Relativistic astrophysics. Vol.1: Stars and relativity*. Chicago: University of Chicago Press, 1971.

Zheng, X., Pan, N., and Zhang, L. (2007). 1122 Hz rotation of XTE J1739-285 as a probe of quark matter in the interior of the neutron star. *ArXiv e-prints*.

Zhu, W. W., Kaspi, V. M., McLaughlin, M. A., Pavlov, G. G., Ng, C.-Y., Manchester, R. N., Gaensler, B. M., and Woods, P. M. (2011). Chandra Observations of the High-magnetic-field Radio Pulsar J1718-3718. *ApJ*, 734:44.